9-27-2023

1D/3D Electrochemical Thermal model of a Battery System at Cell and Modular Levels

Kieran James Johnson-Bujold
University of Windsor

1D/3D Electrochemical Thermal model of a Battery System at Cell and Modular Levels

By

Kieran Johnson-Bujold

A Thesis
Submitted to the Faculty of Graduate Studies
through the Department of Mechanical, Automotive and Materials Engineering
in Partial Fulfillment of the Requirements for
the Degree of Master of Applied Science
at the University of Windsor

Windsor, Ontario, Canada

2023

1D/3D Electrochemical Thermal model of a Battery System at Cell and Modular Levels

by

Kieran Johnson-Bujold

APPROVED BY:

N. Van Engelen
Department of Civil and Environmental Engineering

N. Eaves
Department of Mechanical, Automotive, and Materials Engineering

---

O. Jianu, Advisor
Department of Mechanical, Automotive, and Materials Engineering

August 24th, 2023

DECLARATION OF ORIGINALITY

I hereby certify that I am the sole author of this thesis and that no part of this thesis has been published or submitted for publication.

I certify that, to the best of my knowledge, my thesis does not infringe upon anyone's copyright nor violate any proprietary rights and that any ideas, techniques, quotations, or any other material from the work of other people included in my thesis, published or otherwise, are fully acknowledged in accordance with the standard referencing practices. Furthermore, to the extent that I have included copyrighted material that surpasses the bounds of fair dealing within the meaning of the Canada Copyright Act, I certify that I have obtained a written permission from the copyright owner(s) to include such material(s) in my thesis and have included copies of such copyright clearances to my appendix.

I declare that this is a true copy of my thesis, including any final revisions, as approved by my thesis committee and the Graduate Studies office, and that this thesis has not been submitted for a higher degree to any other University or Institution.

ABSTRACT

One of the many current significant challenges of lithium-ion battery use is keeping the thermal limits of the boundaries within a reasonable range. This applies equally to hybrid electric vehicles and to full-battery electric vehicles. To accomplish this, an accurate understanding of the thermal behavior of the battery is necessary, and consequently, accurate thermal models are required. To achieve this accuracy, the model's parameters must be well-predicted to reduce the behavior difference between simulated and experimental temperatures. These models should also describe the voltage behavior of the battery adequately to encapsulate the system's design requirements fully.

To estimate the parameters of the model, a hybrid pulse power characteristic profile was performed at multiple temperatures and multiple discharge rates, and the battery's voltage and temperature response were measured at ambient conditions. A one-dimensional electrochemical model was developed, and a genetic algorithm minimizing the root mean squared error between modeled and experimental voltages was completed. Current loads representing the loading conditions of the standard world harmonized light-duty cycle (WLTC), environmental protection agency driving cycle (EPA), China light-duty cycle (CLTC), and Nuremberg ring cycle (NR) were applied to the battery cell model. The battery cell model's simulated voltages were compared to the experimental voltages of the above driving cycles. These initial simulations show that parameter estimation can accurately simulate the voltage behavior of the battery. A heat generation model was developed, including reversible and irreversible heat generation terms. The thermal behavior of the battery, such as the maximum, minimum, and mean temperatures, was investigated for the aforementioned drive cycles at ambient conditions, at both the modular and cellular levels.

ACKNOWLEDGEMENTS

Here, sitting and pondering about the people involved throughout this master's experience, I am reminded of a common phrase "It takes a village." Often a short form of the entire proverb describing the intensity of resources and people required to raise a prospective individual in today's world. I identify parallels between the number of people in a village and the number of people who have guided me throughout this learning journey.

To describe everyone who helped and aided me in full detail and with accurate gratitude would require a whole extra document of thesis length. As such, before my acknowledgments, I must oddly start with an apology, as I can only provide a fraction of the gratitude that is undoubtedly deserved by all of the individuals who fall into this brief acknowledgment.

Firstly, I must start with my advisor, Dr.Ofelia Jianu, head of the I-FuELs team, Associate Professor at the University of Windsor, and Dual International Masters Degree (DIMD) program coordinator, whose devotion to teaching, great insight, patience, and guidance throughout the entire thesis were indeed the reasons I could attain any success within the program. To Dr. Satyam Panchal, the Adjunct Professor at the University of Waterloo, and Sr. Adv. Battery Systems engineer at Stellantis, whose expertise, kindness, and questions were always constructive. Emiliano di Tullio, Virtual Analysis Engineer at Stellantis, whose knowledge, sincerity, and discussions provided a route to successful outcomes. Dr. Angelo Bonfitto, whose constructive feedback was always a welcome addition to the thesis process.

To the DIMD coordinators Dr.Jennifer Johrendt, Professoressa Maria Cavatorta, and Marie Mills, whose devotion to the student's well-being and learning could not be described in a mere paragraph. Their work on making this incredible program successful is genuinely appreciated.

To my committee advisors Dr. Nickolas Eaves, and Dr. Niel Van Engelen, my appreciation for their valuable time reading and questioning my thesis cannot be overstated.

To the many others, Anosh Mevawalla, Dr.Soumya Gudiyella, and Rafael Braga, whose kindness and support were always highly appreciated and made me feel welcome to work with the team.

For more personal acknowledgments, I would like to thank my family. My brother Liam, whose fortitude, and unwavering gentleness, even in the face of difficulties, always reminds me of what type of person we should strive to become. My brother Aidan, whose passion and mental strength to pursue what he truly loves, always inspires me to strive to follow my dreams. My brother Declan's humor and wit always remind me to find joy in life. To Lindsay, mein grossliebe, for all the love and support during this enduring time. Last but certainly not least, my parents, both retired teachers, whose years of tireless affection and ardent dedication to ensuring they pass their love of education and learning on to me, have certainly been the biggest inspiration for learning any person could ever dream of.

TABLE OF CONTENTS

LIST OF TABLES

LIST OF FIGURES

NOMENCLATURE

List of Symbols

$\frac{dOCV}{dT}$ Open circuit potential gradient with respect to temperature ($\frac{V}{K}$)

$\psi(x)$ Unknown potential electrolyte function for Sturm louieville problem

τ Tortuosity of electrode

A Area (m^2) or state matrix

a_s Ratio of electrode interface area to volume ($\frac{1}{m}$)

B Input matrix

C Output matrix or capacity (Ah)

c Total charge in battery (Ah)

C_1 Polarization capacitance (F)

c_e Concentration in electrolyte ($\frac{m^2}{s}$)

$c_{s,0}$ Initial concentration of lithium in solid ($\frac{mol}{m^3}$)

$c_{s,max,anode}$ Maximum solid concentration in anodic material ($\frac{mol}{m^3}$)

$c_{s,max,cathode}$ Maximum solid concentration in cathodic material ($\frac{mol}{m^3}$)

$c_{s,max}$ Maximum lithium concentration in solid material ($\frac{mol}{m^3}$)

$c_{s,min,anode}$ Minimum solid concentration in anodic material ($\frac{mol}{m^3}$)

c_{s-e} Lithium concentration at the solid-electrolyte interface ($\frac{mol}{m^3}$)

c_s Solid concentration ($\frac{mol}{m^3}$)

Cr Controllability matrix

D Diffusion coefficient ($\frac{m^2}{s}$) or zero matrix

D_{eff} Effective diffusion coefficient electrolyte ($\frac{m^2}{s}$)

D_e Diffusion coefficient electrolyte ($\frac{m^2}{s}$)

$D_{s,anode}$ Anodic solid diffusion coefficient ($\frac{m^2}{s}$)

$D_{s,cathode}$ Solid diffusion coefficient in cathode ($\frac{m^2}{s}$)

E Energy (J)

e^+ Electrons

F Faraday's constant ($\frac{C}{mol}$)

f Mean molar activity coefficient

g Acceleration due to gravity ($\frac{m}{s^2}$)

Gr Grashof number

H Hankel matrix

h_0 Instantaneous hysteresis voltage (V)

h_1 Representative height of first well in the kinetic battery model (m)

H_2O Chemical formula for water

H_{k+1} Shifted Hankel matrix

h_m SOC related hysteresis voltage (V)

I Current (A)

i	Current in local location (A)
I_{app}	Current load applied to the battery (A)
i_e	Current in electrolyte (A)
i_{R_1}	Polarization current (A)
i_s	Current in the solid electrode material (A)
j	Lithium flux ($\frac{mol}{m^3}$)
j_{ox}	Lithium flux through oxidation chemical reactions ($\frac{mol}{m^3}$)
j_{red}	Lithium flux through reduction chemical reactions ($\frac{mol}{m^3}$)
k	Kinetic battery model conductance term ($\frac{A}{m}$)
k	Time in the discretized domain (s) or thermal conductivity (s or $\frac{W}{m \cdot K}$)
k_0	Reaction rate coefficient ($\frac{mol}{m^3}$)
k_{cond}	Thermal conductivity ($\frac{W}{m \cdot K}$)
k_{norm}	Normalized reaction rate coefficient ($\frac{mol}{m^3}$)
L_c	Characteristic length (m)
L_{neg}	Length of the negative electrode (m)
L_{pos}	Length of the positive electrode (m)
L_{sep}	Length of the separator (m)
L_{tot}	Total length of the battery (m)
N	Number of cells
N/A	Not applicable
n_i	Coefficient for charge species in chemical reactions

Nu Nusselt Number

O Observability matrix

O^{n+} Molecules containing oxygen with n positive charges

P Power (W)

$p(x)$ Sturm-louiville coefficient function

Pb Chemical symbol for lead

Q Capacity (Ah)

$q(x)$ Sturm-louiville coefficient function

R Universal gas constant $(\frac{kJ}{kg \cdot K})$

r Radial position in particle (m)

R_0 Internal resistance of the battery (Ω)

R_1 Polarization resistance (Ω)

R_{film} Film resistance of electrode $(\frac{V \cdot m^2}{C})$

R_{hyb} Hybridization ratio (W)

R_{part} Solid particle radius (m)

R_{prod} Product of the reduction process

$R_{s,e}$ Resistance of the solid electrolyte interface (Ω)

Ra Rayleigh number

$RMSE$ Root mean squared error (V)

$Rp, anode$ Particle radius of anodic material (m)

$s^{+/-}$ Charge of species in chemical reaction

SO_4 Chemical formula for sulfate

T Temperature (K)

t Time in the continuous domain (s)

t_+^0 Transference number

t_0 Initial time step (s)

$u[k]$ Input vector at current current discrete time step

U_{ocp} Open circuit potential (V)

V Voltage or volume (V or m^3)

v Kinematic viscosity ($\frac{m^2}{s}$)

$V_{electrode}$ Total electrode volume (m^3)

V_s Phase of volume (m^3)

$w(x)$ Sturm-louiville coefficient function

X Rank of individual in generation

$x[k+1]$ State space model state vector at next discrete time step

$x[k]$ State space model state vector at current discrete time step

y_1 Kinetic battery model liquid height in first well (m)

y_2 Kinetic battery model liquid height in second well (m)

z Normalized radial position within electrode particle

Z_{ind} Fitness

Greek Symbols

α Charge transfer coefficient or thermal diffusivity ($\frac{m^2}{s}$)

β Grouping of other variables for simplified algebraic reading

β_{exp} Coefficient of volume expansion ($\frac{1}{K}$)

δ Discrete change or constrictivity of the electrode material

ϵ^{Brug} Effective diffusion coefficient volume phase fraction

ϵ_{anode} Solid volume fraction of anodic material

$\epsilon_{cathode}$ Solid volume fraction of anodic material

$\epsilon_{e,anode}$ Anodic electrolyte fraction

$\epsilon_{e,cathode}$ Electrolyte volume fraction in cathode

ϵ_e Volume fraction of electrolyte

η Overpotential of battery (V)

κ Electrolyte conductivity ($\frac{m^3 \cdot A}{mol}$)

$\kappa_{D,eff}$ Abbreviation of the electrolyte potential equation ($A \cdot m$)

λ Eigenvalue of Sturm-louiville problem ($\frac{mol}{m^3}$)

λ_n N^{th} eigenvalue of the Sturm-louiville problem ($\frac{mol}{m^3}$)

ϕ Potential (V)

ϕ_e Potential electrolyte (V)

ϕ_{s-e} Difference between solid and electrolyte potential (V)

Σ SVD rectangular diagonal matrix

σ Solid conductivity in electrode material ($\frac{S}{m}$)

σ_{anode} Solid conductivity of anodic material ($\frac{S}{m}$)

$\sigma_{cathode}$ Solid conductivity of anodic material ($\frac{S}{m}$)

$\sigma_{cathode}$ Solid conductivity of cathodic material ($\frac{S}{m}$)

σ_{eff} Effective conductivity of electrode material ($\Omega \cdot m$)

θ Stoichiometric coefficient of electrode

ϱ Probability that the in individual is selected for next generation

U SVD complex unitary matrix

V^T SVD complex unitary matrix transposed

Subscripts

0 Initial

∞ Ambient

anode Anode

$Batt$ Battery

c Cross Section

cathode Cathode

cell Cell

cond Conductivity

$diff$ Diffusivity

e Electrolyte

eff Effective

EM Electric motor

Eng Engine

exp Expansion

Hyb Hybridization

ind Individual

$irrev$ Irreversible

$load$ Load

max Maximum

min minimum

neg Anode region

ox Oxidation

p Particle

$pack$ Battery pack

pos Cathode region

$prod$ product

red Reduction

rev Reversible

s Solid

$s-e$ Solid-electrolyte

sep Separator

$Series$ Cells in series

tot Total

Superscripts

$+$ Positive charge

$-$	Negative charge
$Brug$	Bruggeman coefficient

Acronyms

BC	Boundary condition
JR	Jelly Roll
SVD	Singular value decomposition
1D	One dimensional
3D	Three dimensional
ANN	Artificial neural networks
BEV	Battery electric vehicle
BMS	Battery management system
BTMS	Battery thermal management system
CLTC	China light duty vehicle test cycle
ECM	Equivalent circuit model
EPA	Environmental protection agency
EV	Electric vehicle
GA	Genetic algorithm
HEV	Hybrid electric vehicle
HPPC	Hybrid pulse power curve
ICE	Internal combustion engine
LCO	Lithium cobalt oxide

Li-ion Lithium-ion

LIP Lithium pouch

MAB Metal air batteries

NCM Nickel cobalt metal

NMH Nickel metal hydride

NN Neural networks

NR Nuremberg ring

OCV Open circuit voltage

P2D Pseudo two dimensions

PCM Parallel cell module

PDE Partial differential equation

PHEV Plug-in hybrid

RMSE Root mean squared error

SCM Series cell module

SEI Solid electrolyte interface

SOC State of charge

SOH State of health

SPM Single particle model

V2G Vehicle-to-grid

WLTC Worldwide harmonized light vehicles cycle

CHAPTER 1

Introduction

The energy crisis and the movement away from fossil fuels have become a significant concern [1] for the global economy. The Government of Canada announced in 2021 that the ban on all sales of non-zero emission vehicles will commence in 2035 [2]. In the move to a more sustainable economic system that reduces its overall impact on the planet, a reduction of carbon release is necessary across the globe. Many subsections of the economy and consumer products are responsible for vast amounts of carbon release, and a move for their respective reductions is necessary [3].

Nowhere in the economic system is the release of carbon or the use of carbon-rich fuels more evident than in the transportation sector. The transportation sector is the third highest economic carbon sector [3], and according to Amjad et al. [4], it takes up 49% of oil resources.

As the transportation sector is one of the most significant carbon dioxide contributors to the economy, corresponding reductions will significantly decrease carbon emissions and dangerous particulate matter traditionally released through the combustion of fossil fuels [5]. To reduce overall carbon emissions, a move to electrifying passenger vehicles is being adopted in Canada and across the globe [6].

One of the critical elements in this move to electrification and, thus, sustainability is the Lithium-ion (Li-ion) battery [7]. It has many benefits over other automotive solutions with its corresponding high specific energy, power density, high nominal voltage, low self-discharge rate, long cycle-life, and lack of memory effect [8, 9, 10, 11, 12]. Although there are several benefits to adopting this technology, significant power losses [13], low cycling age [14], increased capacity fade, and an increased impedance

of the battery [15] occur if not operated within an ideal operating range. The battery temperature should be kept ideally between 15 °C and 35 °C [16] to mitigate the effects previously described. This temperature-sensitive behavior with respect to the life cycle is seen in Fig. 1.0.1 where the ideal temperature working region is between 10 and 60 °C.

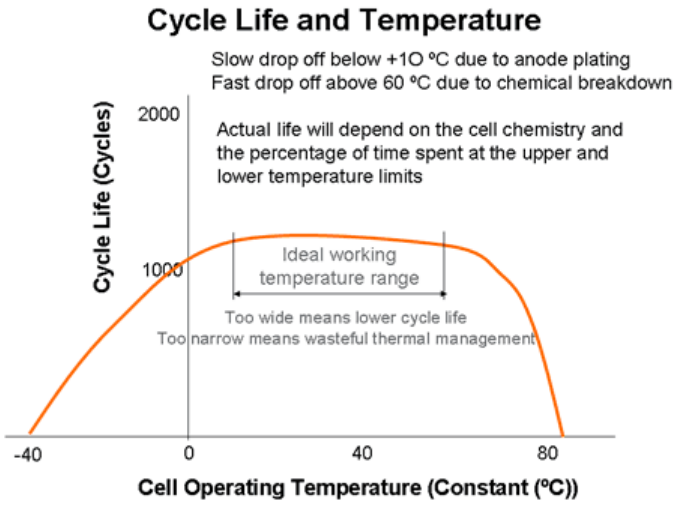

Fig. 1.0.1: Cycle life vs operating temperature; a display of ideal operating conditions [17]

Keeping the battery's temperature within an ideal range is of the utmost importance for the previously mentioned reasons. Consequently, the importance of the battery thermal management system (BTMS), whose responsibility is to manage the thermal behavior of the battery within electric vehicles (EVs), will become ever more significant in the electrification of automobiles [12, 18].

To design a well-functioning BTMS system, an understanding of the thermal profile is critical. Heat is generated during the battery's charge and discharge, and the BTMS system is crucial in keeping the temperature within the ideal range [19, 20] during these processes. An introduction to the industry's different technologies will be provided to understand the context in which this research sits.

1.1 EV Technology

Electric vehicles (EVs) differ from traditional fossil fuel-powered vehicles by replacing the vehicle's power source with an electric energy source and by typically adding an electric motor to provide torque in some manner or form [21]. Historically, the first electric vehicles were of no practical concern as manufacturability was extremely low. Producing these vehicles on a large scale limited them to singular or small groups of vehicles. There are several examples of this from the years ranging from 1828 to 1900 [22]. Nearly 100 electric taxis were running in New York City in 1899 [23]. By the year 1912, there was a peak in EV manufacturing with 33842 vehicles in the United States [22].

However, the gasoline-powered vehicle had a sharp decline in price making them affordable to the masses. Consequently, their popularity increased dramatically, and the cost of owning a gasoline-powered vehicle was achievable as gasoline was a very cheap fuel source [21]. Only recently has EV technology improved enough to be viable in today's automotive manufacturing market, with examples commercially starting in the late 1990s and early 2000s, with hybrid electric vehicles (HEVs) such as the Honda Insight [24, 25, 26].

Automotive EV technology, for simplicity, can be broken into three categories defined by the electrical source type; the source types are:

1. Batteries [27, 28, 29]
2. Fuel Cells [28, 29]
3. Capacitors [27, 28, 29]

Both battery and fuel cells are technically of the same energy source type, although they differ vastly. Both technologies convert electrochemical energy into electrical energy from a stored medium; in the case of battery technology, it is stored in a self-contained chemical structure, closed off from the environment, which typically uses the same materials during discharging and charging. The operating principle of

an idealized fuel cell can be seen below in Fig. 1.1.1. The stored hydrogen reacts with the oxygen from the air, and only water is produced [30]. For this reason, it is obvious why this technology has been a prospect for clean energy.

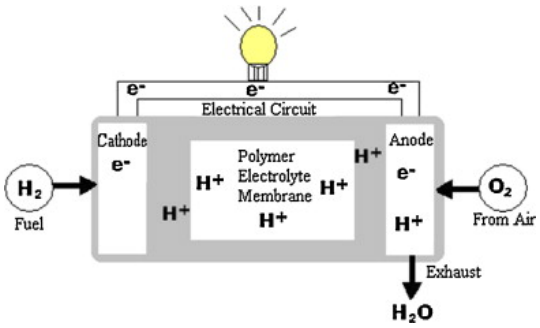

Fig. 1.1.1: Fuel cell working principle [31]

Fuel cells provide silent,vibration-free operation and excellent energy efficiency [32, 33]. However, technical challenges such as safety, hydrogen storage, hydrogen distribution, and lifetime have slowed their adoption in the industry. A more comprehensive list of the technical challenges of fuel cell adoption is shown in Fig. 1.1.2

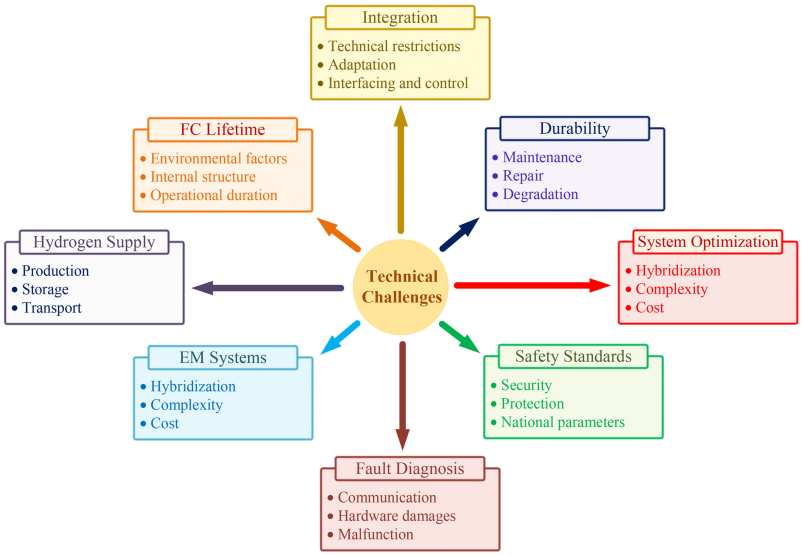

Fig. 1.1.2: Technical challenges for fuel cells [33]

The last electrical energy source of note is capacitor energy storage technology, specifically the supercapacitor. Supercapacitors are electrical components that store energy in an electric field [34].The well-known traditional capacitor stores energy through a difference of electric charge across an empty or dielectric space [35]. It is

typically visualized as charged parallel plates, which can be seen on the left side of Fig. 1.1.3. Supercapacitors are electrical elements that store electrical energy through the electric double layer effect [35, 34]. This effect is fundamentally different than a typical capacitor [35] and is shown on the right side of figure 1.1.3 below.

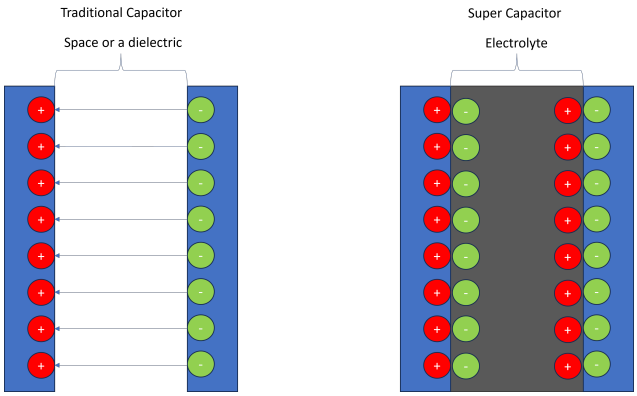

Fig. 1.1.3: Capacitor vs super capacitor difference [35]

This difference allows greater energy to be stored in the supercapacitor, orders of magnitude higher than their traditional counterparts [36]. Even though the two technologies' functional principles may differ, fundamentally, the equations for energy storage and their electric behavior remain the same [35, 37], which can be seen from equation 1.1, where E and V are the energy stored in the capacitor and the voltage across the plates of the capacitor respectively.

$$E = \frac{1}{2}V^2 \tag{1.1}$$

This storage behavior leads to an extremely high specific power, higher than Li-ion batteries [38], which can be visualized in the Ragone plot in Fig. 1.1.4, where various energy storage technologies on a specific power vs. specific energy basis are compared. A combination of both specific power and specific energy is necessary for EVs. As such, it can be seen why lithium batteries have become so prevalent within the market, as their technology has an attractive combination of these two critical characteristics.

A technology that should also be noted, due to its traction in recent research

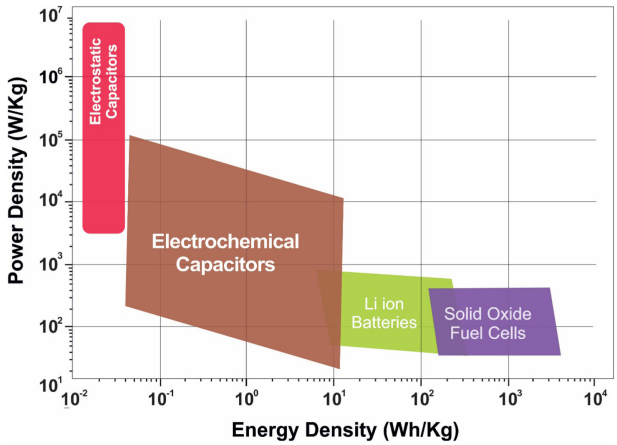

Fig. 1.1.4: Ragone plot [39]

for renewable energy storage, is flywheel technology. As more novel techniques and energy strategies have evolved, flywheel energy storage is becoming a soon viable competitor with a long cycle life, high power density, and little environmental impact [29, 40]. Currently, their high cost [41, 42], security problems [43], and the need for increased cooling [42] seem to have limited their use in current vehicles, but the integration of flywheel technology into EVs may become more commonplace in the future.

1.1.1 HEVs

The comparison of the different energy storage technologies naturally leads to a discussion about the different types of EVs that are available today. The first, which has been briefly noted, is the HEV. The HEV is a "hybrid" between an electric-powered vehicle and a traditional gasoline-powered vehicle; that is to say, there are both electrical and fossil fuel sources. HEVs are broken into many distinct categories, firstly, the level of hybridization, and secondly, into configuration categories. The level of hybridization is the amount of electrical energy provided by the electrical source as a percentage of the total power as given by equation 1.2. The configuration categories are based on the energy path distributed from the vehicle energy storage through the powertrain. Here R_{hyb}, P_{EM}, and P_{Eng} represent the ratio of hybridization, the engine power, and the electric motor power, respectively.

$$R_{hyb} = \frac{P_{EM}}{P_{Eng} + P_{EM}} \tag{1.2}$$

The categories defined by the hybridization ratios are provided in table 1.1.1.

Table 1.1.1: HEV types based on power ratios [44, 45]

Type	Description	Power
Micro	Motor is an integrated alternator starter Hybridization less than 5%	less than 2.5kW
Mild	Hybridization up to 10 %	10-20kW
Full Hybrid	Parallel Hybridization between 10 - 50 % Series Hybridization between 50-75%	Above 20kW

The second HEV categories described by the powertrain configuration are outlined below.

- Parallel HEV
- Series HEV
- Series Parallel HEV

HEVs are generally more efficient than their traditional counterparts as they can benefit from the advantages of the two distinct energy sources.

1.1.1.1 Parallel HEV

Significant simplification will be made in the following sections, as there are many complexities within the context of powertrain design and vehicle manufacturing. Parallel HEVs supply power to the wheels using both fossil fuel power and electrical power sources in parallel. The power flow through a parallel HEV can be visualized, as shown in Fig. 1.1.5.

The vehicle contains a fossil fuel-powered engine that delivers power to the wheels in parallel with a battery and an electric motor with independent energy paths. As

electrical power paths are more efficient than heat engine power paths, less energy is necessary from each energy type to deliver the same amount of power.

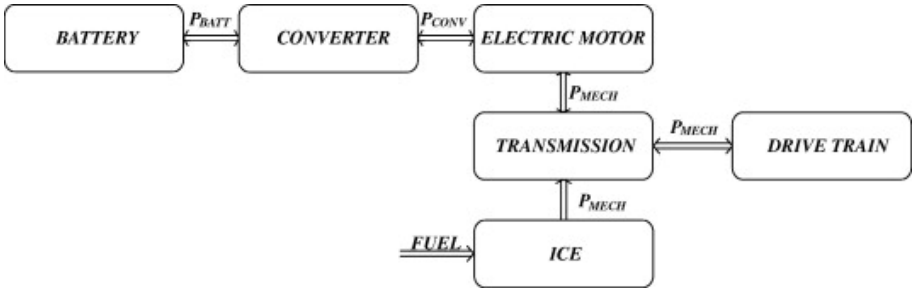

Fig. 1.1.5: Parallel HEV power-flow diagram [46]

This powertrain configuration allows for several benefits to the vehicle; the vehicle's engine can be much smaller as the battery also delivers energy through the powertrain to reach the same vehicle demands [47]. The vehicle can also recover the energy typically lost in braking to restore some of the state of charge (SOC) of the battery in use[47], which further reduces the need for a larger engine and increases efficiency.

Although there are several advantages to using the parallel HEV configuration, there are still several disadvantages. The first primary disadvantage is that two different energy sources have separate energy paths leading through the drive trains. Therefore, the manufacturing cost is significantly increased compared to that of a traditional vehicle.

1.1.1.2 Series HEV

Unlike the parallel HEV, a series HEV supplies energy from a fossil fuel source to the tires in one energy path. The fossil fuel chemical energy is converted into thermal energy and then subsequently converted into electrical energy. This usually consists of an internal combustion engine (ICE) completing the chemical energy conversion and running an electrical generator that drives electric motors, powering the vehicle to meet the energy demand [46]. Figure 1.1.6 shows a clear view of this powertrain energy path.

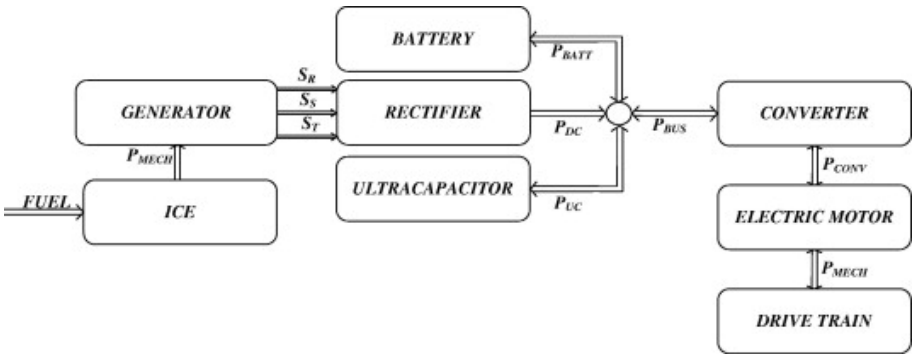

Fig. 1.1.6: Series HEV powertrain diagram [46]

In this configuration of HEV, the ICE power is always converted into electrical power. The energy conversion is completed by a generator whose output is alternating current. This energy is not only used to drive the vehicle but can also recharge the battery. As such, a rectifier must convert the alternating current into a direct current. This rectifier can transfer the electrical energy into the battery or the supercapacitor. The supercapacitor is used in the series configuration to smooth out the voltage variations from the generator. Correspondingly, the electrical energy can be simultaneously supplied from the three different electrical components in this power train layer: the battery, the rectifier, and the supercapacitor. However, as the electrical energy is in direct current, it needs to be converted again into alternating current to supply the electric motor. This energy conversion process does lead to some additional inefficiencies within the system.

As there is the sole conversion from thermal energy to electrical energy, the engine is decoupled from the wheel speed. Correspondingly the engine can be run at higher optimal speeds, which results in higher efficiency when delivering power in comparison to an ICE vehicle [48]. Less gasoline is consequently necessary to meet the vehicle's demand. Thus, a smaller engine and less fuel are necessary to power the vehicle.

Although it has a more straightforward construction than the parallel HEV configuration, the series HEV generator's size limits the design capability. This construction is primarily used in larger utility and military vehicles [49]. As with the parallel HEV, there are still more components than in an ICE vehicle, as both ICE and electrical components are still required for a series HEV. These additional components increased

the cost from that of solely an ICE-driven vehicle.

1.1.1.3 Combination HEV

In a combination HEV, parallel and series configurations are available for powering the drivetrain. This dual powering of the drivetrain is accomplished through a power-split device [46], a planetary gear set allowing two electric machines to connect to the system.

This system can be visualized from the diagram in Fig. 1.1.7 shown below.

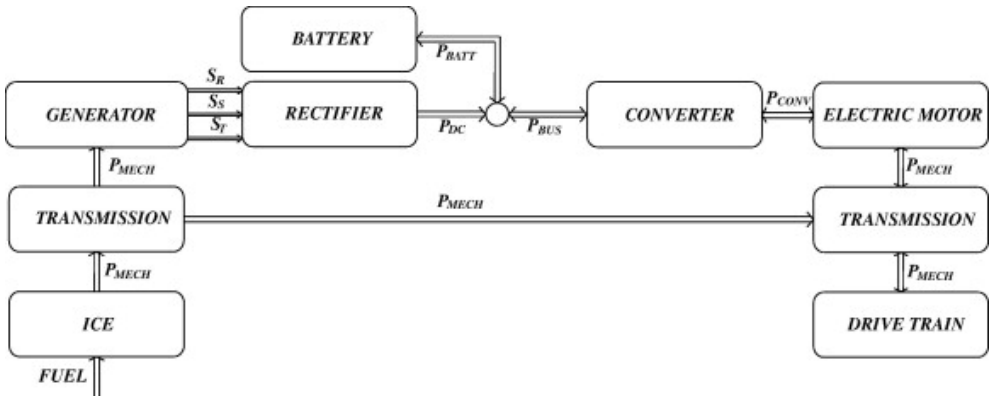

Fig. 1.1.7: Combination HEV powertrain diagram [46]

As both parallel and series configurations can be used, the energy management system of the vehicle can adjust the ICE load to achieve optimal fuel economy. This may help decrease the necessary battery size and ICE on board compared to solely series and parallel configurations, respectively [48].

Once again, as in the parallel and series configurations, added complexity and parts increase the price of the system and the potential for failure.

1.1.1.4 Plug-in Hybrid

The aforementioned complex powertrain configuration can be configured without external energy sources other than the internal gasoline power source. When a vehicle configuration can receive energy from external electric power sources such as the electric grid, the vehicles are described as "plug-in" hybrid vehicles (PHEV).

PHEVs have many advantages; a separate power source can supply the battery with more energy, and thus, a more extended range can be achieved. It reduces the overall necessity to replenish gasoline resources within the vehicle as the battery recharging can be completed without any aid from the internal combustion engine.

When a vehicle is configured as a PHEV, further capabilities can be unlocked from a consumer standpoint. One capability that has some promise and that is currently being investigated worldwide is vehicle grid (V2G) technology. V2G technology allows the user to charge and discharge energy to and from the grid at different times of the day. Charging and discharging to and from the grid can be done with concern to the time-dependent energy grid prices, which leads to the consumer's benefit and, if ideally used, can reduce the strain on the energy grid.

A well-known strenuous phenomenon in the grid, often labeled as the duck curve, is an energy demand phenomenon that reduces the attractiveness of solar energy investment. The demand for energy over the day varies from location to location, but energy use generally increases in the early morning and peaks in the evening. However, the energy supplied by the solar panels peaks during the day and decreases drastically in the evening, leading to an asymmetric net load on the electrical grid[50]. This leads to the net-energy demand curve seen in Fig. 1.1.8 below. Although maybe somewhat hard to see, this curve resembles a duck's overall profile, where the colloquial name "duck" comes from.

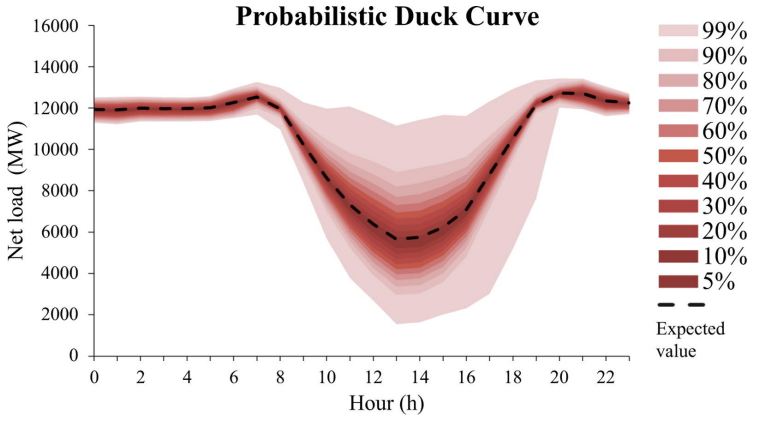

Fig. 1.1.8: Energy demand from grid over the day [50]

It can be seen that the peaks and valleys of net energy demand can be quite

different; this puts a considerable unwanted, unintended strain on the grid. This duck curve exemplifies one of the issues with solar energy. Often these strains are seen as a significant disadvantage to solar power technology as the energy cannot be fully harnessed. However, with V2G technology, this energy can be harnessed to reduce the difference between peaks if vehicles are plugged in during this time. In theory, this would mean that PHEVs, along with fully battery electric vehicles, can address other renewable resource issues other than that of just the automobile industry. That being said, this technology is still a developing field and is subject to change.

1.1.2 Battery EV

Vehicles configured with powertrain configurations without the ICE with solely an electric energy source are aptly known as battery electric vehicles (BEV). With the ever-increasing capacity of battery technology, these cars are the future of the green movement toward a more sustainable future. BEVs contain a large battery pack that stores all its energy as electrochemical energy.

BEVs were not feasible when first developed due to the energy density typically required for a vehicle's power and energy demand for extended use. However, in recent years, these issues have been addressed more satisfactorily, with battery technology becoming increasingly energy-dense and the price per kilowatt hour dropping dramatically since the invention.

A benefit of the BEV powertrain configuration related to HEV configurations is its sole power source. In comparison to parallel and complex hybrids, two energy pathways are no longer necessary as power flow from the storage components to the wheels is from a singular electric source. Fewer components are required, and the powertrain costs and design requirements are reduced. Although it is more straightforward than its HEV counterparts, this does not necessarily mean that the overall design process is without its difficulties.

Another core benefit of BEV automobile configurations is its overall power transfer efficiency. As previously noted, traditional combustion engines' efficiency is much

higher in electrical pathways. Moving all the power and energy through the electrical configuration makes the overall energy efficiency within the vehicle relatively high when compared with series hybrids or ICE vehicles.

1.2 Drive Cycles

There are many different use cases for a vehicle, and they can vary tremendously on several factors: environmental conditions, road speed limits, grades, and even the type of driver. Particularly aggressive or "soft drivers," or in other words, the driver's propensity to over -or under-accelerate in one condition over another, affects the stresses within a vehicle. These differences across the many use cases can make comparing a vehicle's loading complex in a typical use case. The industry commonly uses the drive cycle to alleviate this comparison issue. Historically, drive cycles were implemented to evaluate the vehicle's loading under standardized load conditions to compare their respective emissions.

Various drive cycles are used; however, for the most part, they can be classified as profiles of specific speed vs. time, altitude, speed vs. time, and speed vs. gear shift. In the context of EVs, the drive train of an electric power vehicle does not have any shifting; they typically have regions of constant torque vs. non-constant torque, depending on the vehicle's loading conditions.

An example of the EPA drive cycle profile is shown below. As can be seen, the test runs for around an hour of driving time with different speeds ranging across several parts of the region. Depending on the proposed vehicle application and what is deemed the representative user environment, various drive cycles with varying areas of speed, braking events, and acceleration events can be combined to verify a vehicle's power train configuration and behavior.

Different drive cycles stress the vehicle and powertrain differently, and as such, a variety of drive cycles were simulated to evaluate the behavior of the cell and module. The drive cycles of note are the EPA as already described, the Nuremberg (NR) drive cycle, and the China light truck cycle (CLTC) to estimate demands for the

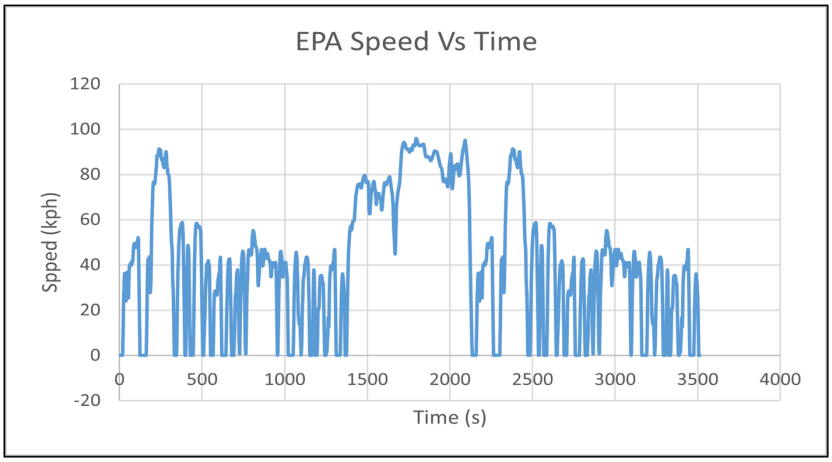

Fig. 1.2.1: EPA speed vs. time drive cycle

international market. The speed profile of the CLTC is shown in Fig. 1.2.2. A brief consequential note is that the NR drive cycle is a cycle that simulates driving around the famous Nuremberg racing circuit and, as such, is highly demanding for the vehicle.

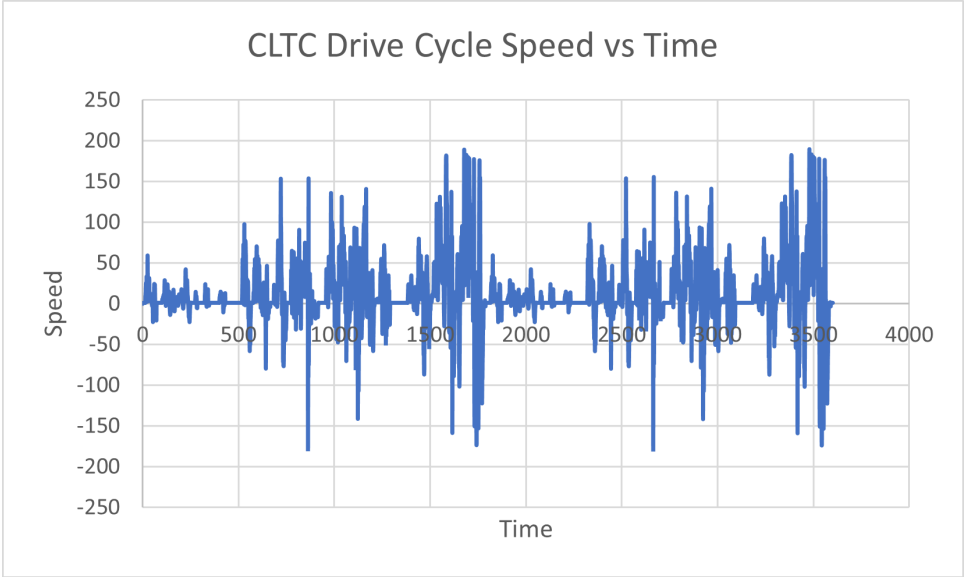

Fig. 1.2.2: CLTC speed profile

1.2.1 Hybrid Pulse Power Characteristic Cycle

Under the Department of Energy's Advanced Technology development program, the hybrid pulse power characterization (HPPC) is a tool to analyze the behavior of

battery technology [51]. HPPC is a curve in which a battery is loaded under various short pulses, from full to some minimum battery charge. These tests are done at multiple temperatures to verify the battery's power behavior.

The HPPC has two current loading profiles/curves: a charging and a discharging profile.

Before continuing to an explanation of the discharge, a concept that will be further described in section 2.2 is touched upon here. The C-rate is a normalized current rate with respect to the nominal capacity of the battery. For a clear example, a battery of 10Ah under a 5A load is at a 0.5C rate. With this, the HPPC discharge cycle can be detailed.

1.2.2 HPPC Charge

The overall structure of the charging HPPC cycle is as follows. The battery is left to rest for 2 hours to bring the battery fully to the specified intended temperature. At the start of the HPPC, it is left to rest for another 30 minutes. After 30 minutes, the battery is charged under a constant voltage constant-current and constant-voltage charging profile (CC-CV). The CC-CV charging profile is well defined within the battery community; a constant current is applied to the battery until some predefined voltage limit is reached. After the limit is reached, the battery voltage applied remains the same, and the current is decreased until the battery is fully charged. For clarity, the voltage and current profiles for the CC-CV charging profiles taken from the tests on the battery researched within the thesis are shown below in Fig. 1.2.3. For even further clarity, the first rest period for the HPPC curve is also shown in the same diagram.

The battery then undergoes another 30-minute rest period. After this rest period, the battery is fully discharged at some specified discharge rate such as C/3,1C, and 2C.

The battery's total current loading HPPC cycle is exemplified in Fig. 1.2.4.

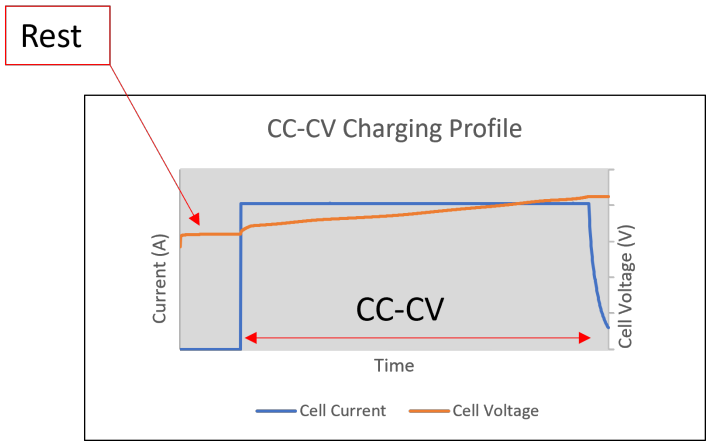

Fig. 1.2.3: CC-CV charging voltage and current profiles

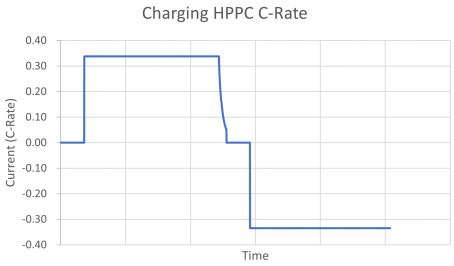

Fig. 1.2.4: Full HPPC charging current profile

1.2.3 HPPC Discharging Cycle

The discharging HPPC curve has a similar procedure to the charging HPPC. Unlike the charging HPPC which has four distinct sections (rest, CC-CV charge, rest, and constant discharge) the discharging HPPC has eight sections. These eight sections, for simplicity, will be broken down into two separate, distinct HPPC discharge curves; HPPC 1 and HPPC 2, respectively. Starting with HPPC 2, its sections are broken down into a rest section, CC-CV charge, rest, and constant discharge, which is precisely the HPPC charge profile. The HPPC 1 section is broken down into another rest, CC-CV rest, and a sporadic pulsing section. This sporadic pulsing section is made up of pulsating discharges, whose time length is the duration necessary to change the overall state of charge by ten percent. There are naturally 10 of these discharges. The HPPC curves are labeled as such because, in the testing process, these profiles are performed at multiple temperatures and various C-rates in consecutive order. For clarity, if the starting test temperature is 25 °C with a C-rate of C/5, the next HPPC discharge test (curve 2) will be completed immediately after at 25 °C with a C-rate of C/3. The HPPC test curves were completed in this specific order. HPPC curve one was completed with an immediate test of HPPC test curve two but with different C-rates. In this way, the two distinct HPPC curves were combined for the tests. These two curves are shown in Fig. 1.2.5.

This test, which measured the voltage response and the battery's temperature, was completed for three cells.

1.3 Motivation

Li-ion batteries have many advantages in comparison with other battery technologies, such as high specific energy, low discharge rate, high specific power, and no memory effect [52] behavior and characteristics are highly subject to their respective operating temperatures, [53, 54]. The temperature of operation for Li-ion batteries affects multiple aspects of their behavior. Due to this temperature sensitivity, the behavior of Li-ion batteries under realistic loading conditions should be studied to better maintain

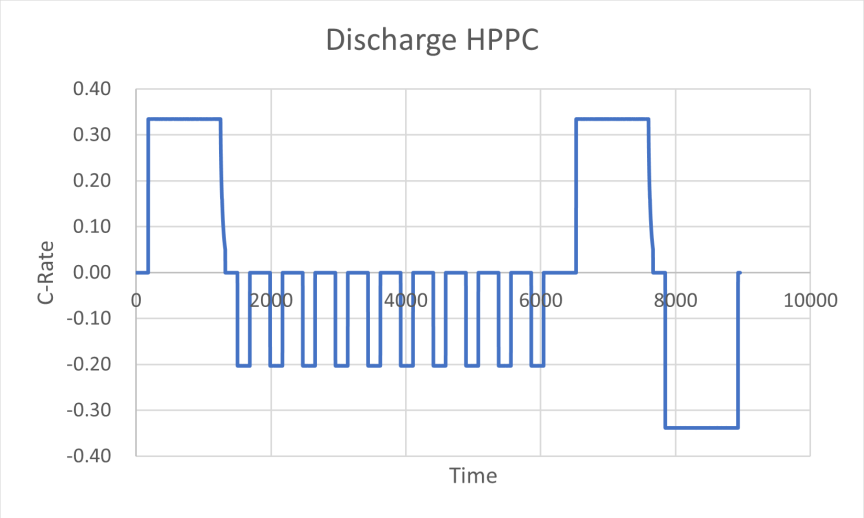

Fig. 1.2.5: Discharge HPPC profile

and design thermal management systems for continual use to keep batteries within safe operating ranges and reduce overall aging and stress on the batteries.

The temperatures within the battery, even for short periods of discharge, can exceed 50 °C. These high-temperature values can lead to increased degradation. If the battery's temperature rises even further, explosive events such as thermal runaway can occur [55]. As proof of how quickly the temperature can increase over a specified interval, Fig. 1.3.1 shows the temperature profile of an HPPC test at 25 °C with ambient conditions and a 3C current load. As is evident, the temperature increase can be large even for normal loads. Ergo, to fully and effectively design for proper temperature management for EV applications, proper thermal modeling is necessary to size the BTMS adequately.

In this modeling process, electrochemical modeling, specifically the simplified one-dimensional single-particle model, has become a standard tool in the arsenal of battery simulation techniques [56]. This technique has several advantages over other battery modeling types widely used in the industry, such as electric circuit models, namely, similar speed and higher fidelity of the inner states of the battery [57]. A challenge, however, with this model is the parameter estimation of the model [58]. The HPPC curve is a tool commonly used in the automotive industry to develop battery models [59]. Using this tool to estimate further parameters could save resources while

providing a consistent testing structure to current standards within the industry and aid in the overall thermal design process of BTMS. This use of consistent standards could extend performance and life and increase the sustainability of Li-ion battery technology.

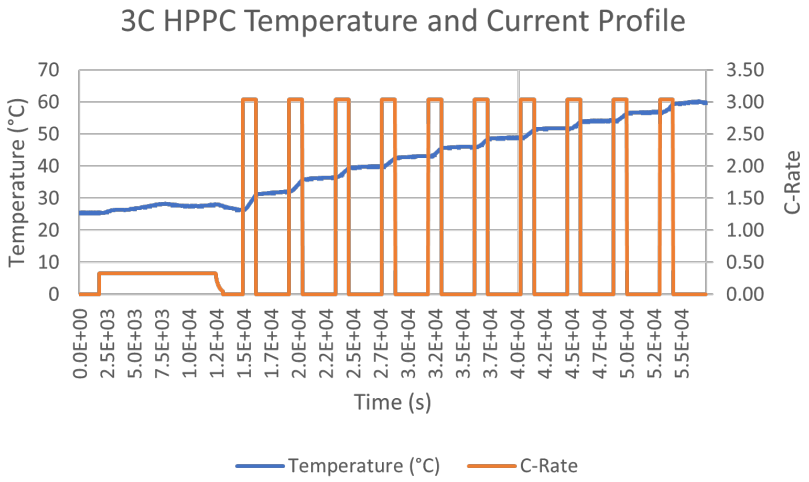

Fig. 1.3.1: Temperature and current profile of a 3C HPPC test

1.4 Objectives

Due to these problems mentioned above, like Li-ion battery's temperature sensitivity, faster-aging processes, and capacity fade in non-ideal temperature regions. It is of the utmost importance to investigate the thermal behavior of the battery at multiple levels to ensure that the performance and life cycle are enhanced concerning their usage in realistic loading scenarios. This research aimed to address these main challenges.

- To develop and validate a 1D electrochemical model using voltage estimations from requisite HPPC testing.
- To estimate the parameters of the 1D model using a genetic algorithm in conjunction with the HPPC, as mentioned above, curves
- Use these parameters to evaluate the model's effectiveness in estimating voltage behavior for the WLTC, CLTC, EPA, and HPPC cycles at ambient conditions.

- Using these estimated parameters, create heat generation profiles (which will be called heat generation maps) to estimate the heat generation behavior of the battery over the WLTC, CLTC, EPA, and HPPC cycles
- Use these heat generation maps to evaluate the thermal behavior of the battery for the WLTC, CLTC, EPA, and HPPC cycles at ambient conditions
- Use these heat generation maps to evaluate the thermal behavior of the batteries at the module level configuration
- To identify areas of thermal interest such as maximum temperatures, minimum temperatures, and temperature differences in regions at a battery level
- To identify areas of thermal interest such as maximum temperatures, minimum temperatures, and temperature differences in regions at a module level

1.5 Thesis Outline

The outline for the structure of the thesis is described below:

Chapter 2 is the background and literature review, which recounts key concepts in EV automotive applications. These explored concepts are different EV automotive storage technologies, electrochemical battery technologies' structures, topologies, and chemistries, along with anode, cathode, electrolyte, separator, current collectors, battery management systems, thermal management of batteries, thermal runaway, and cell balancing techniques. analytical modeling, equivalent circuit modeling, and electrochemical modeling are also discussed.

Chapter 3 is the methodology of the thesis research. Starting with an in-depth discussion of genetic algorithms, their configurations, and applications. The 1D electrochemical model has its equation and boundary conditions defined. The discrete-time realization algorithm is expanded. The 3D battery cell model geometry, governing equations, boundary conditions, and the 3D battery module model geometry and thermal boundary conditions are discussed. After this, an explanation of the grid independence study and an experimental uncertainty analysis are completed.

In Chapter 4, results and discussions are presented. The genetic algorithm results are displayed, and its estimation is compared with the experimental data provided from the HPPC curve. The simulated voltage curves for WLTC, CLTC, EPA, and HPPC drive cycles are then displayed with the experimental data. The estimates from the developed 3D thermal model describing the battery are then discussed for the WLTC, CLTC, and EPA at the battery level. Following these results, the temperature profiles for the WLTC, CLTC, and EPA drive cycles are then displayed at the module level.

Chapter 5 contains the conclusions and future recommendations for this research.

CHAPTER 2

Background and Literature Review

This chapter aims to review some critical background information around the core concepts of battery functionality and modeling, which includes a discussion on the typology, topology, modeling techniques, and degradation mechanisms.

2.1 Automotive Battery Technology

There are many energy storage technologies; some of the most important have been briefly discussed in section 1.1. A natural question that may arise is what battery materials are necessary to maximize performance. That question, although seemingly simple, has many complications.

Lithium batteries offer a crucial advantage when compared to their counterparts. It has a high volumetric energy density to high mass-energy density [60]. This ratio is seen graphically in Fig. 2.1.1. This ratio of gravimetric-to-volumetric density means that Li-ion batteries can fit more energy in a smaller space than their counterparts with other chemical configurations.

With the large, extended power draw during EV usage, high specific power, and specific energy are necessary, making Li-ion batteries excellent for EV design [62]. The price of Li-ion batteries was originally a barrier to entry into the market and was too expensive of an option for their configuration. However, prices have been decreasing, and at the time of writing for [63] (2016), there was already a drop of 73 % from 2010, from approximately 1000$/kWh to 273$/kWh.

Even if the evident decrease in lithium batteries is not persuasive, Stellantis has

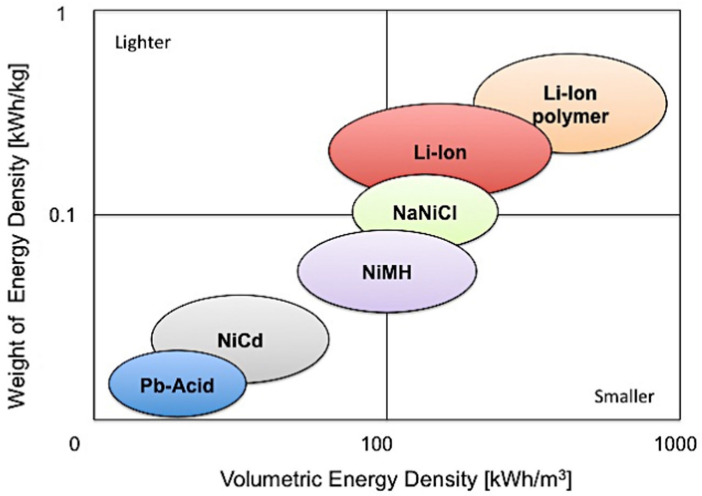

Fig. 2.1.1: Ragone plot [61]

aimed to provide a 5 billion dollar investment for Li-ion batteries in Canada [64]. General Motors (GM) announced a 35 billion dollar investment into EVs and autonomous vehicles, citing Li-ion as a critical technology and investment [65]. At least for the foreseeable future, Li-ion batteries will drive EVs.

2.2 Battery Definitions

Before discussing the various details of battery technology and its context in the automotive field, some valuable and standard definitions for the utmost clarity are provided first. The battery specifications of the Panasonic NCR18650PF are provided to clarify these definitions with a real-world example. The battery specifications for the data are seen in Fig. 2.2.1.

The ***calendar life*** of a battery is the time duration that the battery is functional. This characteristic is affected by discharging, charging, and resting. When the battery loses capacity during this resting process, it is known as calendar aging [67]. The unit for calendar life is described by a time scale of interest, typically in years.

The ***capacity***, frequently seen as nominal capacity, is the overall maximum amount of energy that the battery can store nominally [68, 69, 70, 71]. This unit is typically defined in Ah. In lithium batteries, this characteristic is directly related to the

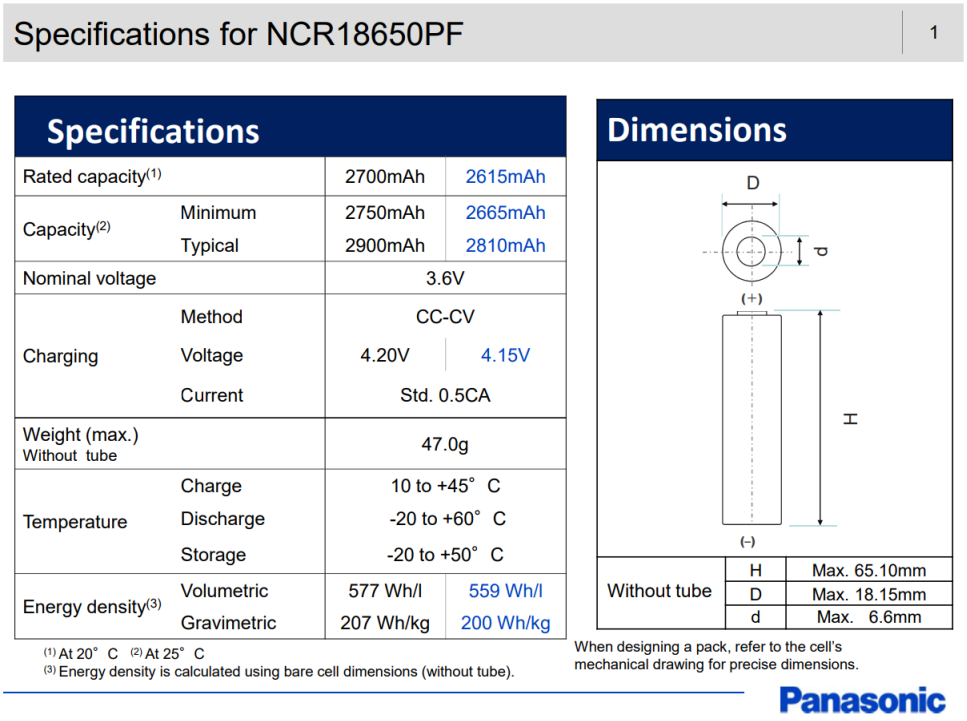

Specifications for NCR18650PF 1

Specifications

Rated capacity(1)		2700mAh	2615mAh
Capacity(2)	Minimum	2750mAh	2665mAh
	Typical	2900mAh	2810mAh
Nominal voltage		3.6V	
Charging	Method	CC-CV	
	Voltage	4.20V	4.15V
	Current	Std. 0.5CA	
Weight (max.) Without tube		47.0g	
Temperature	Charge	10 to +45° C	
	Discharge	-20 to +60° C	
	Storage	-20 to +50° C	
Energy density(3)	Volumetric	577 Wh/l	559 Wh/l
	Gravimetric	207 Wh/kg	200 Wh/kg

(1) At 20° C (2) At 25° C
(3) Energy density is calculated using bare cell dimensions (without tube).

Dimensions

Without tube	H	Max. 65.10mm
	D	Max. 18.15mm
	d	Max. 6.6mm

When designing a pack, refer to the cell's mechanical drawing for precise dimensions.

Panasonic

Fig. 2.2.1: Panasonic 18650PF battery specifications taken from [66]

amount of lithium within the battery. Theoretically, this capacity does not change with temperature, but it does vary due to various internal effects within the battery. This change in capacity can be seen in Fig.2.2.1 where multiple capacities based on temperatures are provided.

The ***C-rate*** is a normalized current rate with respect to its nominal or maximum capacity [68, 69, 70, 71]. E.g., The Panasonic battery shown in Fig. 2.2.1 has a capacity of 2900 mAh at 20 °C. Therefore, this battery at a current load of 2.9A would be under a 1C loading.

The ***E-rate*** is the energy discharge rate necessary to deliver the power required to deplete the battery fully of charge with respect to 1 hr. E-rates and C-rates are unitless multipliers expressing a ratio; however, a clear distinction is made here to alleviate any confusion. The C-rate is a multiplier showing a relationship with *current* A, while the E-rate is a multiplier based on a relationship with *power* W.

The ***cut-off voltage*** is the threshold voltage within the battery [68, 70, 69], and affects the life of the battery [72]. It can be used for both upper and lower voltage

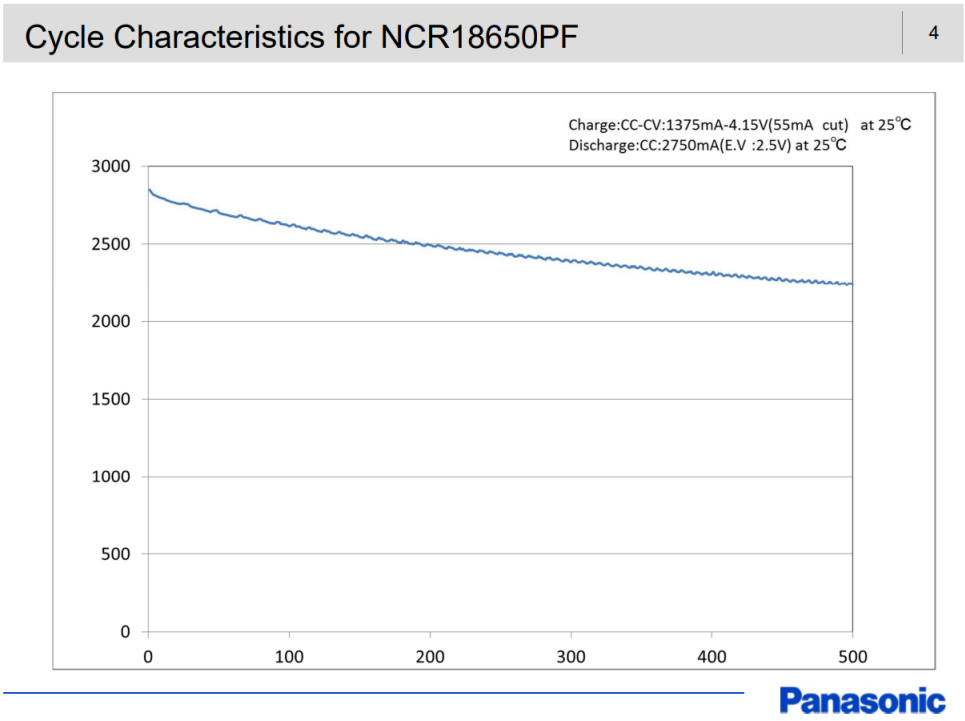

Fig. 2.2.2: Panasonic 18650PF capacity fade due to cycling taken from [66]

limits. Within this thesis, these are respectively labeled upper and lower cut-off voltages.

The ***cycle life*** of the battery is defined as the number of complete charges and discharges of the battery that can occur before some threshold of capacity loss is met [71, 69]. This definition is necessary as lithium is lost in various processes when the battery is charged and discharged. These processes are further described in detail in section 2.9. Therefore, they are not discussed at full length here. These degradation mechanisms accumulate over time, reducing the battery's capacity to hold a usable charge. For convenience, this decrease in capacity is shown in Fig. 2.2.2. The x-axis in Fig. 2.2.2 is the number of cycles completed, while the y-axis is the battery's capacity in mAh.

The ***depth of discharge*** (DOD) of a battery is the amount of capacity that has been discharged concerning its overall capacity; this value is written as a percentage [69]. As a clear example, take the Panasonic 18650PF, in the usage of 870 mAh of the 2900 mAh capacity, the DOD is 30%.

The ***state of charge*** (SOC) of the battery is its present charge with respect to its nominal capacity written as a percentage [70, 69, 71]. In the Panasonic battery example previously given with 870 mAh discharged, the total SOC would nominally be 70%. The SOC and DOD sum to 100 such that equation 2.1 holds; this is visually seen in its graphical representation in Fig. 2.1. In equation 2.1 SOC andDOD represent the SOC of the battery and the DOD.

$$SOC = 100 - DOD \tag{2.1}$$

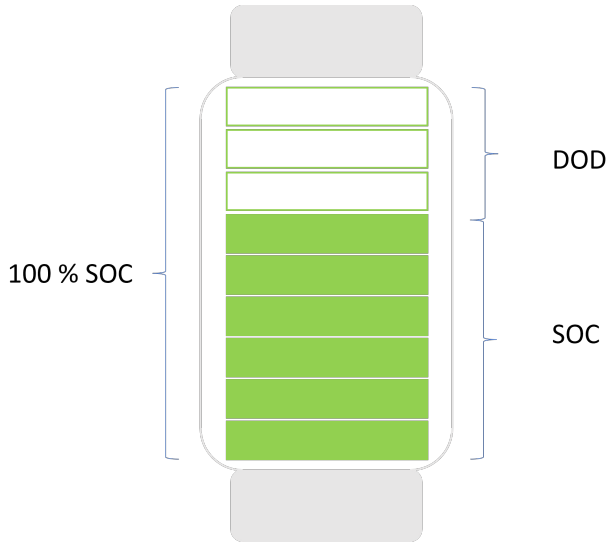

Fig. 2.2.3: Visual representation of SOC and DOD adapted from [71]

The ***energy*** of the battery is the total amount of energy supplied by a battery under a specified current [69, 70].

The ***energy density*** of the battery is the amount of energy contained within the battery per unit volume, typically with units of $\frac{Wh}{l}$ [69].In the case of the 18650PF example, this energy density is further labeled with *volumetric* energy density so as not to be confused with specific energy.

The ***specific energy***, sometimes also called the gravimetric energy as seen in Fig. 2.2.1, is similar to the energy density of a battery; however, instead of the density being with respect to volume, it is with respect to mass, often the units are reported in $\frac{Wh}{kg}$ [69]. This specification is also exemplified in the Panasonic battery

specifications in Fig.2.2.1.

The ***internal resistance*** of the battery is the resistance that is intrinsic to the battery cell [69].

The ***nominal voltage*** of the battery is the reported voltage value of the battery. This value does not represent the actual voltage that can be seen from the battery at any particular time. This difference between nominal voltage and voltage measured across the terminals is because of the nature of the internal resistance and open circuit voltage characteristics of the battery. The internal resistance of the battery changes based on various reasons: charging, discharging, temperature, and SOC [70].

The ***open circuit voltage*** (OCV) is the voltage within the battery without any external loading [70, 71]. The OCV of the battery is the difference in potentials between the anode and the cathode.

The ***power density*** of the battery is the amount of power that the battery can supply with respect to its volume, typically provided in $\frac{W}{L}$ [69].

The ***self-discharge rate*** is the time rate at which the battery loses energy under no loading. This process is due to spontaneous side reactions within the cell [71].

The battery's ***specific power*** is the power of the battery with respect to its mass, typically with units of $\frac{W}{kg}$ [69].

The ***state-of-health*** (SOH) of the battery is the relationship between its current capacity and its nominal capacity [71] and is usually represented as a percentage using the equation 2.2 [73], where SOH C_{cur}, and C_{nom}, are the battery's state of health, the capacity of the present battery which has aged, and the nominalcapacity respectively.

$$SOH = \frac{C_{cur}}{C_{nom}} \times 100 \tag{2.2}$$

The ***terminal voltage*** is the working voltage of the difference in potentials applied at the terminal. This voltage value includes the internal effects that develop in the battery, such as the battery's internal resistance. This concept is discussed more deeply in section 2.11 as seen in equation 2.18. For convenience, however, this concept

is displayed in equation 2.3, where v_{term}, OCV, i, and R_{int} are terminal voltage, the open circuit voltage, the current applied to the battery and the internal resistance of the battery respectively. Here, i is positive for a discharging current.

$$v_{term} = OCV - iR_{int} \tag{2.3}$$

To graphically clarify some of the concepts noted above, the battery voltage profiles for the Panasonic NCR18650PF taken from the experimental data provided by [74] are shown in Fig. 2.2.4 and Fig. 2.2.5 below. The battery was charged and discharged with a current applied of around 0.145 A or, with the knowledge of the battery definitions now known, a $\frac{C}{20}$ charge and discharge rate. This Li-ion battery's behavior is adapted from actual data taken from [74], so it should present the definitions with real accurate context to current technology. The battery's terminal voltages, open circuit voltage, and cut-off voltages are labeled in both figures 2.2.4 and 2.2.5 but are clarified further in the context of equation 2.3 in Fig. 2.2.5.

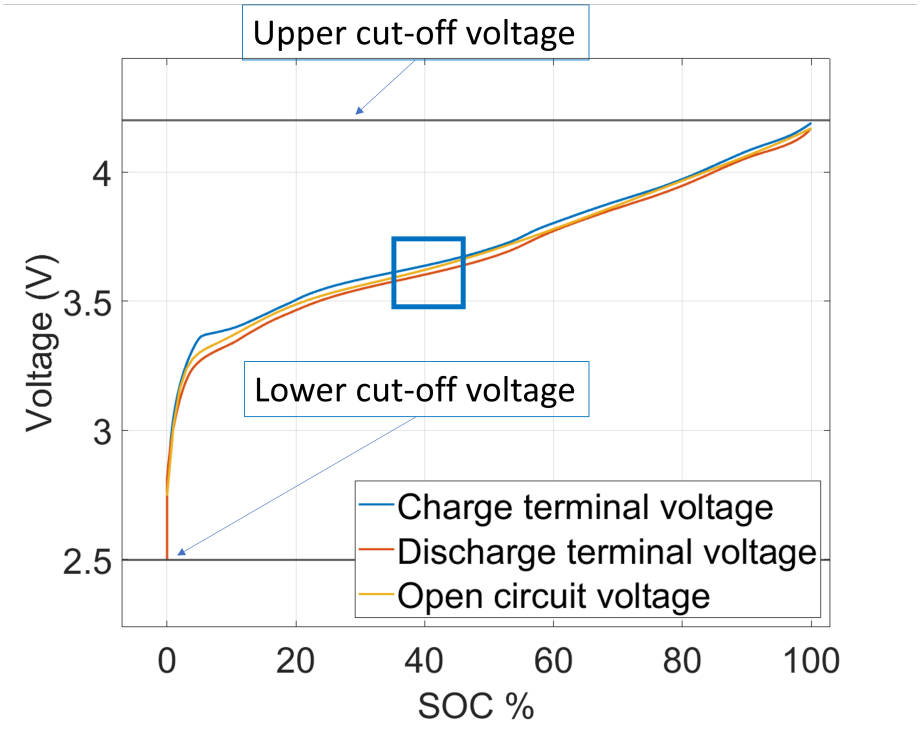

Fig. 2.2.4: Battery voltage characteristic curves of the Panasonic NCR18650PF

Figure 2.2.5 is a zoomed-in portion of the highlighted section, as seen from the

blue rectangle in Fig. 2.2.4.

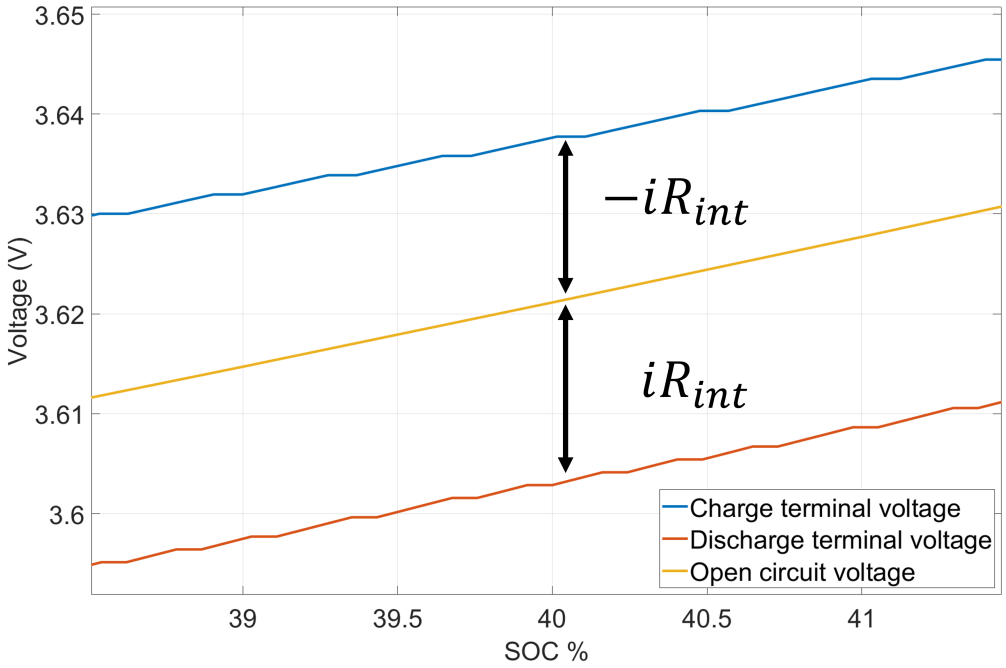

Fig. 2.2.5: Close-up of charging/open circuit voltage/discharge curves from Fig. 2.2.4

2.3 Battery Cell Structure

For a complete comprehension of the work that will be presented, an inherent understanding of the structure and nature of the battery is necessary. An electrochemical battery stores energy in the form of chemical energy and then converts it to electrical energy to supply some source [75, 76, 77, 78]. A battery is broken up into several component types, which will be discretely described for easier understanding.

The battery is made of four different component types seen in the list below [79, 80, 81, 82, 83, 78].

- Electrodes (Anode and cathode)
- Separator
- Electrolyte

- Current Collector (positive and negative)

These sections of the battery that can be seen in Fig. 2.3.1. The positive and negative current collectors aid in the process of collecting the current more effectively to deliver the power from the battery. Typically, the anodic current collector is made of copper, and the cathodic current collector is made of aluminum, although other material configurations are used within the industry.

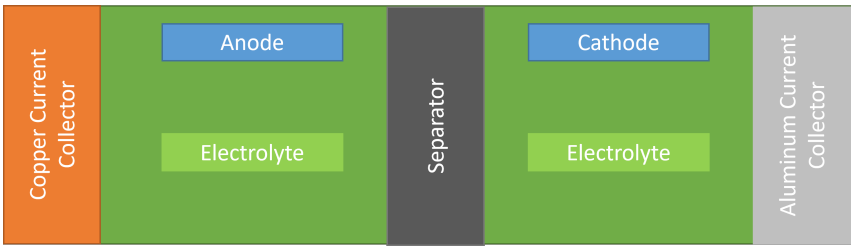

Fig. 2.3.1: Basic battery structure

The battery's separator acts as a "filter," allowing ions to travel through it without short-circuiting the battery.

The sections of the highest interest, particularly that of the electrochemical modeling problem, are the electrodes and the electrolyte. The electrolyte of the battery chemically and electrically connects the anode and the cathode, aiding in the ionic exchange between the two electrodes to enhance the chemical reaction, generating an electric current.

The next sections will clarify the general chemical reaction for the battery. Both the anode and the cathode are the electrodes of the cell. Electrodes are the structures of the battery that store and react chemically to generate electricity.

A reaction in which the charge of the atom is brought from an overall more positive charge to a more negative charge, as shown by moving from left to right in equation 2.4, is termed reduction (as the positive charge is reduced).In equation 2.4 O^{n+} represents a reactant that when donated an electron is reduced becoming R_{prod}

which represents the final reduced product. When driving in the opposite direction (right to left), the donation of electrons or, in this case, negative charge is termed oxidation.

$$O^{n+} + ne^- \underset{\text{Oxidation}}{\overset{\text{Reduction}}{\rightleftharpoons}} R_{prod} \tag{2.4}$$

When evaluating the chemistry within the battery, it is standard practice to look at half of the cell, or a so-called "half-reaction" or "half-cell." Take a reaction of zinc into an electrolyte solution where zinc and an appropriate aggregate are dissolved. For *cathodic* current, the zinc within the solution is reduced. When the zinc donates electrons from the electrolyte to the electrode, becoming oxidized, this current is defined as *anodic* current. A clear representation of this can be seen in Fig. 2.3.2, where the zinc electrode is shown on the left side of the figure. The dissolved zinc is shown over top of the (green) electrolyte, and the arrows show the direction of the current along with its designation.

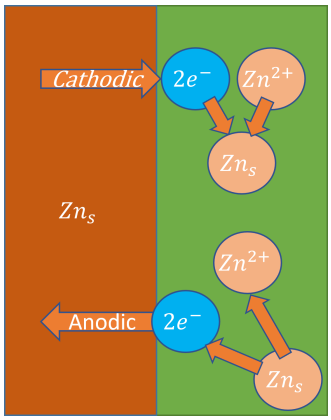

Fig. 2.3.2: Half cell reaction

The two processes above are the driving forces behind the functionality of the battery. It should be noted that although there is charge transfer across the boundary of the electrode for the half-cell reaction, the flux of energy is in the exact opposite direction at the other electrode or the other half-cell reaction, such that the conservation of charge equation, (equation 2.5) is satisfied.

$$\sum n_i s^{+/-} = 0 \tag{2.5}$$

In equation 2.5 n_i is the coefficient for the charge species $s^{+/-}$.

In this way, one can view the flow of current through the battery from the electrode to the electrolyte and from the electrolyte to other electrodes.

For completeness and clarity, an example with a lead acid battery composition will be displayed for complete understanding. Another method of naming this type of reaction is a *redox* reaction, a so-called reduction-oxidation reaction. The total number of chemicals necessary for a theoretical lead acid battery is labeled in table 2.3.1.

Anode	Electrolyte	Cathode
Pb	H_2SO4	PbO_2

Table 2.3.1: Chemical components for lead acid battery

The lead oxidizes at its half-cell reaction, as shown in equation 2.6. This reaction is the "ox" in the "redox" reaction.

$$\mathrm{Pb_{(s)}} \underset{\text{Discharge}}{\rightleftharpoons} \mathrm{Pb^{2+} + 2e^-} \tag{2.6}$$

Which reacts with the SO_4^- anion. The total anode half-reaction is equation 2.7. This reaction is the "red" in the "redox" reaction.

$$\mathrm{Pb_{(s)} + {SO_4}^{2-}} \underset{\text{Charge}}{\overset{\text{Discharge}}{\rightleftharpoons}} \mathrm{PbSO_4 + 2e^-} \tag{2.7}$$

while the half reaction at the cathode PbO_2 is written as equation 2.8 is reduced (the *"red"* in redox)

$$\mathrm{PbO_2 + 4\,H^+ + 2\,e^- + {SO_4}^{2-}} \underset{\text{Charge}}{\overset{\text{Discharge}}{\rightleftharpoons}} \mathrm{PbSO_{4(s)} + 2H_2O_{(l)}} \tag{2.8}$$

Combining the two half-cell reactions ,equations 2.7 and 2.8, the entire chemical formula becomes equation 2.9

$$\mathrm{Pb_{(s)}} + 2\,{\mathrm{SO_4}}^{2-} + \mathrm{PbO_{2(s)}} + 4\,\mathrm{H^+} \underset{\text{Charge}}{\overset{\text{Discharge}}{\rightleftharpoons}} 2\mathrm{PbSO_{4(s)}} + 2\mathrm{H_2O_{(l)}} \tag{2.9}$$

Which in its entirety is the full redox reaction. The redox reaction is the traditional chemical reaction that fuels electrochemical cells.

The anode and cathode can now be defined confidently from understanding the above processes. For processes of spontaneous reaction, what one would consider a discharge process, the flow of electrons moves from the anode to the electrolyte and from the electrolyte to the cathode.

Understanding the redox reaction that fuels traditional electrochemical cells is essential, as many concepts remain the same for Li-ion batteries. Although there are similarities, they are nor the same. New Li-ion batteries do not react in a typical oxidation pair. Where for the lead-acid battery, the lead reacted with the electrolyte to form a substrate on the surface of the electrode ($PbSO_{4(s)}$), lithium does not specifically react with the anode or cathode; on the contrary, the lithium is absorbed/-expelled into/from the structure in processes called *intercalation* and *deintercalation* [84].

This is possible because the internal structure of new cathodes and anodes are open-crystal structures, which let electrons and lithium ions permeate their structure.

2.3.1 Negative Electrode-Anodes

The function of the anode within a battery is to store the electrochemical energy at a higher energy level and then react with the electrolyte to move the stored energy to the lower energy region within the battery. Typically, this is chemically done within the self-contained battery's cathode. However, this is not necessarily true with newer battery types. Confusingly, due to the historical nature of electrical research, the notation for potentials is typically reversed from the understanding of energy levels later developed. The lower the energy level, the higher the potential energy developed

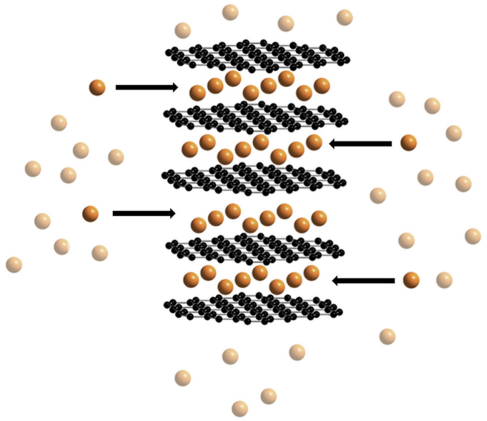

Fig. 2.3.3: Intercalation processes with graphite layers [90]

within the battery. For a more straightforward example, the potential in the cathode is at its highest when the battery is fully charged, while the potential within the anode is at its lowest.

The anode in an electrochemical cell can vary widely in different types of batteries. For example, in a pure lead acid cell, the negative electrode is a pure metal, specifically lead. However, essentially all commercial Li-ion cells use lithium graphite as the material for the negative electrode [85, 86, 87, 88]. This is done for several reasons. The graphite structure is loosely formed of hexagonal layers made of C6 groupings of atoms. During the intercalation and deintercalation processes, lithium moves in between these layers of graphite, where one Li-ion can be stored per graphite molecule (C_6). This atomic structure brings about beneficial behavior of the lithium in the interactions with the battery; namely, the lithium ions can intercalate into the spacing of the layers between the various layers of lithium graphite [86, 89]. Due to this intercalation process, the overall stress prevalent within the graphite is reduced, and as such, the overall life cycle capacity of the battery is increased [78]. The general structure of graphite and the intercalation process can be visualized in Fig. 2.3.3.

The massive scale of the structure of graphite can be essentially described as separated into three different groups: graphite, hard carbon, and soft carbon [91, 92, 60, 93]. These three different categories of the graphite structure can be seen in the image 2.3.4 below.

The sections in which the layers of graphite are uniformly parallel in the same

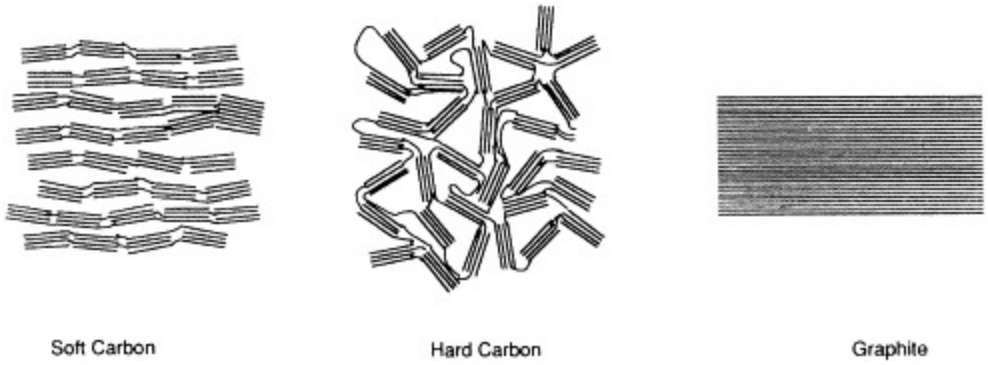

Fig. 2.3.4: Graphite structures [60]

orientation are named grains. The spaces that separate these same oriented layered regions are called grain boundaries. In soft carbon, the grains of graphite material are generally uniformly distributed and in similar directions. While in hard carbon, the grains of the graphite are randomly oriented. The orientation of these different grain layers does have an overall effect on the pathways in which the Li-ions can intercalate into the anodic material. As such, the voltage characteristics of natural and synthetic graphite are slightly different [60, 94, 93]. It is generally understood that hard carbon, due to its structure, has a higher specific capacity and cyclability but lower coulombic efficiency and affordability [95, 8]

An alternate anodic material is lithium titanate oxide. Its internal chemical structure is entirely different from that of lithium graphite. Where graphite has layers of hexagonal structures, lithium titanate oxide is a convoluted 3D structure. However, lithium can intercalate quite well with this structure, and due to the internal stability of the material, lithium titanate oxide decays much more slowly than graphite. As such, batteries made from lithium titanate oxide last and have life cycles that are much greater in magnitude than graphite. Although the life cycle of the battery can be increased, its OCV is much higher than that of graphite. Hence, the difference between electrode potentials from the anode to the cathode is reduced. This effectively reduces the battery's overall voltage, which is sub-optimal in the context of EV use. Hence, this anodic material is usually used for purposes that require low voltage and high cycle life, not EV applications.

Silicon [96, 97, 98] is a future anodic material that carries some promise. Silicon

theoretically has an ultra-high specific capacity of approximately 4200 $\frac{mAh}{g}$ [99], which in comparison to graphite at 372 $\frac{mAh}{g}$ is more than an 11-fold increase. Batteries that use silicon as an anodic material can significantly increase their power-to-weight and energy-to-weight ratios. Silicon also has a low working potential and is more environmentally friendly [99, 100]. The downside of using this anodic material currently is silicon's tendency to volumetrically swell when charged [101, 96, 102]. This creates significant stress on the battery due to charging and discharging. Work is currently being completed to mitigate these effects based on multiple technologies. An example of a technology under development is silicon channels surrounded by other anodic material such that the swelling of the silicon does not damage the overall structure [97].

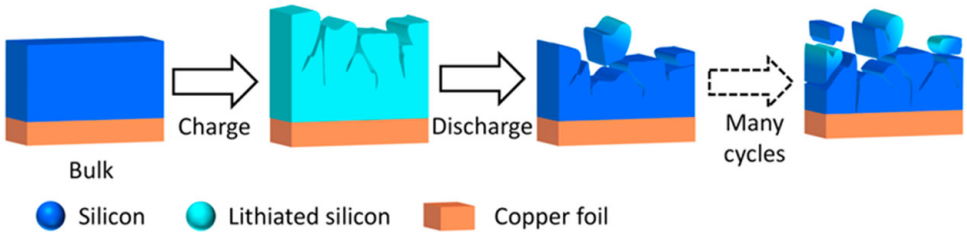

Fig. 2.3.5: Silicon break down due to swelling [96]

2.3.2 Positive Electrode-Cathodes

There are several cathodic materials on the market, but for a brief overview, the more common ones will be discussed here. One particular cathodic material is lithium cobalt dioxide (LCO). LCO was one of the first cathodic materials used with lithium [103, 104, 105, 106]. The overall structure of LCO is planes of cobalt and oxygen that are tightly bonded together. These bonds are extremely strong; when lithium intercalates into the spaces between the LCO layers, the overall structure and material of the cathode remain unchanged. Accordingly, charging and discharging lithium into the material can be done frequently and reversibly. Its structure is layered similarly to graphite, which lets the lithium-ions move in between the layers. LCO has a high theoretical capacity, low self-discharge, and good cycling performance [107]. At

the same time, its downsides are its high cost [108], capacity fade, and low thermal stability [109, 110].

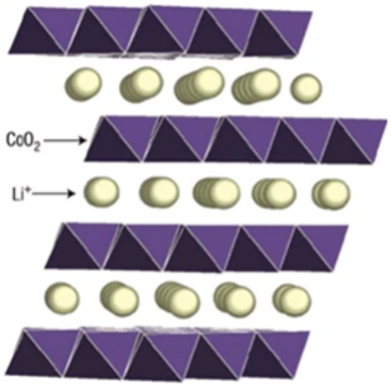

Fig. 2.3.6: Layer LCO structures [111]

LCO is commonly present in small portable electronic devices; however, it suffers from issues when trying to scale up for more significant energy demands. Cobalt is extremely rare and toxic. Thus, the disposal of batteries becomes an issue. Nickel can be added to the structure to replace cobalt; however, it is thermally unstable. Aluminum, chromium, and manganese can also substitute cobalt, but each element varies the behavior of the overall structure in its own unique way. An example of this element substitution is seen in the common lithium manganese oxide (LMO). LMO is a cathodic material with an octahedral cubic spinel structure [110, 112], which is a complicated, convoluted 3D structure that has the property where lithium can diffuse into the material in all three directions. This structure can be seen in Fig. 2.3.7. These openings decrease its effective internal resistance. The benefits of LMO over LCO are its affordability and safety [113, 110, 114, 115]. However, it has a shorter lifetime due to manganese dissolving into the electrolyte under acidic conditions [116, 114].

The most commonly used cathodic mixture is NSM, also known as NMC [118], which is a blend of nickel cobalt and manganese that has properties that mix all of the material blends. NMC cathodic materials are the most common cathode material in EV applications today. However, it should be noted that NCA, a mixture of cobalt and aluminum, is solely used for Tesla vehicles.

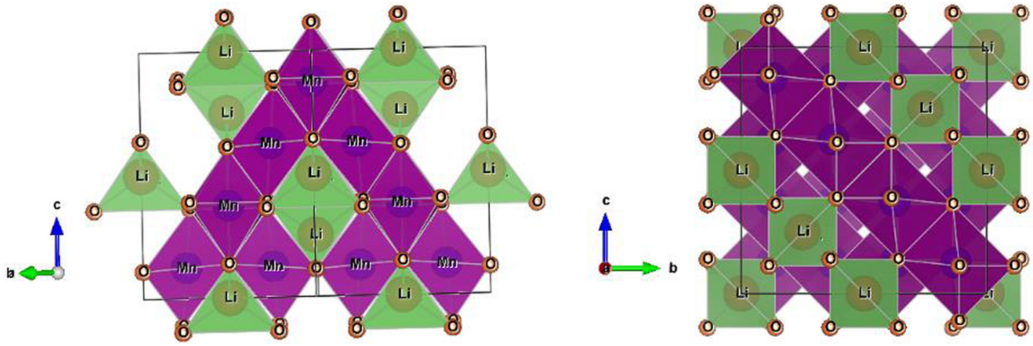

Fig. 2.3.7: LMO cubic spinel structure [117]

Lithium iron phosphate is another common cathodic material of particular note to automotive applications ($LiFePO_4$).This material has an olivine structure, [119] exemplified in Fig. 2.3.8. This material is inexpensive and non-toxic, and it is the most thermally stable of all the cathode materials [120]; however, there is a substantial voltage drop (around 0.5V) which reduces its overall energy density [114]. The electronic conductivity is also much lower than that of other cathodic technologies, being around $10^{-9}\frac{s}{cm}$ [121, 120]. This, in comparison with LCO at 10^{-4} [122], and LMO at $10^{-}-6$ [123] shows in context how significant the difference is and accordingly how disadvantageous this lack of conductivity becomes.

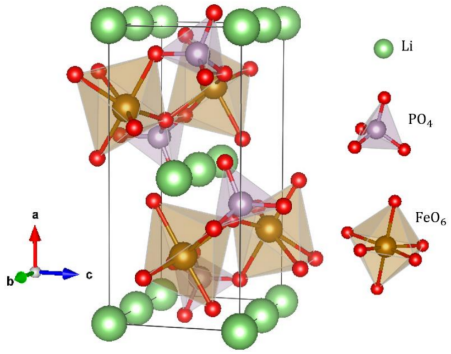

Fig. 2.3.8: LiFePO_4 olivine structure [124]

Overall, some common cathodic materials used within the automotive industry for battery use have been described. Each, with its performance standards and advantages, provides a specific behavior type typically chosen based on design criteria. A more graphical comparison of some of the essential characteristics of the cathodic materials is shown in Fig. 2.3.9 below.

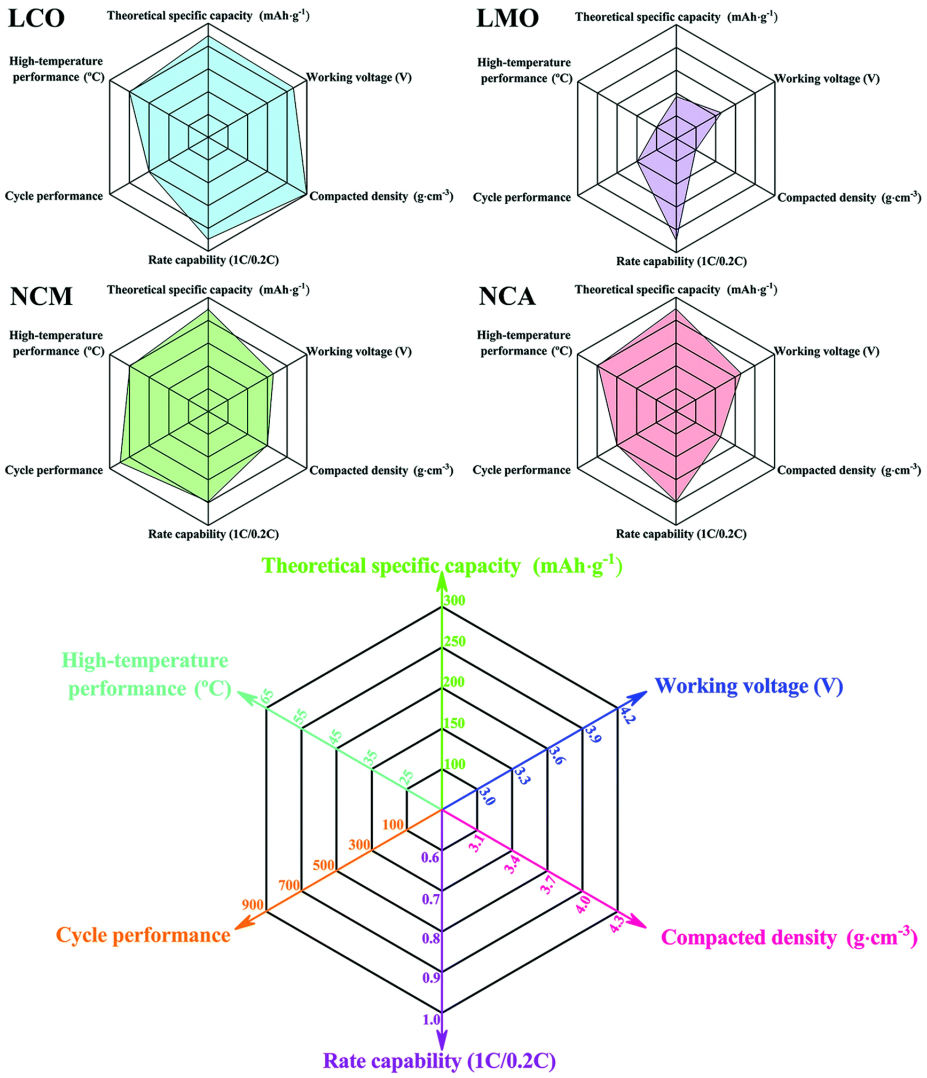

Fig. 2.3.9: Different common cathodic materials performance comparison [125]

2.3.3 Electrolyte

Electrolytes are fundamentally made up of two sub-components: solvents and salts. The solvent is typically a liquid that dissolves a solute without any change in its chemical composition. At the same time, the salt is dissolved in the electrolyte and aids in the chemical functioning of the battery. As such, the electrolytes of automotive batteries are typically made of solvents that can dissolve sufficiently high concentrations of lithium salts and have low viscosity to aid in the transport of ions [126]. Lithium batteries require voltages above 2 volts, often in excess of 3 or even full 4 volts. Due to this voltage range, non-aqueous electrolytes must be used. The most common solvents that are used in Li-ion batteries are ethylene carbonate, propylene carbonate, dimethyl carbonate, and ethyl methyl carbonates [114, 127].

The electrolyte acts solely as an ionic bridge between electrodes, so the choice of salt is important, unlike the different solvents. The most common salt by far is lithium hexafluorophosphate ($LiPF_6$) [128, 129, 127] which when dissolved becomes a Li^+ and a PF_6^-. Its ubiquitous use is due to a combination of characteristics: high conductivity, stability up to 5V, and corrosion prevention of the aluminum current collector [114]. Two major challenges with this salt are $LiPF_6$ disintegrates at temperatures above 70 °C. [114, 130] and it also reacts very destructively with water which can cause damage to the battery [130, 131]. Acids and water are not purposely added to the electrolyte under normal conditions. However, moisture during manufacturing is sometimes unknowingly added, which reacts with the salts, reducing the batteries' overall lifecycle.

2.3.4 Separator

The separator is a permeable membrane that physically and electrically separates the cathode and anode. If there is a short circuit between the two electrodes, large amounts of current and voltage will flow through the two sections of the battery, potentially causing a fire or explosion [130]. Although the separator electrically separates the anode and cathode, it still enables free ionic transport but is chemically

stable with the electrolyte and electrode materials [132, 133]. These functions are necessary for the battery functionality [134]. Separators are broken into three categories [132]

- microporous polymer membranes
- non-woven fabric mats
- inorganic composite membranes

The differences between these technologies are their manufacturing processes and their overall characteristics [135, 136]. Microporous polymer membranes are most commonly used due to their low costs and good mechanical properties [130]. In contrast, non-woven mat technologies are used as separators but not usually in Li-ion batteries. Inorganic composite membranes are gaining popularity for high voltage applications such as EV usage due to their high melting points and thermal conductivities but are still sluggishly being uptaken in the industry as a result of low tensile strength and extra weight [130].

2.3.5 Current Collectors

Current collectors are conductive materials placed on each electrode to aid in charge distribution. During battery operation, it is through the current collectors that the electric charge is passed [137]. During the manufacturing process, the anodic and the cathodic materials, along with other additives and binders as seen in Fig. 2.3.10, are attached to these current collectors and then formed into their respective battery structure types. Current collectors are subjected to extremely harsh chemical environments and, as such, must be non-reactive [139, 140]. Typically, the current collectors for the cathode and the anode are aluminum and copper, respectively[141, 85, 142, 143]. These materials are chosen as the electrode potential that is necessary to dissolve these two metals is much higher and lower, respectively, than the anodic and cathodic materials.

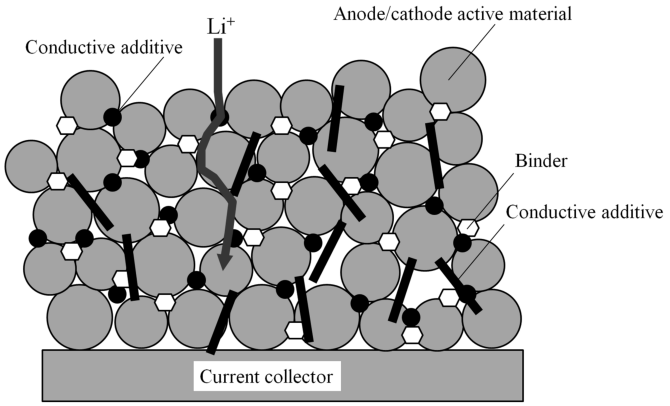

Fig. 2.3.10: Active electrode material on current collector [138]

The current collectors' design affects aspects of the battery's cyclability, energy density, and the rate performance of the cell[138], and as such, must be mechanically robust, lightweight, inexpensive, electronically and thermally conductive [140] which are further reasons why traditionally these metals, aluminum, and copper, have been used.

2.4 Automotive Battery Chemistries

There has been extreme development since Volta's original work on the first battery developed in the 1800s. Where previously there was only the electrochemical cell structure of a singular battery type, it seems new batteries are displayed on the news every several months. For completeness, previous and new technologies will be mentioned and briefly discussed so an entire picture is formed of the various automotive choices in the industry, both historically and for the future.

2.4.1 Lead Batteries

A brief explanation of the basic functionality of the lead acid battery has already been provided in equation 2.9 as well as its half-reactions, seen in equations 2.7, and 2.8. Lead acid batteries have been the most common battery for automotive implementation. Lead batteries powered the cranking of the ICE engine and supplied current

for the vehicle's auxiliary loads for many years due to their safety performance, low cost, and excellent recyclability [144, 145]. These batteries are still used in HEVs for auxiliary power and as the primary electric source in micro hybrids [26]. Lead batteries are also responsible for the basic micro-hybrid functions [146] the functionalities of the various sub-categories of hybrids are shown below in table 2.4.1.

Table 2.4.1: Powertrain functionalities of the different hybrid classifications adapted from [146]

Capable Hybrid Classification	Responsibility
Micro,Mild,Medium,Full	Powering electric accessories
Micro, Mild, Medium, Full	Comfort cranking
Micro,Mild,Medium,Full	Limited regenerative braking
Mild,Medium,Full	Crank to idle
Mild,Medium,Full	Torque smoothing
Mild,Medium,Full	Launch assist
Mild,Medium,Full	Electric powerpoint
Medium,Full	Medium Power assist
Medium,Full	Full regenerative braking
Full	Full power assist
Full	Electric drive

Although these advantages exist, lead acid batteries have low specific and volumetric energy ratios [61], making them unsuitable for more demanding battery applications such as full-hybrids and BEVs.

2.4.2 Nickel Metal Hydride

Nickel Metal Hydride (NMH) batteries are secondary batteries with a potassium hydroxide (KOH) electrolyte, a nickel oxyhydroxide anode, and a metal hydride cathode [147]. Their general components are shown in Fig. 2.4.1. These batteries were in-

troduced in 1991 by Sony as a replacement to the nickel-cadmium battery, which was expensive and environmentally unfriendly [148]. Although slowly being overtaken within the HEV market, they are still used within the industry, such as in the RAV4L and the Honda EV plus[149]. The NMH advantages are a lack of memory effect and relatively high specific energy, although not as high as Li-ion batteries [61].

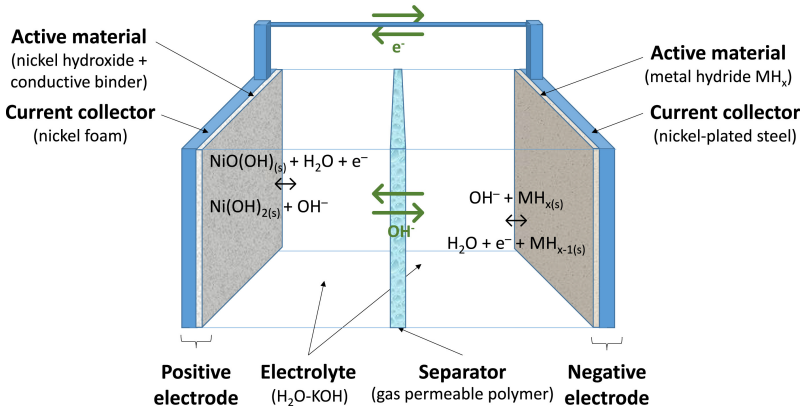

Fig. 2.4.1: NiMH basic structure [150]

2.4.3 Li-ion battery comparison

At this point in writing, Li-ion batteries have been well described and have no requirement for further explanation. In the context of the previous battery chemistry sections, Li-ion batteries, when compared to the technologies mentioned earlier, have a superior specific energy density, specific power density, and cyclability. These comparisons are seen in the table 2.4.2.

2.4.4 Potential Future Battery Technologies

Although this research was done on current Li-ion technology, some notes on potential future technologies will be made to show the context of this research in the developing field.

Metal-air batteries have gained some traction within the mainstream view as a possible replacement for the more widespread Li-ion batteries, and a brief look into

Table 2.4.2: Comparison of battery chemistry characteristics adapted from [151]

Battery Chemistry	Specific energy $\frac{wh}{kg}$	specific power $\frac{wh}{kg}$	Self-Discharge (% per 24h)	Recharge Cycles
Pb-acid	40	180	1	500
NiMH	70	1000	2	1350
Li-ion	125	1800	1	1000
Li-ion Polymer	200	3500	1	1000

their functionality is thought to bring light to this new, evolving, and potentially promising field.

As discussed previously, traditional batteries typically use a cathode, anode, and electrolyte to transfer energy between high-energy and low-energy states through an electrochemical reaction. The conventional battery contains all the necessary chemicals within its structure. More clearly stated, a traditional battery has all its usable materials in its cathode, anode, electrolyte, and separator.

However, metal-air batteries (MAB) do not physically store all the usable materials necessary for the reaction to generate electricity. MABs use the oxygen in the surrounding air under load to react with the chemistry within the battery. Due to this, all the mass necessary to fundamentally complete the reaction does not need to be included during manufacturing. Thus, the energy densities of these metal-air batteries can be extremely high. These energy densities have even been reported to be as high as 13000 $\frac{wh}{kg}$ [152] or 46.8 MJ/kg. MABs show energy densities that are even more impressive in comparison with gasoline, which is roughly around 45 MJ/Kg. A comparison is visible in Fig. 2.4.2 provided by [153] showing the relative energy densities of MABs compared to current Li-ion batteries.

MABs are exceptionally dense and could potentially alleviate some of the energy density disadvantages that the current battery technology has reached in comparison with its traditional fossil-fueled competition.

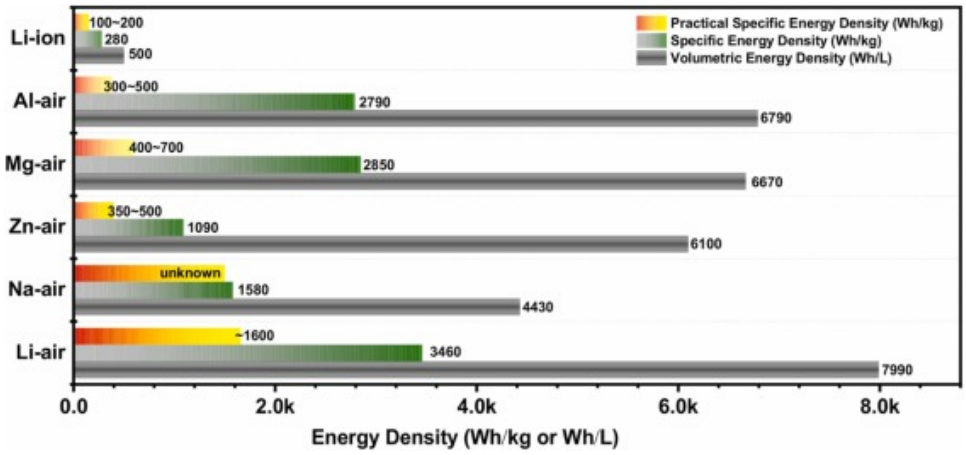

Fig. 2.4.2: Metal air battery densities [153]

Promising as the densities of these batteries are, MAB suffers from slow electrochemical oxygen reactions [153], which makes them currently unsuited for EV applications. It is also mentioned that the overall theoretical voltages of the MABS are generally lower than that of current Li-ion batteries.

2.5 Battery Topologies

Not only does the chemistry vary across batteries, but so does the shape or topology of the batteries. For simplification, a battery can typically be classified under the following topologies [154].

- Cylindrical
- Pouch
- Prismatic

The structures of the various shape formats of Li-ion batteries contain very similar components. The electrodes, as can be seen in Fig. 2.5.1, are typically coated on both sides of a singular current collector in a process known as "coating" [155]. The coating is completed for both the anodic and cathodic materials on separate current collectors [156].

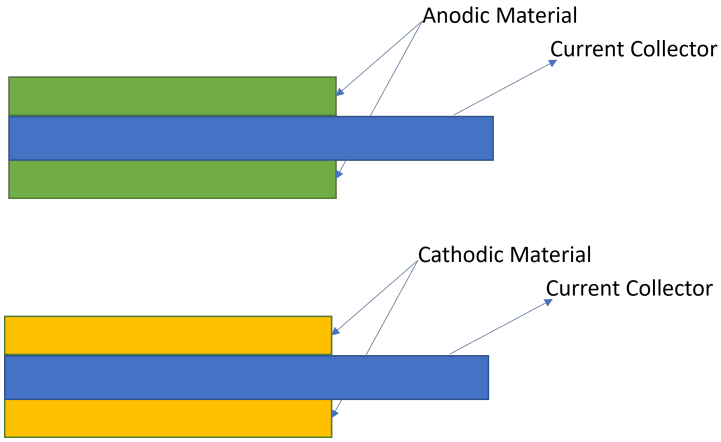

Fig. 2.5.1: Electrode plating structure adapted from [84]

For cylindrical batteries, the six sections of the battery (negative current collector, anode, electrolyte, separator, cathode, and positive current collector) are placed side by side in layers which are then wound or "rolled," around an inner core, sometimes called a mandrel [157, 156].

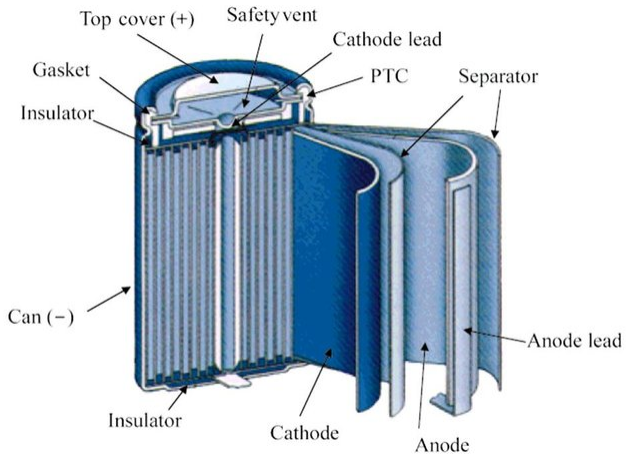

Fig. 2.5.2: Cylindrical battery structure taken from [158]

This electrical battery is sometimes also called a "jelly roll" due to its resemblance to the well-known desert with the same shape.

Cylindrical cells are widely used in industry due to their mechanical strength and manufacturability [159]. However, they have low packing capacity, resulting in an overall lower energy density [159]. It should also be noted that for cylindrical cells, as they are heated, there is minimal to no swelling compared to the pouch and prismatic

cells [160].

These cylindrical cells are the easiest to manufacture with robust processes and machinery [161]. The packing efficiency is low due to their cylinder shape, as when the cells are either in series or parallel, the adjacent tangent circular shapes leave small gaps. On the positive side, these gaps provide an intrinsic coolant pathway for air or some other coolant [162].

Prismatic batteries have a similar structural nature to that of cylindrical cells; the electrode-coated current collectors are wound around a center in the same way that a cylindrical cell is made. However, the core is made of a rectangular mandrel, and this entire structure fits into the prismatic container [162]. As the prismatic batteries can be placed directly adjacent to each other, this can increase the packing efficiency with respect to cylindrical cells. However, prismatic battery cells are typically placed with spaces between each addition cell so that coolant may flow; this increased space reduces the overall packing efficiency [162]. The spacing between prismatic cells should be reduced to maximize the overall energy density of the vehicle. Compared with cylindrical cells, prismatic cells have a thicker case. Thus, its overall energy density is lower than that of cylindrical cells, but still, with this reduced density has a higher packing efficiency [160]. Figure 2.5.3 shows prismatic batteries with their structure. A key disadvantage to the prismatic cells is their tendency to swell during usage, which is a primary method of failure [163] for this topology.

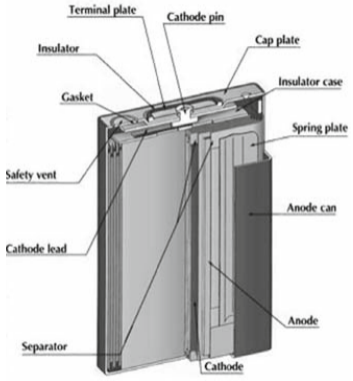

Fig. 2.5.3: Prismatic battery structure taken from [164]

Pouch cells (LIP) are created by layering sheets of anode-separator-cathode assem-

blies [160] and then packaged into a pouch. The pouch is an aluminum film with an electrically insulating coating to prevent electrolyte corrosion. As the pouch is light, the cell's energy density and packing efficiency are high but susceptible to physical damage. LIPs are also prone to swelling, and not only can this cause damage, but this swelling also reduces the battery's effective conductivity, reducing its ability to cool [165].

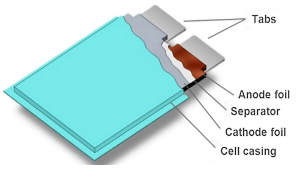

Fig. 2.5.4: Pouch battery structure taken from [160]

These types of cells are being more frequently adopted in the automotive industry due to their structure having less casing and increasing the overall energy-to-weight ratio of the entire battery pack for the vehicle [166]. The costs associated with pouch cells are also low due to fewer components [161]. The LIPs' overall structure is shown in Fig. 2.5.4.

As the LIPs can be placed directly adjacent to each other, unlike that of the cylindrical cell, spaces need to be added in the design phase to apply coolant [16].

2.6 Battery Pack Structure

The voltage and current that a single cell can supply are not nearly enough to run a vehicle; correspondingly, to meet the EV power demands, the cells must be configured suitably to realize the necessary vehicle behavior. The next component level that the cells are configured into is known as the battery module configuration [28]. These battery modules are then combined to form a battery pack that so the pack can meet the total demand of the vehicle.

2.6.1 Module Structure

A module is a collection of cells placed in series or parallel, along with other necessary components for safety features such as temperature sensors, voltage, cage monitoring system, and a battery management system [162]. These modules are then configured to fully complete a battery pack [167, 168]. An example of the module comprised of prismatic batteries is shown below 2.6.1.

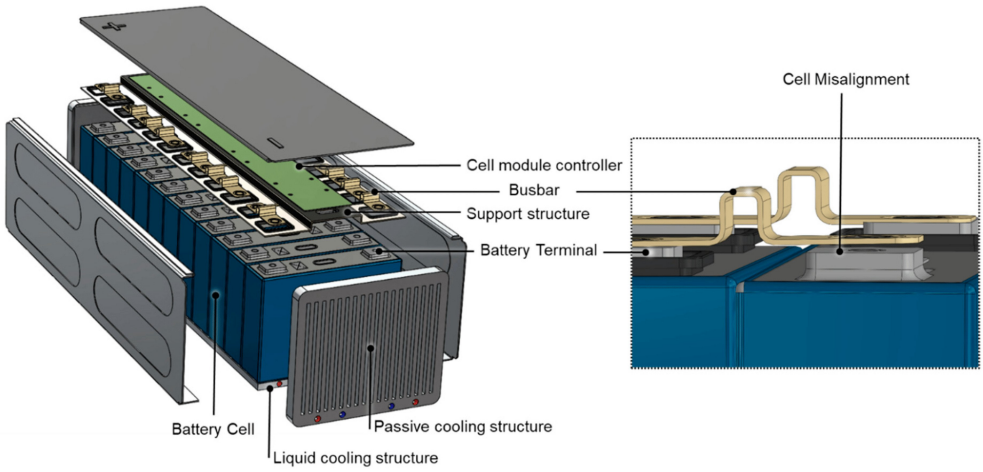

Fig. 2.6.1: Representation of an automotive battery module [167]

For clarity in the subsequent discussion, the demand that is required from the battery to the vehicle will be discussed as power demand. Power drawn from the battery can be modeled with the equation 2.10 shown below for electrical power, where $P\,V$ and$I$ represent power, voltage, and current respectively.

$$P = VI \tag{2.10}$$

This shows that for the overall battery pack to supply enough power to the vehicle, one can increase either current and/or voltage. Placing cells in series increases the effective voltage so that their voltage accumulates as described by equation 2.11 shown below, where $V_{pack}\,N_{series}$andV_{cell} are the voltage of the pack, the effective number of cells in series, and the voltage of the cell.

$$V_{pack} = N_{series}V_{cell} \tag{2.11}$$

This voltage increase leads to an increase in the module's power output. However, one particular downside to this scenario is that although the voltage output of the module has increased, the current production of the module in comparison with a single cell has not.

To solve this issue of stagnant current, the cells can be placed in parallel such that the current distribution across each of the cells is reduced, effectively increasing the configuration's capacity. However, as the cells are stacked in parallel, the effective voltage across the parallel cells must be the same. Thus, this reduces the overall voltage one can achieve. Effectively, these configurations are combined to meet power demand, either module wholly comprised of the cells in series (SCM) represented in Fig. 2.6.3, consisting of cells completely in parallel (PCM) as seen in Fig.2.6.2, or a combination of both, which will be given the acronym (CCM).

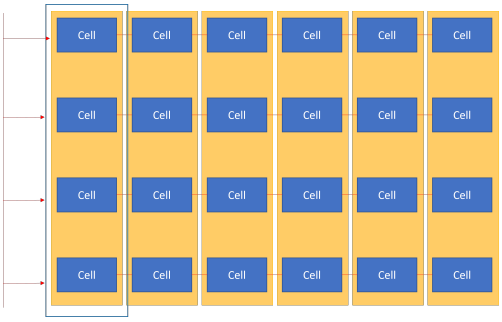

Fig. 2.6.2: PCM structure

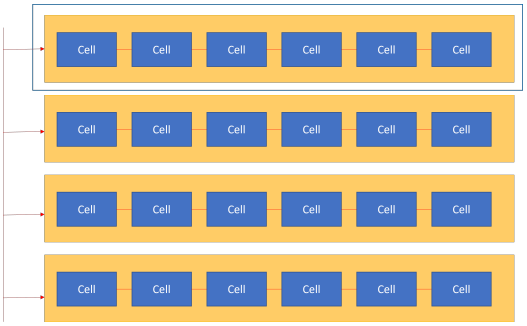

Fig. 2.6.3: SCM structure

As can be seen in Fig. 2.6.2 and Fig.2.6.3, by placing the various SCM and PCM modules in parallel and in series, the disadvantages of each of the individual modular designs can be effectively reduced although not completely eliminated.

Although modular topology is excellent at solving the power distribution issue within the battery pack, it is also done for other logistical and cost reasons. To reduce the nonrecurring engineering costs by subdividing the battery pack into these predefined modules, companies and teams can design different configurations while minimizing time on the specific design of the modules. This reduces time and costs for almost all involved [169].

2.7 Battery Management System

Regardless of configuration or battery application, the battery management system (BMS) has several functional requirements that it needs to supply. These requirements are sensing, high voltage control, battery protection, interface, performance management, and diagnostics [170]. Although not explicitly stated, these categories can be seen in an outline of the finer responsibilities of the BMS shown in 2.7.1.

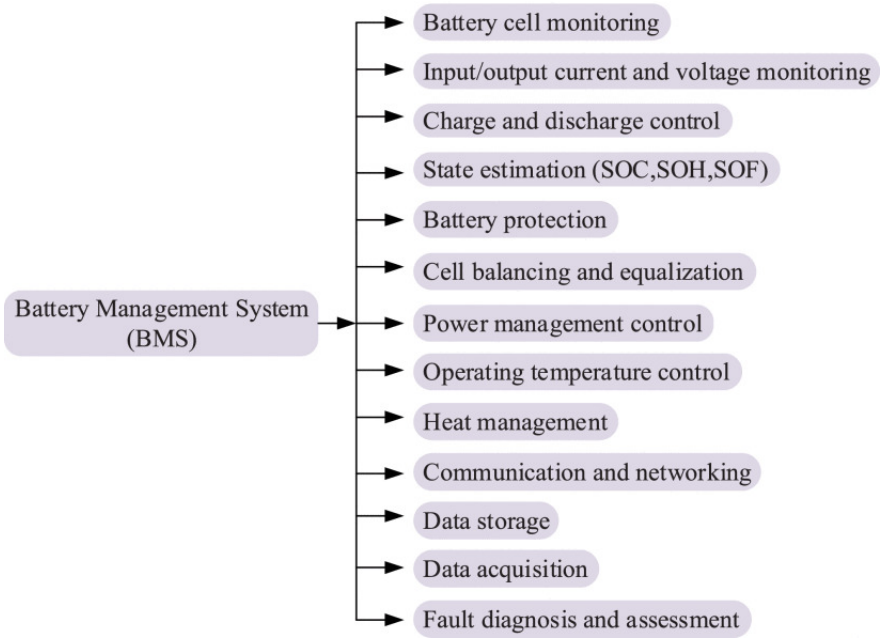

Fig. 2.7.1: BMS responsibilities [171]

Voltage sensing is of particular importance as the state of health (SOH) and state of charge (SOC) estimations directly correspond to the voltage measurements of the battery. Dangerous charging is also measurable from the voltage applied across

the cells. Examples of these dangerous voltage scenarios are overcharging or over-discharging [172].To measure the voltage levels, modules typically contain integrated circuits or "chipsets," included in the module structure [173].

The BMS is responsible for the various current loads and temperature management protocols. To communicate the proper information to the battery load control computer or the thermal management system, current and temperature sensors are placed into each modular structure [169]. The temperature sensor communicates the overall modular temperature to the BMS. The BMS would measure the internal temperature of the battery if possible, as a battery's internal temperature is of critical importance to know if the battery cell is an area of safe operation [174, 172]. However, to measure the internal temperature of the cell, the structure of the cell would necessarily need to be punctured or penetrated; this is not ideal for several reasons. Firstly, puncturing the cell would cause irreversible damage and could potentially release toxic chemicals. Secondly, as several hundreds of cells can depend on the cell topology in an automotive-style battery pack for EVs, the cost of each cell would unnecessarily increase. For these reasons, temperature sensors are typically placed at the module level, and the cell temperatures generally are interpolated between these sensors.

The overall structure of the BMS system can technically vary, being either a centralized network, a modularized network, or a decentralized network [20]. The communication between the cell and the BMS system is realized across all categorizations. This can be seen in Fig. 2.7.2.

These are the critical functions of a BMS and are necessary for the smooth operation of an EV. Data acquisition is of general importance to the BMS to carry out the other important purposes of the BMS function. Without its ability to gather information, none of the following essential functions could be carried out effectively.

Safety protection: The BMS is responsible for the limitation of the overall power usage of the battery to protect the safety of the passengers and the batteries themselves. Limiting the current and voltage drawn from the battery can enhance the overall life cycle of the storage mediums. These power level bounds are typically

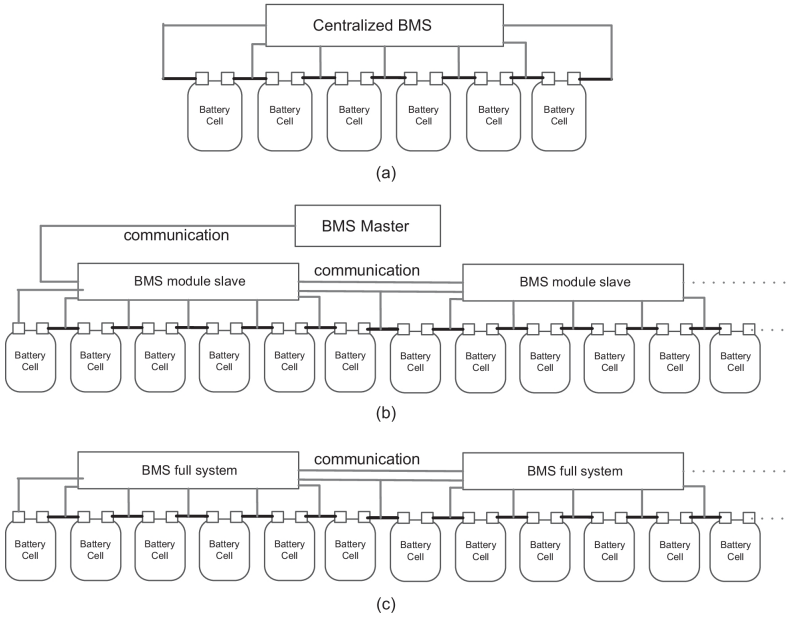

Fig. 2.7.2: Topology of BMS systems [20]

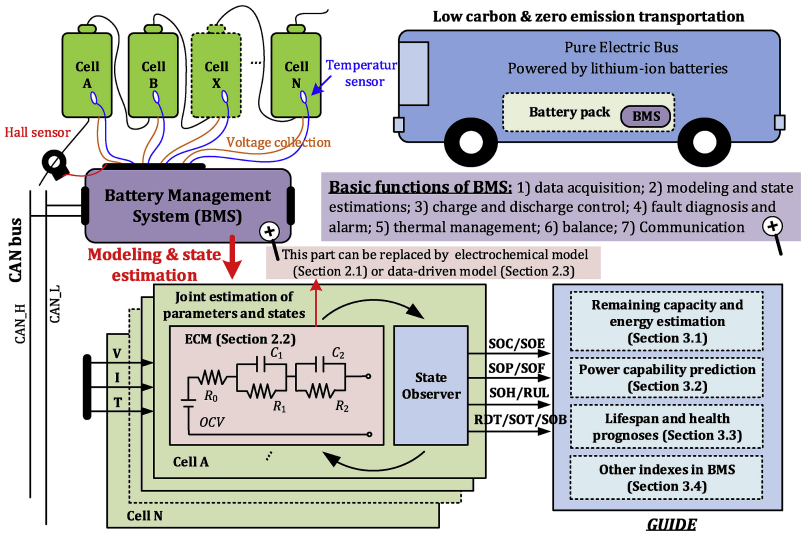

Fig. 2.7.3: Functional structure diagram of an advanced battery management system [175]

calculated separately.

Predicting the battery's state is essentially separated into two categories: estimating the battery's overall SOC and SOH.

2.7.1 Thermal Management of Batteries

Thermal management of batteries is of the utmost importance due to lithium plating, battery degradation, thermal runaway, etc. To avoid these unwanted behaviors, temperature management of the battery is critical. This can be done in several ways; power management from the battery, that is, current and voltage limits applied at the battery at specific load cases, which would be completed at the BMS level (refer to 2.7). Or it can be achieved by using cooling or heating from some dedicated cooling/heating system. In reality, both are used to minimize damage to the battery and maximize the vehicle's performance concerning safety parameters and the vehicle's design limits.

Overall, there are three different types of thermal management systems for battery electric vehicles [176].

1. Air cooling
2. Liquid cooling
3. Phase change material (PCM) cooling

2.7.1.1 Air Cooling

Air cooling can be divided into two further sections, either passive cooling or active air cooling [177]. Air cooling has significant expense advantages compared to liquid cooling or PCM cooling. Passive cooling is the technique of only using the difference between the ambient air temperature and the battery to cool the battery without preconditioning the air. Active air cooling, on the other hand, takes ambient air with preconditioning to cool the battery [178]. Both configurations take advantage of forced convection to dissipate heat. This is extremely simple and affordable due to the lack of

complexity and moving parts, but its performance is limited to the extensive loading of the batteries. These systems were used effectively in the early HEV, PHEV, and BEV models, such as the 2001 Toyota Prius and Honda Insight. In general, passive and active air cooling have less expensive components and simpler designs than liquid and PCM cooling. Due to this, they also have low maintenance and installation costs and compatibility with different batteries without fluid leaking issues. The critical downside for air cooling, in general, is air cooling's overall effectiveness for heating and cooling the battery pack due to the low air heat capacity and thermal conductivity [179, 180, 181, 182].

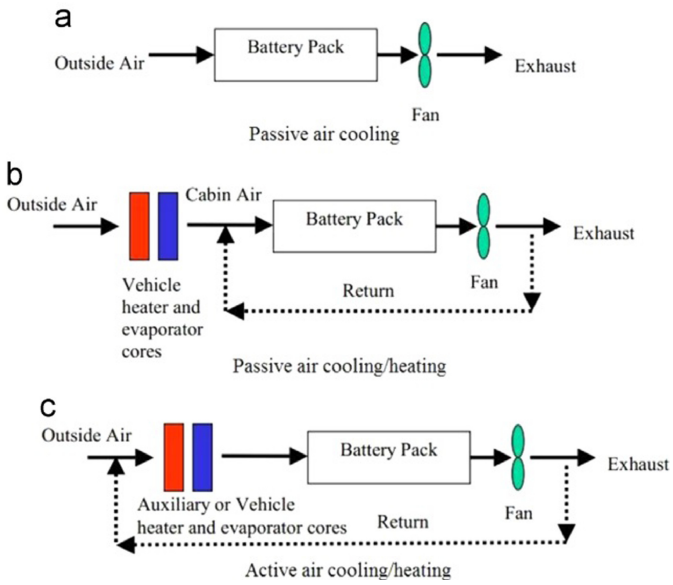

Fig. 2.7.4: Passive vs active air cooling [62]

More recently, the configurations of air-cooled batteries are being improved by changing the battery positioning [183], flow-pattern [184, 185], and change in inlet and outlet positions [186].

2.7.1.2 Liquid Cooling

Liquid cooling for battery packs has been shown to be highly effective compared to the air cooling technique. Depending on the configuration, it can be up to 3500 times more effective [187]. Liquid cooling management techniques can be subdivided into direct or indirect cooling [177, 176]. The difference is that for direct cooling,

the modules or batteries come directly into contact with the heat transfer fluid. In contrast, for indirect cooling, there is indirect contact with the heat transfer fluid, such as the cooling plate/jacket [178]. Both direct and indirect liquid cooling techniques are highly effective and can reduce temperatures and temperature gradients within the batteries. At the cost of this increase in effectiveness, their complexity and costs associated with their constructions are also higher [188].

An example of an indirect liquid cooling configuration constituted of pouch cells is discussed and evaluated in [189]. This example is shown below Fig. 2.7.5.

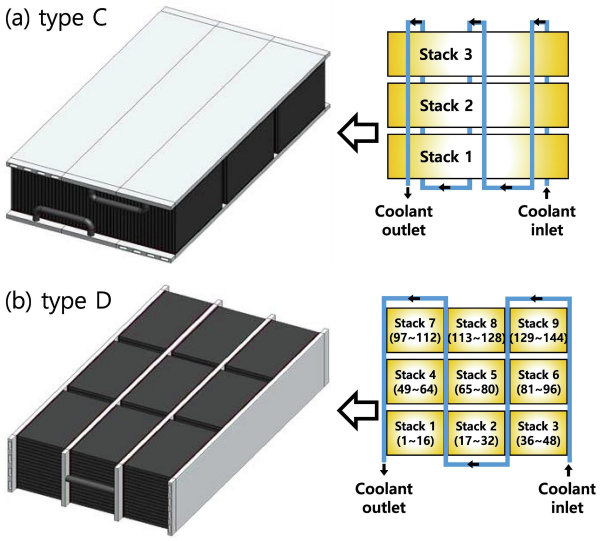

Fig. 2.7.5: Pouch cell battery pack with liquid cooling [189]

2.7.1.3 Phase Change Materials

Phase change materials use the latent heat of a phase change to remove heat from the battery pack. As a result of this cooling principle, PCMs are a type of passive cooling method [176], which reduces the necessary parasitic power. The benefit of using this type of system over the previously stated systems is the capacity of the cooling system to achieve a homogenous temperature distribution [190]. Also, they have smaller volumes in comparison with both liquid and air cooling methods [179, 180]. Paraffin is commonly used due to its high latent heat and other important chemical characteristics such as low corrosivity and toxicity [191]. However, the downsides

typically with these types of systems are their heat conductivity, leakage risks, and risk of supercooling [179, 180], and when compared with air cooling, has an increased initial cost. New research is trying to alleviate some of these issues. As an example, Murali et al. [190] discuss adding high thermal conductive particles into PCM to increase thermal conductivity.

2.8 Thermal Runaway

With excess heat generation and, consequently, excess temperatures within the battery pack, a process known as thermal runaway can be triggered. This process is a chain of exothermic reactions within the battery [192]. This exothermic reaction can lead to the battery catching fire, releasing dangerous fumes, and, in extreme circumstances, even explosions [193]. This is an unwanted phenomenon for multiple reasons: danger to human life, destruction of property, and expensive cleanup.

Many different avenues of battery mistreatment can cause this process, [194, 193] defines them into three categories;

- mechanical - physical mistreatment of batteries, e.g., penetration, external stress, etc.
- thermal - battery temperatures growing too large due to heat generation
- electrical - overcharge, over-discharging, etc.

Some examples of the consequences of these abuses can be seen in Fig. 2.8.1, and correspondingly show the obviousness of how unwanted this phenomenon is.

The first abuse type naturally isn't easily controlled for in the design phase. However, design and modeling steps can help reduce the last two abuse types.

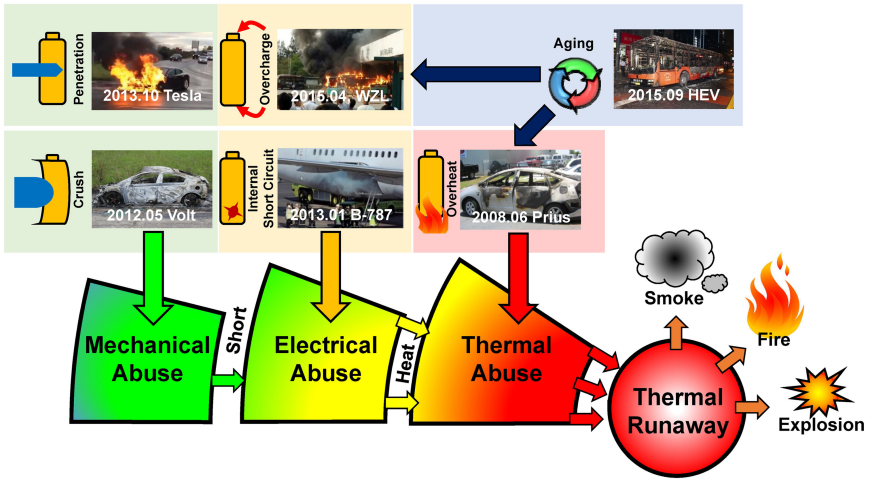

Fig. 2.8.1: Thermal runaway [193]

2.9 Battery State of Health and Degradation Mechanisms

Estimating the SOH can be difficult as the parameters are often "pseudo-static." That is, they are very slowly changing characteristics. As the cell charges and discharges, the overall capacity fade of the battery is caused by two major degradation contribution types [195]; the degradation types are structural deterioration and side reactions. Structural deterioration is the deformation due to diffusion-induced stress during battery charging and discharging. In contrast, side reactions refer to the degradation occurring due to the instability of the electrolyte or reactions taking place outside of the solid electronic material. The SOH properties affected by these degradations are challenging to measure directly and usually must be measured indirectly with a corresponding algorithm applied to estimate its SOH.

2.9.1 Anode Aging Mechanisms

The graphite anode under voltage operates at voltages outside of the stable voltage window. As such, when the electrolyte comes into contact with the anodic material within these unstable windows, it forms a solid electrolyte interface (SEI). This SEI layer acts as a barrier between the anode and the electrolyte, increasing the impedance

of the battery and remaining for the duration of the battery's life. Despite this increased impedance at the battery's life cycle start, this SEI formation is critical for the battery's operation. The SEI protects the rest of the graphitic material as it does not react with the electrolyte in the usable voltage range [196, 197]. There are two crucial points to note about the formation of this SEI layer: Firstly, the SEI layer consumes lithium in the formation process and reduces the cell's overall capacity. Secondly, even though the SEI is porous, the SEI layer increases cell resistance. The formation of the SEI is a complex non-uniform process [169].

Keeping the concepts mentioned earlier in mind, it then becomes clear that any damage to the SEI layer exposes fresh unprotected graphite material to the electrolyte, which will then grow more SEI once again, compounding and reducing the overall lithium in the battery, and increasing the battery's resistance. Therefore, any process that breaks down or degrades the SEI layer thus degrades the entire battery's performance. An example of such a process is when water is trapped within the battery. It reacts with the LiF_6 salt to create hydrofluoric acid [118]. This acid deteriorates the SEI layer, removing more cyclable lithium and thus deteriorating the battery.

Another anode deteriorating process is anode poisoning. Anode poisoning is the effect that occurs when the cathodic material breaks down into the electrolyte. Due to diffusion processes, these dissolved materials can intercalate into the SEI layer. These elements are non-reactive and, as such, block the intercalation of lithium into the anode, increasing the resistance of the battery. These processes can be seen in 2.9.1.

As the lithium intercalates and deintercalates into the material, the material expands and contracts volumetrically. This leads to stresses within the particles that can cause cracks not only in the SEI layer but also in the bulk of the material. In the anode material, it is also possible at high currents that there is solvent co-intercalation [199], which is the behavior of electrolyte solvent intercalating into the material in conjunction with lithium. As the solvent has extra volume, this can further expand the particle, creating cracks or fissures in the anode [169]. These fissures then come

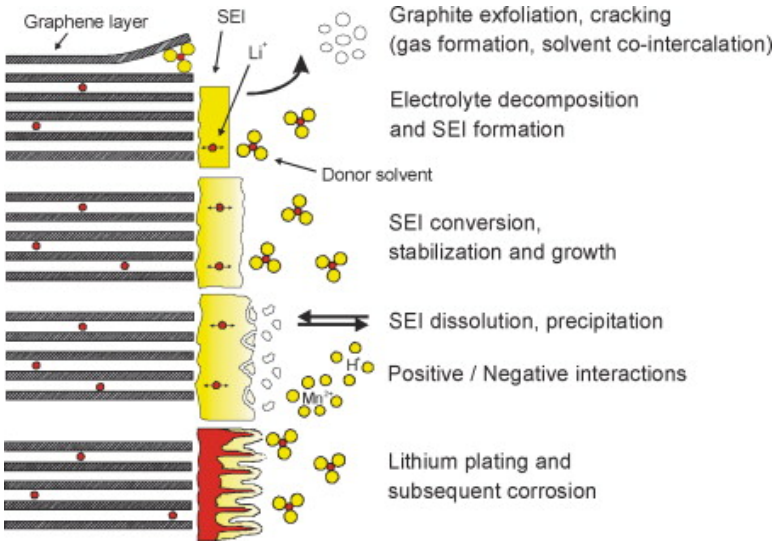

Fig. 2.9.1: Aging mechanisms of Li-ion batteries [198]

into contact with the electrolyte, reducing the overall capacity and creating thicker SEI sections. These can also cause stress within the binders and correspond to the mechanical connection between the particles and the current collector. Once the particles flake off due to cracking and no longer have a solid contact pathway to the current collector, fewer pathways for the electron to charge and discharge are present. This reduction in pathways increases overall cell resistance/impedance and can effectively reduce the battery's capacity.

If the cell is over-discharged, the copper current collector enters a region of low voltages where it can dissolve into the electrolyte [137, 200]. This process is called current collector dissolution. If this occurs, the corrosive material can deposit in the particles, increasing the resistance of the battery.

The last degradation mechanism that is well-known within the industry is lithium plating. Lithium plating occurs when the potential of the solid electrolyte drops below 0 V. This can occur when there are cold temperatures and when there are high current rates [201, 202]

2.9.2 Cathode Aging Mechanisms

Electrolyte oxidation and $LiPF6$ decomposition form a surface layer similar to that on the SEI on the anode. However, cathodic SEI differs from the anode's in magnitude and importance. Its magnitude is much smaller than its anode counterpart's and is usually not considered as significant as in the anodic section [169].

Metals within the electrode can dissolve into the electrolyte and then re-precipitate into the particle. This causes the internal structure of the cathode to break down, leading to a capacity loss. This process is also the reason for the aforementioned anode poisoning and is most dramatic for cathodic materials containing manganese or cobalt. This behavior is most consequential when the battery is at high temperatures and with low and high states of charge [169].

Once again, when the lithium ions intercalate and de-intercalate into the cathode, there are volume changes in the cathodic material. This process seemingly sounds similar to the anodic material swelling processes but is fundamentally different. These volume changes are due to phase transitions within the material's structure or, put more plainly, the structural shape of the crystal structural shape of the material. These phase transitions, if not large in magnitude, are primarily reversible, but if they proceed beyond a certain threshold, they are entirely irreversible. This phase transition collapses the layered structure, leading to capacity loss.

Like anode material, the cathode also experiences capacity loss and increased impedance due to lost contact with the current collector. The reason is the same as the anodic material; as the stresses build up within the material over time, particle and binder materials can break down, reducing the overall contact with the current collector.

The cathodic processes are enhanced or increased due to high and low SOC and high current rates. This means that effectively reducing the current rate is essential to reduce the overall aging of the cell.

One can also see that many of these degradation behaviors are responsive to temperature, again showing the importance of temperature control and prediction

within the Li-ion battery systems.

2.10 Cell Balancing Techniques

Cell balancing is redistributing the charge of the different cells and modules to have a uniform SOC across the entire battery pack. This is important for many Li-ion batteries as the voltage across the various cells changes with SOC, and the amount of energy that can be retrieved from each cell differs. This effectively reduces the capacity of the pack [203]. These differences are caused by the differences in the cells from manufacturing [204]. For instance, the circuit diagram Fig. 2.10.1 shown below, where a simple SCM module with four batteries is loaded with some non-zero defined current labeled i_{load}.

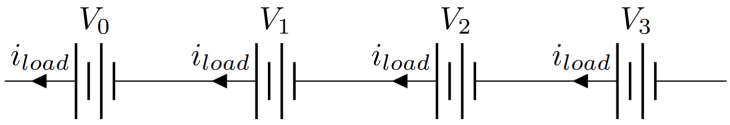

Fig. 2.10.1: Batteries in series

As can be seen, when the cells are in series, the load across all of the batteries remains the same; if the cells do not have uniform SOCs, which is likely the case if there are manufacturing differences, the entire system essentially has the SOC of the battery with the least capacity remaining. This reduces the battery of the whole battery pack. As discussed, the batteries' aging processes are accelerated at high/low SOC states. Therefore, if the system was run at low SOCs for specific unhealthy cells, the aging is accelerated for the weakest cells.

The diverging in cell SOCs is due to several processes; firstly, when battery capacities are different, which is almost always the case due to manufacturing differences, and aging affects each battery cell differently. As the pack is discharged, the overall SOC diverges naturally due to these discrepancies. This process can be visualized in Fig. 2.10.2.

Secondly, the cell SOCs diverge over time due to the difference in the charging efficiencies or the coulombic efficiency of the battery. If the charging efficiencies of

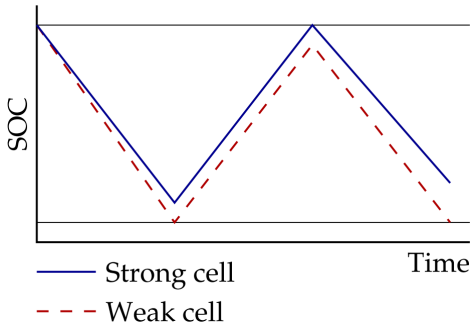

Fig. 2.10.2: Battery pack imbalance due to capacity differences [84]

the batteries are different, as the batteries are continuously charged and discharged, the divergence grows, and the cells become unbalanced.

Unbalanced cells are an unwanted phenomenon, and as such, they need to be rebalanced after a predetermined amount of time. By completing cell balancing, the battery life can be extended [205]. This can be achieved in two ways [206];

1. Passive balancing
2. Active Balancing

Passive balancing is balancing the modules and cells by dissipating excess charge through heat dissipation [207]. Historically, the balancing techniques in the first category used passive electrical elements [84]. It is noted that this is no longer the case, as more active components are used currently. Nevertheless, this naming scheme will be kept here to stay in line with the standard convention. Passive balancing typically uses dissipative techniques to reduce the excess charge from stronger cells to re-balance the battery pack. These methods are simple to implement and typically of lower cost [208]. Looking at the circuit diagram for this system, Fig. 2.10.3 shows that the shunt resistors are placed in parallel with the batteries. As differences in potential build between the cells in series, the shunts re-balance the system.

Active balancing, however, redistributes charge from healthy to unhealthy cells. These methodologies are more complex and costly [207] and are typically not used currently in the field [208]. These techniques are being researched and are believed to become part of the growing repository of tools that will emerge in the EV battery

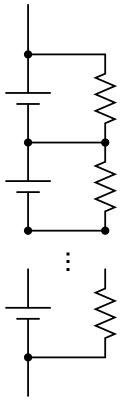

Fig. 2.10.3: Fixed shunt resistor [84]

management field.

2.11 Battery Modelling

Modeling the battery and its heat generation is the first step in understanding the behavior of the battery and how to optimize the battery's performance. Whether that is through range extension, life extension, or an improvement in drive capabilities, the models for batteries in this thesis are generally categorized into several categories.

- Analytical Models
- Electrical Models
- Electrochemical models

Each method has its benefits and downsides and will briefly be discussed to motivate the modeling methodology.

2.11.1 Analytical Battery Modelling

Analytical modeling can be broken down into several sub-categories, such as stochastic and non-stochastic modeling [209], but a generalized approach will be explained here for easier comprehension. Analytical modeling breaks the problem into a higher

level of abstraction, removing itself from the physical representation and using experimental data to fit parameters to adjust the model's performance. For example, the kinetic battery model postulated originally by Manwell et al. reduces the complexity of the battery into a system of "wells," each filled with a certain amount of electrons that supply the current necessary for functioning. Figure 2.11.1 shows the representation of the model.

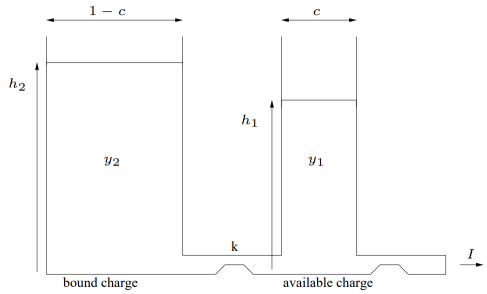

Fig. 2.11.1: Kinetic battery model representation [209]

The model is broken into two sections; one "well" is the "bound" energy, which represents the energy immediately unavailable in the battery, while the "available" energy well is immediately able to discharge into the current. The "well" for the available energy is filled with a fraction of the total charge c, while the "unavailable well" is $1 - c$. Using experimental data, a conductance term k is used to develop equations with relation to the height between the wells represented by equations 2.12,2.13 and 2.14.

$$h_1 = \frac{y_1}{c} h_2 = \frac{y_2}{1-c} \tag{2.12}$$

$$\frac{dy_1}{dt} = -i(t) + k(h_2 - h_1) \tag{2.13}$$

$$\frac{dy_2}{dt} = -(h_2 - h_1) \tag{2.14}$$

The solution can be found using the appropriate Laplace transforms, and when fitted with the appropriate SOC data, it can accurately describe a constant discharge process [210]. Despite its accuracy for continuous discharge, this method cannot

accurately predict variable discharge processes.

2.11.1.1 Neural Network Modelling

Neural networks (NN) or artificial neural networks (ANN) have gained much traction in the mainstream media and the research community. When appropriately applied, NNs can be highly robust, fast, and provide accurate results.

The basic structure of neural networks is provided here. Still, as no NN was used within the thesis, their specifics will only be delivered to show the context of the research happening within the field and the relative advantages and disadvantages compared to the chosen thesis methodology.

NNs historically are called that due to the algorithms' original representation to describe the behavior of neurons that work within the brain. That is to say that for a neuron, when a specific stimulus is input, the neuron fires or "activates." In this way, the classical representation of neural networks tries to imitate this behavior with functions, so the process activates when a specific condition is met. These "neurons" or activation functions are then connected to the other activation functions analogously as the neurons in the brain. This representation can be seen in Fig. 2.11.2.

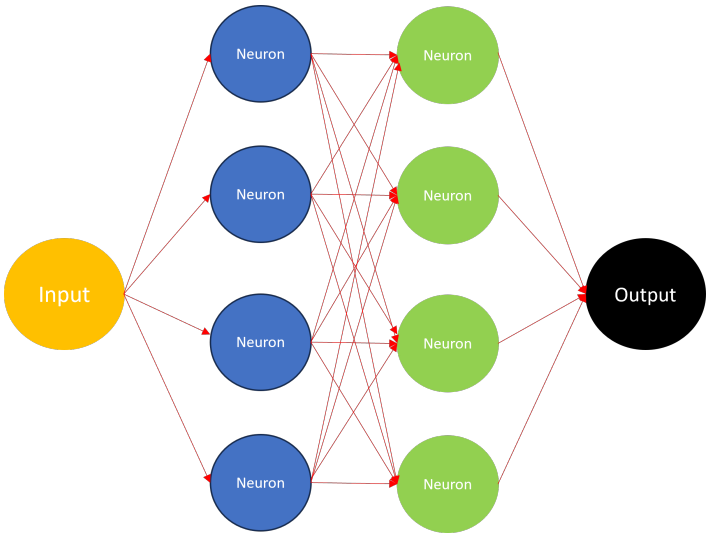

Fig. 2.11.2: Diagram of a neural network [211]

A chosen activation function represents each neuron. Notwithstanding that the

subsequent list is certainly not extensive nor representative of all activation functions, some of the most common activation functions are [212],[213].

1. Sigmoid
2. Tanh
3. ReLU
4. Leaky ReLU

A NN's prediction accuracy depends on the number of layers used in the algorithm and the activation function [212],[213]. As mentioned earlier, each function provides different advantages and disadvantages. For the listed equations above, a brief table is displayed in table 2.11.1.

Table 2.11.1: Pros and cons for different activation functions

Activation function	Pros	Cons
Sigmoid [214]	reduces input range between 0,1 Easy interpretation	Output non-zero centered Kills gradient
tanh [215]	Zero-centered	Kills gradient
ReLU [216]	Computationally efficient Converges quickly	Not zero-centered
Leaky ReLU [217] [216]	Computationally efficient Not saturated in the pos region	Not zero-centered

NNs are then trained on a subset of data with known output. Using this known output, a comparison can be made with the estimated neural network output. The differences between the expected and subset value outputs are then compared, and the goal of the network is to minimize this error as given in equation 2.15.

$$Error = min(fn(y_{estimated}, y_{subset})) \tag{2.15}$$

2.11.2 Electrical Battery Modelling

Equivalent circuit modeling (ECM) techniques represent the battery and the system as a series of *representative* electrical components. Using analysis from experimental data, accurate results for both constant and non-constant discharge profiles can be achieved.

Further detail will be provided here as some of the concepts necessary within the following explanation transfer well to that of the electrochemical modeling section.

As a reminder from section 2.2, a finite voltage difference across a battery's terminals between only its anode and its cathode is known as its *open circuit voltage* (OCV). Figure 2.11.3 displays an equivalent circuit representing the OCV of the battery.

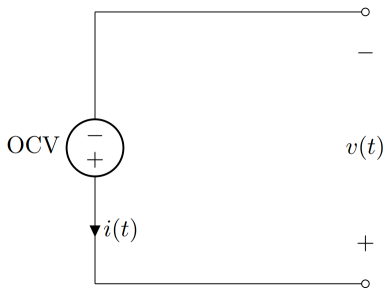

Fig. 2.11.3: ECM representing the OCV of a battery

The battery's state of charge (SOC) represents the percentage of total charge nominally available in the battery. By adding further electrical components to the representative circuit, accuracy can be added to the model. For instance, the internal resistance of the battery that must be overcome can be defined as R_0, and the circuit from Fig. 2.11.3 becomes the circuit seen in Fig. 2.11.4 [218].

For calculation of the SOC, the coulomb counting formula seen in equation 2.16 such that Q represents the battery's total capacity, and i represents the current can be used for the continuous-time domain.

$$SOC(t) = SOC(t_0) - \frac{1}{Q}\int_{t_0}^{t} i(t)dt \tag{2.16}$$

Most EV systems use the discretized time domain due to the sampling nature of

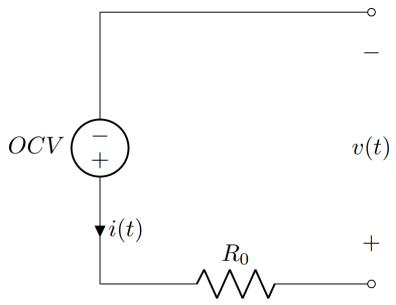

Fig. 2.11.4: ECM diagram with internal resistance

the sensors. For a discrete-time domain, equation 2.16 can be rewritten as equation 2.17, where k is the time step of interest.

$$SOC(k+1) = SOC(k) - \frac{\Delta t}{Q} i(k) \tag{2.17}$$

Combining equation 2.17 with the defining electrical equation for the circuit in 2.11.4, the voltage response represented by the ECM can be written as equation 2.18, where $v[k]$ represents the voltage in the discrete-time domain at time step k.

$$v[k] = OCV(SOC[k]) - i[k]R_0 \tag{2.18}$$

This equation here is often sufficient for cells but not for battery packs, as at the cellular level, resistance is constant but non-constant at the pack level.*Polarization* or the difference between the OCV and the terminal voltage in the battery is non-linear. To include these polarization effects, further electrical components may be included within the circuit to better represent the system's behavior. An ECM with the polarization effects included based on a parallel capacitance representation is shown in Fig. 2.11.5.

This leads to a more representative equation after some algebraic manipulation, resulting in equations 2.19 and 2.20. Equations 2.19 and 2.20 represent the battery's current and voltage response, respectively.

$$i_{R_1}[k+1] = e^{-\frac{\Delta t}{R_1 C_1}} i_{R_1}[k] + (1 - e^{-\frac{\Delta t}{R_1 C_1}}) \tag{2.19}$$

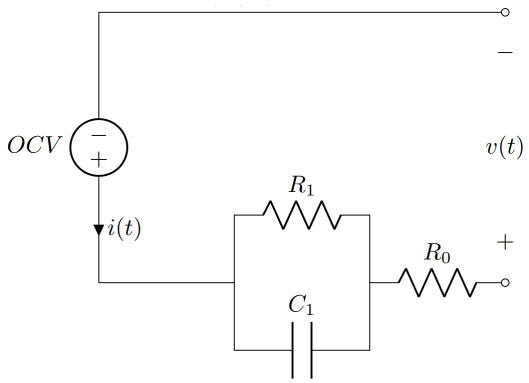

Fig. 2.11.5: ECM with polarization effect

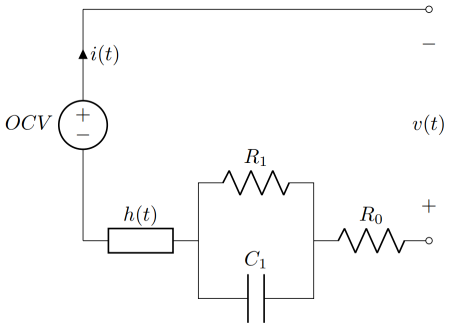

Fig. 2.11.6: ECM with polarization and hysteresis effects

$$v[k] = OCV(SOC[k]) - R_1 i_{R_1}[k] - R_0 ik \tag{2.20}$$

Within the cell, there are notable hysteresis effects such that the measured OCV at a particular time depends on the history of the battery. For example, if the cell is charged to 50% SOC and left to rest, the OCV will be slightly higher than anticipated, but if the cell is discharged to 50%, then the OCV will be somewhat less than OCV. This means that the potential SOC can have an extensive range for any measured voltage. A generic voltage additive term can include this effect within the circuit, as seen in Fig. 2.11.6.

This hysteresis term can be mathematically represented by equation 2.21

$$h[k+1] = h_0[k] + h_m[k] \tag{2.21}$$

Where h_0 is an instantaneous hysteresis voltage, and h_m is a hysteresis voltage

based on the SOC state.

ECMs are powerful, and there are many upsides to modeling the batteries as such. However, there are several downsides to the modeling techniques. For any specific battery, data is necessary to fit the curves accurately across a broad domain of temperature ranges. The results still have varying inaccuracies depending on the number of electrical resistances and capacitances chosen. There are fewer options for future work regarding the physical transformations of the battery as ECMs do not represent the internal states of the battery.

2.11.3 Electrochemical Battery Modelling

This final technique is arguably the most immediately computationally expensive. Typically, these models start from the first principles of chemical interactions and usually consist of partial differential equations (PDEs) to estimate the various states of charges and currents within the battery. Voltage and current characteristics of the battery are usually identified from these PDEs. It is common to reduce some of the computational expenses for electrochemical modeling by reducing the overall model to a 1D model by simplifying some of the behaviors of the battery.

The most common 1D electrochemical model is the Pseudo2D (P2D) porous Newmann model. This model was proposed in 1993 by Newman [219], and in it, the underlying assumption is that the various micro-scale reactions can be modeled using volume-averaging techniques. The inner complexities of the battery are then simplified, and the materials in both the anode and cathode sides of the battery are modeled as a homogeneous material matrix. The solid matrix is the solid material of the respective anodic or cathodic material of the battery, and the spaces of the matrix are filled homogeneously with electrolyte. In this way, many of the internal chemical behaviors of the battery can still be modeled well [220, 221]. An even further simplification of this model, known as the single particle model (SPM), can be made with successful estimation characteristics [222]. A schematic of the P2D and SPM is represented in Fig. 2.11.7. The SPM reduces the computational cost heavily [223] at the expense of fine-tuning according to the electrolyte properties and high discharge

rates [224].

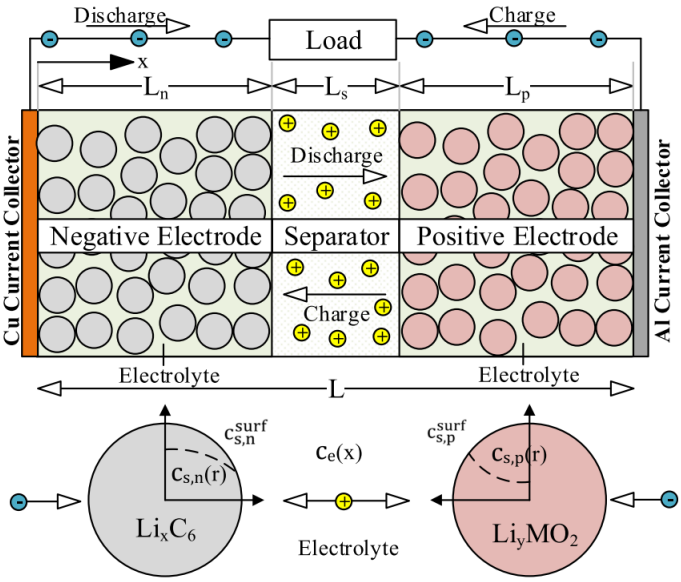

Fig. 2.11.7: P2D model (top) and SPM model (bottom) representational diagrams [222]

Perex et al. [225] used an SPM model with a Legendre-Gauss-Radua pseudo-spectral method to mathematically formulate an optimal charging profile to reduce charging times while staying within its electrochemical constraints.

To increase model accuracy, Li et al. [226] developed an SPM incorporating stress-enhanced diffusion and electrolyte distribution. When comparing the P2D model to the SPM on the same battery under a 1C discharge rate, the calculation time was reduced by 68 % while keeping the relevant fidelity in molar concentration in the electrolyte.

Baba et al. [227] developed an enhanced SPM (ESP) and coupled its simulation with a 3D unrolled plane of spirally wound electrodes for an 18650 Li-ion battery and found that this process could estimate the temperature behavior.

Tanim et al. [228] used an enhanced SPM as the basis for a Luenberger SOC observer to compare isothermal and non-isothermal SOC estimations in a lithium battery and found that at low and high temperatures, it reduces the root mean square error considerably as the isothermal voltage response significantly overshoots in these domains away from the 25 °C set point.

CHAPTER 3

Methodology

This chapter explains the methods used in the research to estimate the battery's thermal response. Firstly, the explanation of the genetic algorithm is completed. Subsequently, the mathematical background for developing the 1D SPM is discussed. The development of the heat generation model is explained, and the 3D modeling of the battery cell and module is explored along with some underlying assumptions.

3.1 Genetic Algorithm

Many different parameter estimation techniques exist for highly nonlinear systems: nonlinear least regression, Kalman filters, and neural networks. These techniques have advantages and disadvantages, but one technique, known as the genetic algorithm (GA), is well-defined within the given constraints of the problem. The GA technique is a recognized method for solving highly complex problems where the system's inputs are not necessarily known, for example, the notorious traveling salesperson problem. This problem defines a "traveling salesman" who is traveling between pairs of cities, and the problem definition is the shortest possible route that visits each city exactly once and returns to the original starting location. Alternatively, the famous knapsack problem is where an assortment of likely items, each with a value and weight, is added to maximize the overall value of items in the backpack but also must weigh less than a specific weight constraint. This problem as can be seen scales by n, where n is the number of inputs, and is known as an NP problem. To try all of the possibilities would be computationally infeasible, so the GA is typically employed for the previous

two examples. Under this reasoning, the GA is also considered an excellent tool to estimate the various inputs into this highly complex nonlinear problem.

The GA is an algorithm that generates different solutions, each with its input parameters or "genes," and over time, after selecting the best results, generates more solutions based on the best prior results. In this way, there is an analogous comparison with how genetic adaptation occurs in nature, where the "best" solution survives and "passes" its parameters onto the next generation of solutions. It should be noted that although the GA can be effective, to say it finds an optimal solution is mistaken, as it can only find local optimums. It is not guaranteed to find a global optimum.

The explanation of the GA methodology [229] breaks the GA into several steps;

1. Generation of a random population
2. Evaluation of solutions' "fitness."
3. Selection of best results
4. Crossover of parameter data
5. Mutation of parameter Data

The explanation will be broken down in the same manner to be clear and concise.

Steps 2-5 are repeated until a condition is met; either a minimum is found, or the value drops below some user threshold that is decided a priori to be sufficient, such as computation time, or number of generations.

3.1.1 GA Population Initialization-Random Distribution

This step is relatively straightforward; the user defines the maximum ranges to generate each gene pool and the defined number of solutions. To keep with convention, each unique collection of parameters with its combination of input parameters will be labeled as an "individual." Each input parameter is defined as a gene. For the initialization step, each individual is generated randomly by randomly selecting each gene value within the gene limit ranges.

3.1.2 GA-Fitness Evaluation

The solution's fitness is its outcome used to evaluate the superiority of one individual over another; for example, take the famous knapsack problem previously defined; its outcome or *fitness* is the overall value of the combination of items in the knapsack. This evaluation step, like its namesake, evaluates the individual's overall fitness in the case of estimating the parameters of the 1D model. The HPPC voltage curves of the batteries are compared to the simulated 1D electrochemical model's voltage estimation. The root mean squared error (RMSE) estimated between the simulated and experimental voltage curves is then used as the individual's overall fitness. In this way, the GA is made to find the minimum RMSE value.

3.1.3 GA-Solution Selection Methods

To minimize the RMSE, selection criteria are necessary to choose which individual characteristics should be kept for the next generation of solutions. A concept that is often discussed in complex search algorithms is "exploitation vs. exploration," that is to say, how well does a specific algorithm capitalize on the information that is being currently learned in comparison with how "willing" the algorithm is going to explore based on sub-optimal information. It is often cited that a relative trade-off is necessary for an algorithm to be effective. With this concept in mind, several methods are used for this selection criteria;

1. Tournament selection
2. Proportional selection
3. Stochastic universal sampling selection
4. Rank selection
5. Elite selection

Tournament selection takes small randomized subsets of the groups and compares the fitnesses between them. The best individual in the small subset tournament is

then selected to be passed on to the next generation. By selecting individuals in this fashion, the best individuals will likely be chosen, with some individuals having less "optimal" fitnesses. This selection method has a balance between best exploitation and exploration but does have one specific downside. There is a non-zero probability that the best solutions are not chosen.

Proportional selection is a method in which the fitnesses are realized as a proportion, and based on this probability, the solutions have that probability of being chosen. The equations for a straightforward proportional selection are seen in equation 3.1 and equation 3.2. Equation 3.1 shows the calculation for the total generational fitness. The variables represented as Z_{tot}, Z_{ind}, and n are the cumulative fitness sum, the fitness of the individual, and the number of individuals in the generation respectively. Equation 3.2 is the calculation for the probability the individual will be chosen, which is represented as ϱ_{ind}

$$\sum_{ind=1}^{ind=n} Z_{ind} = Z_{tot} \tag{3.1}$$

$$\varrho_{ind} = \frac{Z_{ind}}{Z_{tot}} \tag{3.2}$$

This selection method also has a good balance between exploration and exploitation. Still, it has the same issues as the tournament selection method; the best individual has some non-zero probability that it will not be chosen.

The stochastic universal sampling method divides the sub-sample of the fitnesses into n equal samples. This method reduces bias towards the best performances but still has the same issues as the previous methods.

The rank selection method divides the probability of the individual being chosen based on the sorted rank of the fitnesses. This ranking scheme is seen in equation 3.3, where X_{ind} represents the individual's rank within the generation, and X_{tot} represents the total sum of all the ranks.

$$\sum_{ind=1}^{ind=n} X_{ind} = X_{tot} \tag{3.3}$$

and using equation 3.3 calculating the probability of the chosen individual based on equation 3.4.

$$\varrho_{ind} = \frac{X_{ind}}{X_{total}} \tag{3.4}$$

This method slightly reduces the difference between the top and bottom-performing individuals to favor exploration.

Elite selection is the method used in combination with any of the methods mentioned above but guarantees that a predefined amount of the best individuals are chosen.

3.1.4 GA-Solution Crossover Methods

The crossover process is the act of genetic parameter information sharing. As the GA is used in many search algorithm problems, such as the knapsack problem, many crossover methods do not apply to this thesis problem. The processes that do not follow the estimation parameters of the 1D SPM model are labeled with a (N/A) next to their classification.

1. One-point crossover (N/A)
2. N-point crossover (N/A)
3. Uniform Crossover (N/A)
4. Order Crossover (N/A)
5. Blend Crossover
6. Fitness Crossover

The last two methods are the only ones of interest for the context of the thesis. Blend crossover takes the two genes from the two "parent" individuals and, with some

α, linearly finds a point between the parents' genes. This process is graphically represented in Fig. 3.1.1 where the green dots represent two points on an axis representing a gene value. The vertical bars in Fig. 3.1.1 represent the previous gene values. As can be seen from changing the value of *alpha* the points of the next generation's genes fall in between the previous generation's gene values.

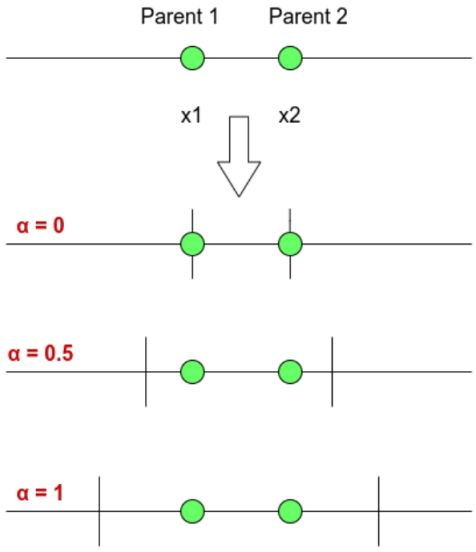

Fig. 3.1.1: Linear crossover example taken from [229]

The fitness crossover compares the current and the next generations and only keeps the best. One issue with fitness crossover is that it reduces exploration and is computationally more expensive as the previous and current generations' information needs to be stored.

3.1.5 GA-Solution Mutation Methods

Mutation is the process of altering genes based on some predefined probability. The mutation is a step that encourages new exploration. This step is extremely important, and although exploration is a beneficial outcome of the GA, if the mutation probability is too high, progress from generation to generation can be lost in finding the optimum. Once again, there are many kinds of predefined mutations in GAs due to the comprehensive nature of applicable problems. Similarly to the previous list, the mutation types irrelevant to this research are listed with a subsequent "N/A."

1. Random deviation mutation
2. Exchange mutation (N/A)
3. shift mutation (N/A)
4. Bit flip mutation (N/A)

Random deviation mutation applies a random shift in an individual's genes based on some non-zero probability. This shift then adds some exploration, even for individuals considered highly fit.

3.1.6 GA-Parameter Tuning

Parameter tuning is used based on averaging information from previous generations to take advantage of both exploration and exploitation. If the overall average remains stagnant or the performance of the whole population in general starts to degrade, there is a combination of a/an;

- Population increase
- Increase in crossover probability
- Increase mutation probability

3.2 1D Electrochemical Model-The SPM model

In this section, the discussion of the electrochemical model is completed for a full understanding/replicability of the research conducted. The governing equations and rationale behind the 1D model are explained and detailed. Also, the discrete-time realization algorithm (DRA) is explored to calculate the system's response. The equations and notations here are used in [230, 84] and are kept the same for easier understanding if further inquiry into the source of the methodology is necessary.

3.2.1 SPM Fundamental Equations

The fundamental equations are separated into the following sections

1. Mass conservation in solid material
2. Mass conservation in electrolyte
3. Charge conservation in solid material
4. Charge conservation in electrolyte

The battery electrodes' volumes are divided into the electrolyte and solid material phases, represented with subscripts as e and s, respectively. The phase volume fraction ϵ_s, and its definition is seen in equation 3.5 where V_s and V represent the volume of the solid electrode material and the total volume of the electrode, respectively.

$$\epsilon_s = \frac{V_s}{V} \tag{3.5}$$

3.2.1.1 Solid Mass Conservation

In these models, the particle is spherical, and the particle's concentration is spherically symmetric at that point. Considering these assumptions, the solid diffusion of particles through the solid material is modeled with Fick's second law of diffusion seen in equation 3.6 where c_s,D_s, r^2 are the solid lithium concentration, the diffusion constant, and the radius of the particle, respectively.

$$\frac{\partial c_s}{\partial t} = \frac{1}{r^2}\frac{\partial}{\partial r}(D_s r^2 \frac{\partial c_s}{\partial r}) \tag{3.6}$$

3.2.1.2 Electrolyte Mass Conservation

Assuming that there is also mass conservation in the electrolyte mass conservation is equation 3.7, where the concentration of lithium in the electrolyte, the electrolyte diffusion coefficient, the current through the electrolyte, the transference number, and the velocity of the solvent are c_e, D_e, i_e, t_+^0 and v_0 respectively.

$$\frac{\partial c_e}{\partial t} = \nabla \cdot (D_e \nabla c_e) - \frac{i_e \nabla t_+^0}{F} - (\nabla \cdot c_e v_0) \tag{3.7}$$

Assuming that the phases,do not deform $v_0 = 0$, and that the transference number within for the concentration is $t_+^0 = 0$. This simplifies equation 3.7 into equation 3.8

$$\frac{\partial \bar{c}_e}{\partial t} = \frac{1}{\epsilon_e}(\frac{\partial(\epsilon_e \bar{c}_e)}{\partial t}) \tag{3.8}$$

A brief explanation of the transference number is provided here. The transference number is a ratio of how much current (of the total current) a specific species in solution carries. This topic is unintuitive, so it will be briefly expanded upon. As provided by equation 2.5, the charge of each of the cations and anions in the electrolyte solution must sum to zero, and this is across all local areas; due to this, as the anode and cathode consume and donate cations in the electrodic regions, a gradient develops so the ions must redistribute to stay in line with equation 2.5. However, due to various parameters such as particle radius and viscosity of electrolyte, the ions redistribute at different rates. For further clarification, an example provided by [231] is provided here. Take a cell with an average electrolyte concentration of c_{avg} with both an anode and a cathode and a long middle section between the electrode regions as seen in figure 3.2.1a. Briefly apply a current i for a duration t. Figure 3.2.1b shows a close-up of the anodic region along with the representative behavior of the anions and cations (which are represented as the purple and orange circles, respectively). Under the current load, cations will flow into the electrolyte, and positive charge in the anodic region will increase. At the boundary of the anode and bulk region, both cations will flow out into the bulk electrolyte, and anions will flow from the bulk electrolyte into the anode region. As there is a *difference* between the rates at which these ions can travel, the cations only carry a fractional amount of the current. This, in principle, is the transference number. This idea becomes even clearer when looking at the transference number equation calculation as seen in equation 3.9 [231].

Here c_{final},V_{anode},Z, and F represent the final concentration of cations, the anode volume, unitless multiplicative coefficient for the cation of interest in the stoichio-

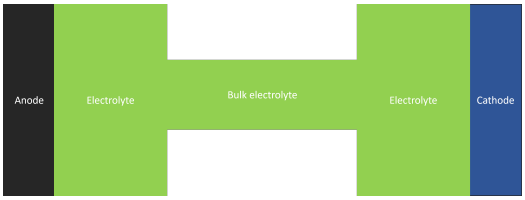

(a) Transference number cell set up adapted from [231]

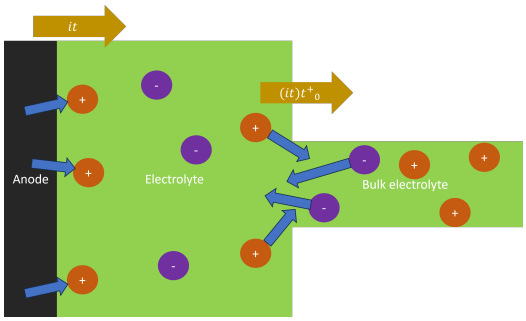

(b) Ion movement explanation adapted from [231]

metric equation to convert the number of coulombs to moles, and Faraday's constant respectively.

$$(c_{final} - c_{avg})V_{anode} = \frac{it - itt_+^0}{ZF} \tag{3.9}$$

Rearranging this equation would solve for the transfer number at the specific concentration c_{avg}, however, the relationship will no longer be expanded upon as these equations were solely examples provided for demonstrative purposes to explain the concept of the transference number.

D_e is represented with the equation 3.10 shown below

$$D_{eff} = D_e \epsilon^{Brugg} \tag{3.10}$$

Before moving on to the final equation, the intrinsic volume average described by the equation 3.11 is provided. Here bar represents the average of the phase variable under the bar, f represents a phase variable of interest, and A represents the area between two different phases of material.

$$\bar{\nabla} \cdot f = \nabla \cdot \bar{f} + \frac{1}{V} \oiint_A f \cdot \hat{n} \cdot dA \tag{3.11}$$

Plett [84] provides a more in-depth explanation and these details for brevity will not be included here. The theorem of equation 3.11 states that the divergence of a phase average and the volume averaged flux through the surface V is equal to the phase average of the divergence.

Taking the right-hand side of equation 3.7 and using the theorem of 3.11, the two equations expand to equation 3.12

$$\nabla \cdot (D_e \bar{\nabla} _e) = \frac{1}{\epsilon_e}(\nabla \cdot (\epsilon_e \bar{D}_e \nabla c_e) + \frac{1}{V} \iint_{A_{s-e}} D_e \nabla c_e \hat{n_e} dA) \tag{3.12}$$

The first portion of the right-hand side of the 3.12 can be approximated with the equation 3.13

$$\nabla \cdot (\epsilon_e \bar{D}_e \nabla c_e) \approx \nabla \cdot D_{eff} \nabla \bar{c_e} \tag{3.13}$$

The second portion of right hand side of the equation 3.12 can be simplified to 3.14

$$frac1V \iint_{A_{s-e}} D_e \nabla c_e \hat{n_e} dA = as(1 - t_+^0) \tag{3.14}$$

These last intermediary steps can then be used to find the final equation 3.15.

$$\frac{\partial(\epsilon_e \bar{c_e})}{\partial t} = \nabla \cdot (D_{eff} \nabla \bar{c_{eff}}) + a_s(1 - t_+^0) \tag{3.15}$$

3.2.1.3 Solid Charge Conservation

Starting with the microscale definition. Ohm's law, equation 3.16, states

$$\nabla \cdot i_s = \nabla \cdot (-\sigma \nabla \phi_s) = 0 \tag{3.16}$$

Where I_s, σ, and ϕ_s are the current in the solid material, solid material conductivity, and the potential of the solid material, respectively.

Using the theorem from equation 3.11 the gradient term of equation 3.16 can be transformed into equation 3.17

$$\nabla \cdot \bar{-\sigma} \nabla \phi_s = \nabla \cdot \nabla - \bar{\sigma} \nabla \phi_s + \frac{1}{V} \iint_{A_{s-e}} (-\sigma \nabla \phi_s) \cdot \hat{n_s} dA \tag{3.17}$$

The second part of the right-hand side of equation 3.17 can be simplified with

assumptions as seen in 3.18

$$\frac{1}{V}\oiint_{A_{se}}(-\sigma\nabla\phi_s)\hat{n_s}\,dA = \frac{1}{V}Fj \approx \frac{A_{se}}{V}Fj \approx a_sFj \tag{3.18}$$

Where a_s is defined as equation 3.19

$$a_s = \epsilon_s\frac{4\pi R_{part}^2}{\frac{4}{3}\pi R_{part}^3} = \frac{3\epsilon_s}{R_{part}} \tag{3.19}$$

which represents the overall SEI's area A_{s-e} to the overall volume of the solid material V. The gradient in the solid potential from the latter section of equation 3.16 can be modeled as equation 3.20

$$\sigma\bar{\nabla}\phi_s \approx \sigma_{eff}\nabla\bar{\phi_s} \tag{3.20}$$

Where σ_{eff} is the effective conductivity, the bar notation defines the intrinsic phase average of the variable of interest. This effective conductivity is the bulk conductivity of the material properties appropriately scaled by the amount of the solid material within the battery, which is equation 3.21

$$\sigma_{eff} = \frac{\epsilon_s\sigma\delta}{\tau} \tag{3.21}$$

Where δ and τ are the material's constrictive and tortuosity, these values naturally range such that $\sigma_{eff} < \sigma$.

As the model simplifies the battery domains to a homogenous porous material, the material properties must be adjusted to consider this assumption. Bruggeman's coefficient is widely employed to encompass this porous media behavior [232]. This exponent relation is shown in equation 3.22.

$$\sigma_{eff} = \sigma\epsilon_s^{Brugg} \tag{3.22}$$

. The $Brugg$ is the Bruggeman coefficient, which is usually considered 1.5.

Assuming that the boundary condition on the electrolyte surface is $-Fj$, where

F is Faraday's constant, which is approximately equal to 96485 $\frac{C}{mol}$, and j, is the current flux necessary to supply the total current to the load of the battery. From all of these points, the final equation is

$$\nabla \cdot (-\sigma_{eff} \nabla \phi_s) = -a_s F \bar{j} \tag{3.23}$$

The standard value standard of 1.5 was used for the Bruggeman constant, but it is noted here that a change in this value could theoretically bring about better results.

3.2.1.4 Electrolyte charge conservation

The charge conservation in the electrolyte is equation 3.24, where i_e, κ, ϕ_e, R, T, F,f, c_e,t_+^0 are the electrolyte current, electrolyte conductivity, electrolyte potential, the universal gas constant, Faradays constant, molar activity coefficient, the electrolyte concentration, and the transference number respectively.

$$\nabla \cdot i_e = \nabla \cdot (-\kappa \nabla \phi_e - \frac{2\kappa RT}{F}(1 + \frac{\partial ln f}{\partial ln c_e})(t_+^0 - 1)\nabla ln(c_e)) = 0 \tag{3.24}$$

For brevity in further equations, some of the terms in equation 3.24 will be grouped into a single variable based on 3.25

$$\kappa_D = \frac{2\kappa RT}{F}(1 + \frac{\partial ln f}{\partial ln c_e})(t_+^0 - 1) \tag{3.25}$$

this when replacing its equivalent terms in equation 3.24 becomes equation 3.26

$$\nabla \cdot i_e = \nabla \cdot (-\kappa \nabla \phi_e - \kappa_D \nabla ln(c_e)) = 0 \tag{3.26}$$

Once again, to encompass the behavior of porous media, Bruggeman's exponent relation is applied, so equation 3.27 is used.

$$\kappa_{D,eff} = \kappa_D \epsilon_e^{Brugg} \quad \text{and} \quad \kappa_{eff} = \kappa \epsilon_e^{Brugg} \tag{3.27}$$

By using equation 3.27 in equation 3.26, equation 3.28 is achieved.

$$\nabla \cdot i_e = \nabla \cdot (-\kappa \nabla \phi_e - \kappa_{D,eff} \nabla ln(c_e)) = 0 \tag{3.28}$$

By using the theorem described by equation 3.11 on the left-hand side of equation 3.28, the relation shown in equation 3.29 is found.

$$\bar{\nabla \cdot} i_e = \nabla \cdot \bar{i_e} + \frac{1}{V} \oiint_A i_e n dA \tag{3.29}$$

The last term of equation 3.29 is the current across the surface of the particle, and so is rewritten as $-a_s F \bar{j}$. This rewrite changes equation 3.29 into equation 3.30

$$\bar{\nabla \cdot} i_e = \nabla \cdot \bar{i_e} - a_s F \bar{j} = 0 \tag{3.30}$$

from equation 3.28 it can be seen that

$$i_e = -\kappa \nabla \phi_e - \kappa_{D,eff} \nabla ln(c_e) \tag{3.31}$$

taking replacing i_e in equation **??** with equation 3.31, equation 3.32 is achieved.

$$\nabla \cdot (\kappa_{eff} \nabla \phi_e - \bar{\kappa}_{D,eff} \nabla ln(c_e)) - a_s F \bar{j} = 0 \tag{3.32}$$

The final equation representing charge conservation in electrolyte becomes equation 3.33

$$\epsilon_e \bar{i_e} = -\kappa_{eff} \nabla \bar{\phi_e} - \kappa_{D,eff} \nabla ln(c_e) \tag{3.33}$$

and equation 3.34

$$\nabla \cdot (\kappa_{eff} \nabla \bar{\phi_e} + \kappa_{D,eff} \nabla ln \bar{c_e}) + a_s \bar{j} F = 0 \tag{3.34}$$

3.2.2 SPM Equation Boundary Conditions

The boundary conditions for each of the sections are as follows;

For the charge conservation in the positive electrode, the boundary conditions (BCs) were the equations 3.35

$$\frac{\partial \bar{\phi_s}}{\partial x}|_{L_{neg}+L_{sep}} = 0 \quad \frac{\partial \bar{\phi_s}}{\partial x}|_{L_{tot}} = \frac{-I_{applied}}{A\sigma_{eff}} \tag{3.35}$$

The anode charge conservation BCs can be seen in equation 3.36

$$\frac{\partial \bar{\phi_s}}{\partial x}|_{L_{neg}} = 0 \quad \bar{\phi_s}|_{L_{neg}} = \frac{-I_{applied}}{A\sigma_{eff}} \tag{3.36}$$

The BCs for the conservation of mass within the solid materials, both in the cathodic and anodic regions, are seen in equation 3.37

$$\frac{\partial \bar{c_s}}{\partial r}|_{r=0} = 0 \quad \frac{\partial \bar{c_s}}{\partial r}|_{r=R_s} = -\bar{j} \tag{3.37}$$

The conservation of mass BCs is shown in the equation 3.38

$$\frac{\partial \bar{c_e}}{\partial x}|_{x=0} = \frac{\partial \bar{c_e}}{\partial x}|_{x=L_{tot}} = 0 \tag{3.38}$$

For the conservation of charge in the electrolyte, the BCs are shown in equations 3.39 and 3.40

$$\kappa_{eff}\frac{\partial \bar{\phi_e}}{\partial x} + \kappa_{D,eff}\frac{\partial ln\bar{c_e}}{\partial x}|_{x=0} = \kappa_{eff}\frac{\partial \bar{\phi_e}}{\partial x} + \kappa_{D,eff}\frac{\partial ln\bar{c_e}}{\partial x}|_{x=L_{tot}} = 0 \tag{3.39}$$

$$\kappa_{eff}\frac{\partial \bar{\phi_e}}{\partial x} + \kappa_{D,eff}\frac{\partial ln\bar{c_e}}{\partial x}|_{x=L_{neg}} = \kappa_{eff}\frac{\partial \bar{\phi_e}}{\partial x} + \kappa_{D,eff}\frac{\partial ln\bar{c_e}}{\partial x}|_{x=L_{neg}+L_{sep}} = -\frac{I_{applied}}{A} \tag{3.40}$$

3.2.3 Butler-Volmer Equation - Electrochemical Kinetics

An electrochemical model would only be complete with the mention of the Butler-Volmer equation. The Butler-Volmer equation relates the reaction rates of the electrode to the overpotential of the electrode. The overpotential is the excess voltage of the solid material (which is related to the overall voltage) above its equilibrium value. This relation is seen in equation 3.41 where η , ϕ_s, ϕ_e, U_{OCP}, F, R_{film}, and j respectively represent the voltage overpotential, the electrode solid potential, the electrolyte potential, the open circuit potential, Faraday's constant, the film resis-

tance of the electrode, and the flux across the boundary of the electrode. In this thesis, the R_{film} is assumed to be negligible.

$$\eta = \phi_s - \phi_e - U_{OCP} - FR_{Film}j \tag{3.41}$$

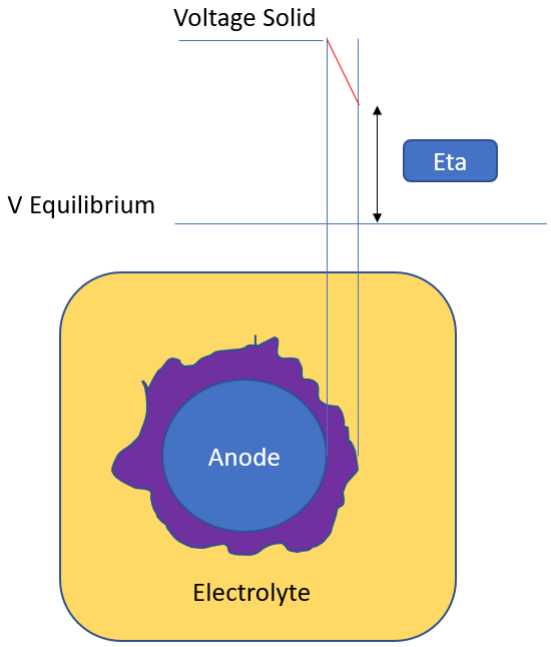

Fig. 3.2.2: Overpotential of electrode

The total reaction rate of the electrode can be further broken down into oxidation and reduction rates. The combination of these results is the total reaction rate. With this in mind, the Butler-Volmer equation is 3.42.

$$j = j_{oxidization} - j_{reduction} = k_{norm}(e^{\frac{\alpha}{RT}} - e^{\frac{1-\alpha}{RT}}) \tag{3.42}$$

k_{norm} is the normalized reaction rate coefficient, and a further relationship between k_0, or the reaction rate coefficient, is defined in equation 3.43

$$k_{norm} = k_0 c_e^{1-\alpha}(c_{s,max} - c_{s,e})^{1-\alpha} c_{s,e}^{\alpha} \tag{3.43}$$

With equation 3.43 and equation 3.42 finally, the coupled equation becomes equa-

tion 3.44

$$j = k_0 \cdot c_e^{1-\alpha} \cdot (c_{s,max} - c_{s,e})^{1-\alpha} \cdot (e^{\frac{\alpha}{RT}} - e^{\frac{1-\alpha}{RT}}) \tag{3.44}$$

3.2.4 Discrete-Time Realization Algorithm

The discrete-time realization algorithm (DRA) models complex systems' behavior using simplified responses from a linearized state space model. This algorithm, also called the eigenvalue realization algorithm (ERA), has successfully modeled highly complex behaviors, from the behavior of satellites to the voltage behavior of batteries.

Before proceeding with the following steps, a general simplified overview of the steps for the DRA is presented. Take a linear state space model such as seen in equations 3.45 and 3.46 holds.

$$x[k+1] = Ax[k] + Bu[k] \tag{3.45}$$

$$y[k] = Cx[k] + Du[k] \tag{3.46}$$

let O be the observability matrix seen in equation 3.47

$$\begin{bmatrix} C \\ CA \\ CA^2 \\ \vdots \\ CA^{n-1} \end{bmatrix} = O \tag{3.47}$$

and the Cr be the controllability matrix represented in equation 3.48

$$\begin{bmatrix} B & BA & BA^2 & \dots & BA^{n-1} \end{bmatrix} = Cr \tag{3.48}$$

The Hankel matrix H is defined as the multiplication between equation 3.48 and equation 3.47, as seen in equation 3.49

$$H = [O][Cr] = \begin{bmatrix} CB & CAB & \dots & CA^{n-1}B \\ CAB & CA^2B \dots & \dots & \vdots \\ \vdots & \dots & \dots & \vdots \\ CA^{n-1}B & \dots & \dots & CA^{2n-2}B \end{bmatrix} \tag{3.49}$$

The shifted Hankel matrix is the Hankel matrix with all positions shifted by one row. The shifted Hankel matrix H_{k+1} can be seen in equation 3.50.

$$H = \begin{bmatrix} CAB & CA^2B & \dots & CA^nB \\ CA^2B & CA^3B \dots & \dots & \vdots \\ \vdots & \dots & \dots & \vdots \\ CA^nB & \dots & \dots & CA^{2n-1}B \end{bmatrix} \tag{3.50}$$

If one could have and be able to factor H, then the state space models for $A, B, C, andD$ can be found. This factoring was done with the singular value decomposition method seen in 3.51

$$M = U\Sigma V^T \tag{3.51}$$

and for further clarity, the Hankel matrix can be represented using equation 3.51

$$H = U\Sigma V^T = U\Sigma^{0.5}\Sigma^{0.5}V^T \tag{3.52}$$

This leads to the conclusion found in the equation 3.53

$$O = U\Sigma^{0.5}I \tag{3.53}$$

and

$$Cr = I^{-1}\Sigma^{0.5}V^{T} \tag{3.54}$$

.

The last step in the decomposition process displays how each A, B, C, and D matrices were calculated. These are respectively seen in equations 3.55, 3.56,3.57, and 3.58

$$A = O^{-1}H_{k+1}Cr^{-1} \tag{3.55}$$

$$B = Cr(1:n, 1:m) \tag{3.56}$$

$$C = O(1:n, 1:m) \tag{3.57}$$

$$D = 0 \tag{3.58}$$

Now that the background of the DRA has been established, the first step of the DRA in the sequential process can be clearly explained. The various PDEs of the prescribed formulas seen in section 3.2 that describe the mass and charge transfer of the batteries need to be simplified and converted into transfer functions. To be succinct, the various PDE forms will be listed here without derivation. For the derivation, see [84].

For the electrochemical model, the battery domain is broken up into three distinct sections, where each section is normalized with respect to its length. The sections are anode, separator, and cathode. The length of each section is labeled between zero and one. Zero demarks the boundary between the electrode and the current

collector, and one demarks the boundary between the electrode and the separator. This representation is clarified in Fig. 3.2.3.

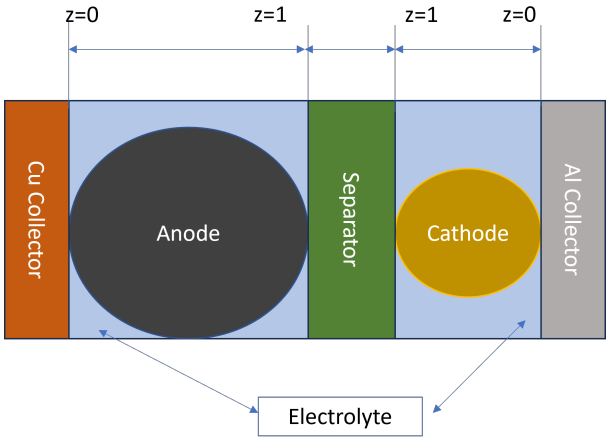

Fig. 3.2.3: 1D SPM layout

The difference between the potentials in the solid electrode material and the electrolyte is simplified using the equation 3.59

$$\phi_{s-e} = \phi_s - \phi_e \tag{3.59}$$

In keeping with the derivation provided by [230], two variables are rewritten for simplification and are defined here as ν as seen in equation 3.60 and β seen in equation 3.61. The definition of these variables is provided here to simplify the overall reading of the transfer functions. Plett [84] interprets ν^2 as the ratio between frequency and SOC-related impedances within the battery.

$$\nu(s) = \frac{L(\frac{a_s}{\sigma_{eff}} + \frac{a_s}{\kappa_{eff}})}{\sqrt{R_{s,e} + \frac{\partial U_{ocp}}{\partial c_{s,e}}|_{c_{s,0}} \frac{R_s}{FD_s} \frac{1}{1-\beta coth(\beta)}}} \tag{3.60}$$

$$\beta = R_s\sqrt{\frac{s}{D_s}} \tag{3.61}$$

The potential at the surface of the solid is described by equation 3.62

$$\frac{\tilde{\phi_{s-e}}(z,s)}{I_{applied}(s)} = L\frac{\sigma_{eff}cosh(\nu(s)z + \kappa_{eff}cosh(\nu(s)(z-1)}{A\sigma_{eff}\kappa_{eff}\nu(s)sinh(\nu(s))} \tag{3.62}$$

The concentration of the surface of the electrode is described by equation 3.63. Here tilde represents the difference between the initial and current amounts for the variable of interest.

$$\frac{\tilde{C_{s,e}}(z,s)}{I_{app}(s)} = \frac{\sigma_{eff}cosh(\nu(s)z + \kappa_{eff}cosh(\nu(s)(z-1)}{a_sFLAD_s(\kappa_{eff}+\sigma_{eff})sinh(\nu(s))} \frac{R_s\nu(s)}{1-\beta coth(R_s\frac{s}{D_s})} \tag{3.63}$$

Equation 3.64 provides the transfer function for the difference in solid potential

$$\begin{aligned}\frac{\tilde{\phi_s}(z,s)}{I_{app}(s)} = -L_{neg}(&\frac{\kappa_{eff}(cosh(\nu(s)) - cosh(z-1)\nu(s))}{A\sigma_{eff}(\kappa_{eff}+\sigma_{eff})\nu(s)sinh(\nu)} + \\ &+\frac{\sigma_{eff}(1-cosh(z\nu(s)) + z\nu(s)sinh(\nu(s)))}{A\sigma_{eff}(\kappa_{eff}+\sigma_{eff})\nu(s)sinh(\nu)}\end{aligned} \tag{3.64}$$

and the equation 3.65 for the flux of the particle

$$\frac{J}{I_{applied}} = \nu(s)\frac{\sigma_{eff}cosh(\nu(s)z\kappa_{eff}cosh(\nu(s)(z-1)}{a_sFLA(\kappa_{eff}+\sigma_{eff})sinh(\nu(s))} \tag{3.65}$$

The equations 3.60, 3.61, 3.62, 3.64, 3.65 apply equally both to the positive and to the negative electrode. However, with a brief caveat, the equations above refer to the anode, but each equation is multiplied by a negative sign for the cathode.

The PDEs for the electrolyte domain are written as a Sturm-Liouvielle problem, an ODE of the form seen in equation 3.66

$$\frac{d}{dx}(p(x)\frac{\psi(s)}{dx}) + q(x)\psi(x) + \lambda w(x)\psi(x) = 0 \tag{3.66}$$

The solutions to these equations are known to many elementary mathematical textbooks, and their solutions will not be listed here.

The concentration of the electrolyte is given by

$$\tilde{c_e} = \sum_{n=0}^{\infty} h(0;\lambda_n)\Psi(x;\lambda_n)e^{-\lambda_n t} \tag{3.67}$$

The input into the 1D model is the discharge and charging current for each drive cycle. These currents were provided for each drive cycle at the cellular level to simulate

the voltage and heat generation responses.

3.3 Genetic Algorithm Methodology

To estimate the parameters of the battery, the GA algorithm was used. Many of the parameters were kept constant with values that were either taken from convention or from the material data, which [233, 234, 235, 236, 237] have investigated. The values labeled as "given" are not unchanging. They are values that have been provided or are not solved by the GA. While the variables marked "varied" were augmented and estimated by the GA.

Some clarifications may be in order; the lengths of the electrodes directly affect the behavior of the battery but are labeled in the table 3.3.1 as "given". This categorization is because the lengths were calculated based on the relation given below in equation 3.68. Where $C_{electrode}$, $V_{electrode}$, $\rho_{available}$ are the total electrode capacity, the total volume of the electrode, and the density of the volume that has available capacity, respectively. These variables are then related to the variables described previously in table 3.3.1.

$$C_{electrode} = V_{electrode}\rho_{available} = A_c F L \epsilon_s c s_{max}(\theta_{max} - \theta_{min}) \tag{3.68}$$

if the capacity is wanted in Ah then equation 3.68 is divided by 3600.

$$C_{batt} = C_{anode} = C_{cathode} \tag{3.69}$$

In this way, by varying the C_{batt}, both the lengths of the electrodes are "given."

For convenience, table 3.3.2 below shows only the variables estimated by the GA and the minimum and maximum boundaries to keep the estimation ranges within. These ranges are values were chosen as many previous literature sources have values within these upper and lower limits.

As stated in section 3.1, the GA needs input for the size of the population, the condition of ending, and the decision of crossover and mutation characteristics. For

Table 3.3.1: 1D SPM variables

Parameter	Value	Parameter Description
$\sigma_{anode}(\frac{S}{m})$	given	Anodic electric solid conductivity
$\epsilon_{anode}(ul)$	varied	Anodic solid volume fraction
$c_{s,max,anode}(\frac{mol}{m^3})$	given	Anodic maximum solid concentration
$c_{s,min,anode}(\frac{mol}{m^3})$	given	Anodic minimum Solid concentration
$R_{p,anode}(m)$	varied	Anodic particle radius
$\epsilon_{e,anode}(ul)$	varied	Anodic electrolyte solid fraction
$D_{s,anode}(\frac{m^2}{s})$	given	Anodic solid diffusion
$L_{neg}(m)$	given	Anodic length
$\theta_{anode,max}(ul)$	given	Anodic max stoichiometry
$\theta_{anode,min}(ul)$	given	Anodic min stoichiometry
$\sigma_{cathode}(\frac{S}{m})$	given	Cathodic electric solid conductivity
$\epsilon_{cathode}(ul)$	varied	Cathodic solid volume fraction
$c_{s,max,cathode}(\frac{mol}{m^3})$	given	Maximum solid concentration
$c_{s,min,cathode}(\frac{mol}{m^3})$	given	Minimum solid concentration
$R_{p,cathode}(m)$	varied	Cathodic particle radius
$\epsilon_{e,cathode}(ul)$	given	Cathodic electrolyte solid fraction
$D_{s,cathode}(\frac{m^2}{s})$	given	Cathodic solid diffusion coefficient
$L_{pos}(m)$	given	Cathodic electrolyte solid fraction
$L_{sep}(m)$	varied	Separator length
$\theta_{cathode,max}(ul)$	given	Cathodic max stoichiometry
$\theta_{cathode,min(ul)}$	given	Cathodic Min stoichiometry
$\epsilon_{sep}(ul)$	varied	Separator solid volume fraction
$A_c(m^2)$	given	Battery cross-sectional area
$Q_{Batt}(ul)$	varied	Battery Capacity

Table 3.3.2: 1D SPM GA variables

Parameter	Estimation Range [min,max]	Parameter Description
$\epsilon_{anode}(ul)$	$[0.2, 0.6]$	Anodic Solid volume fraction
$R_{p,anode}(m)$	$[10^{-6}, 10^{-3}]$	Anodic Particle Radius
$\epsilon_{cathode}(ul)$	$[0.2, 0.6]$	Cathodic Solid volume fraction
$R_{p,cathode}(m)$	$[10^{-6}, 10^{-3}]$	Cathodic Particle Radius
$L_{separator}(m)$	$[0.5L_{neg}, 1.5L_{neg}]$	Separator Length
$\epsilon_{separator}(ul)$	[0.2,0.6]	Separator Solid volume fraction
$C_{Batt}(ul)$	$[0.95 * C_{nom}, 1.05 * C_{nom}]$	Battery Capacity

the simulations, the crossover and mutation characteristics were adaptively changed, with the methodology for crossover being stochastic universal sampling selection. The ending condition was a maximum number of generations, with the maximum generation number being 20. This number was chosen as previous studies have shown its success [238] where the maximum number of generations was 15.

The charging and discharging load for the battery at 25 °C from the HPPC was used to train the model, and the result to be minimized is the well-known root mean squared error (RMSE) seen in equation 3.70. Where V_k, n, and v_k are the experimental voltage at time step k, the total number of time steps, and the estimated voltage at time step k, respectively.

$$RMSE = \sqrt{\frac{1}{n}\sum_{k=1}^{n}(V_k - v_k)^2} \tag{3.70}$$

3.4 Battery Heat Generation

Heat within a cell is generated from multiple sources; typically, the ones considered are Joule heating and heat due to entropy change [239]. The Joule heating is due to the current across the various internal resistances of the cell; this irreversible heat generation is described by the equation 3.71 [240, 241]. Here $\dot{Q_{irrev}}$, I, OCV, V, and

η represent the irreversible heat generation, the current, the open circuit voltage. the voltage applied, and the overpotential of the battery respectively.

$$\dot{Q}_{irrev} = I(OCV - V) \approx I\eta \tag{3.71}$$

The heat generation due to the internal entropy change from the chemical reaction is often described as reversible. This reversible heat generation can be seen in equation 3.72, where,

$$\dot{Q}_{rev}$$

, T, $\frac{dOCV}{dT}$ represent the reversible heat generation, absolute temperature and the gradient of the OCV with respect to temperature.

$$\dot{Q}_{rev} = -IT\frac{dOCV}{dT} \tag{3.72}$$

As such, combining the two heat generation terms provides the total heat generation equation as seen in equation 3.73.

$$\dot{Q}_{tot} = \dot{Q}_{irrev} + \dot{Q}_{rev} = I\eta - IT\frac{dOCV}{dT} \tag{3.73}$$

As can be seen from equations 3.42 and 3.72, the battery's temperature affects the behavior and the magnitude of the heat generation. Due to this, one cannot solely use the heat generation of a singular drive cycle at a specific temperature and correspondingly apply these values to estimate the temperatures of the battery. To overcome this problem, a heat generation map (heat map) like the one seen in Fig. 3.4.1 was created over a range of likely temperatures for the batteries under operation. This heat map is created by simulating the proposed drive cycle at varying constant temperatures with the same loading conditions; the heat generation at each step is calculated until the end of the drive cycle. In this way, the SOC-dependent properties should be estimated correctly. With this heat map alone as an input, the coupled properties between heat generation and temperature should be captured.

These heat generation maps were generated across all drive cycles.

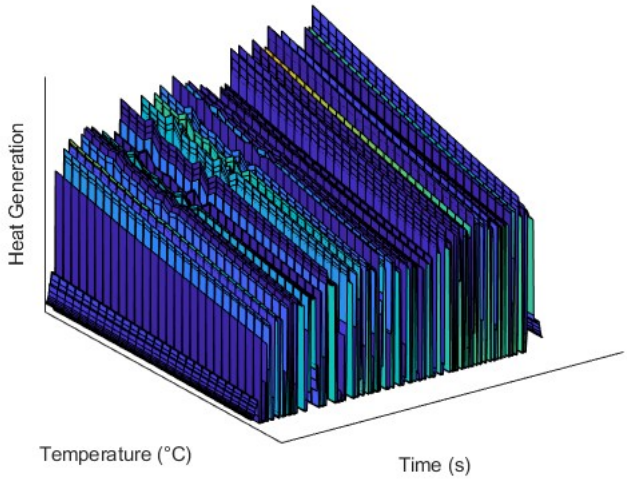

Fig. 3.4.1: Heat generation map over drive cycle

3.5 Thermal 3D Model

Using the heat generation model from the 1D SPM described in section 3.2, the heat maps were applied to the active jelly roll sections of the battery. The measured average temperature of the jelly roll was then used to calculate the next timestep's heat generation. In this way, the overall heat generation effect was included in the 3D model.

3.5.1 Cell Model

This section explains the thermal cell model's setup to provide the utmost clarity and transparency to the research process. First, geometry and its constructions are discussed, then the cell model thermal governing equations and their respective boundary conditions are explained.

3.5.1.1 Cell Geometry

The geometry and boundary conditions of the COMSOL multiphysics ©model will be discussed here. The simulation conditions of the proposed cell model are a cell exposed to ambient air under the proposed drive cycles. The geometry of interest

without augmentation for simulations is a standard prismatic battery shown in three different views seen in Fig. 3.5.1.

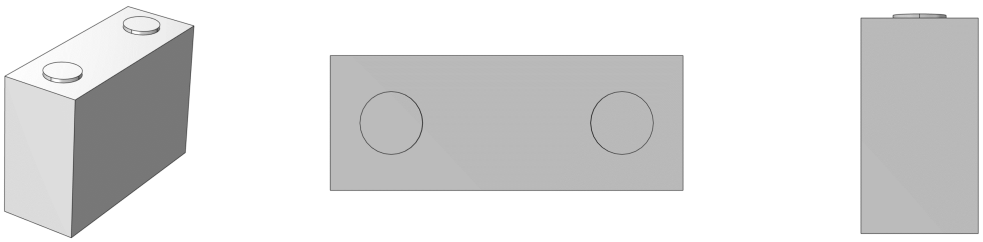

Fig. 3.5.1: Diagonal, top, and frontal views of cell level geometry

3.5.1.2 Thermal Cell Model Governing Equations and Boundary Conditions

The electrochemical, thermal heat model governing equations previously defined in section 3.4 must be redefined here. Using the electrochemical model to generate the previously mentioned heat maps, the thermal behavior of the 3D model was simulated. Before further details can be discussed, a few more critical governing equations must be described. Heat transfer within the battery at the cell level happens almost entirely through conductivity. Therefore the energy conservation equation defines the thermal behavior at a 3D model scale and is shown below in equation 3.74. This partial differential equation is one of the most well-known equations used in heat transfer simulations and is used extensively in cell and module modeling [242]. In this equation, ρ,c_p, T, and $\dot{q}_{int}$ are the density of the material, the heat capacity of the material at constant pressure, the temperature, and the internal heat generation.

$$\rho c_p \frac{\partial T}{\partial t} = \nabla \cdot (k \nabla T) + \dot{q}_{int} \tag{3.74}$$

The cell was in an ambient environment where natural convection was the main mode of heat flux out of the battery cell. The heat flux at this boundary condition was defined by equation 3.75. The equation was defined by the variables q_{conv} ,h_{conv},T, and T_∞, representing the heat flux due to convection, the convective heat transfer coefficient, the surface temperature, and the ambient temperature, respectively.

$$q_{conv} = h_{conv}(T - T_{\infty}) \tag{3.75}$$

The conductivity values, along with the heat capacity, were provided by Stellantis and, within the model, were constant and unchanging with temperature. These values were averaged values obtained for the cell and module and were uniformly distributed within the model across all of the volumetric domains.

Equation 3.75 for convective heat flux is critically dependent on an estimation for h_{conv}. A relation for the convective heat flux coefficient was necessary. A well-known and established convective heat flux correlation from [243] was used in [244] with success. This methodology was also employed at the cell and module level boundary conditions.

This relation is briefly provided here. With its methodology also clearly described in [245], its presentation for clarity of the reader will also follow its presentation. The correlation for both heat transfer coefficients is presented as the battery comprises several vertical and horizontal surfaces. Both horizontal and vertical estimations follow the same overall structure but have different correlations.

For a vertical plate heat transfer coefficient estimation in ambient air. The first step was calculating the Grashof number, a non-dimensional number representing the ratio of the fluid's buoyant to viscous forces. This equation can be seen from 3.76.

$$Gr = \frac{g\beta(T_{surface} - T_{\infty})L_c^3}{v^2} \tag{3.76}$$

Where g,β_{exp},L_c and v are the gravitational acceleration constant, the coefficient of volume expansion of the fluid, the characteristic length of the surface of interest, and the kinematic viscosity of the fluid respectively. It should be noted here that some of these characteristics are temperature-dependent for the fluid of interest. As such, all parameters were evaluated at the film temperature calculated from equation 3.77.

$$T_f = \frac{T_{surface} + T_{\infty}}{2} \tag{3.77}$$

The Rayleigh number was then calculated based on equation 3.76 shown below.

$$Ra = GrPr \tag{3.78}$$

Where Pr is the Prandtl number, a dimensionless characteristic number shown in equation 3.79, here α_{diff} is the thermal diffusivity of the fluid media.

$$Pr = \frac{v}{\alpha_{diff}} \tag{3.79}$$

After this step, the Nusselt number was calculated based on the well-known correlations for the battery's vertical and horizontal section [243]. These are shown in equations 3.80 and 3.81, respectively.

$$Nu = 0.825 + \frac{0.387Ra^{1/6}}{(1 + (\frac{0.492}{Pr})^{\frac{9}{19}})^{\frac{8}{27}}} \tag{3.80}$$

$$Nu = 0.59Ra^{\frac{1}{4}} \tag{3.81}$$

Finally, the heat transfer coefficient was calculated to be equation 3.82

$$h = \frac{k_{cond}}{L_c}Nu \tag{3.82}$$

Based on these correlations, and with the ambient air temperature being kept constant at 25 °C, the range of values for the surface temperature of interest produces two graphs for the vertical and horizontal heat transfer coefficient values shown in Fig.3.5.2.

The BCs of the problem were assumed to simulate the battery at ambient air conditions under natural convection. As the heat within the cell was assumed to be generated uniformly, a plane of symmetry was used to reduce the model's complexity. This reduction can be seen in Fig. 3.5.3.

With this simplification, the boundary conditions are fully applied and are shown below in Fig. 3.5.4. The first boundary condition is naturally the plane of symmetry previously discussed, and the internal jelly roll of the battery is the heat source domain

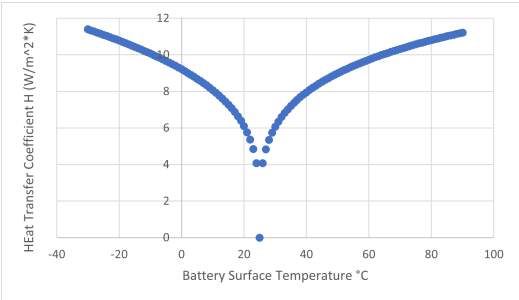

(a) Horizontal surface heat transfer coefficient estimations

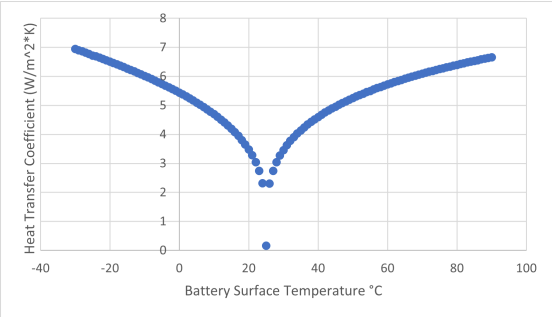

(b) Vertical surface heat transfer coefficient estimations

Fig. 3.5.2: Correlations for surface temperature-dependent heat transfer coefficients for horizontal and vertical surfaces

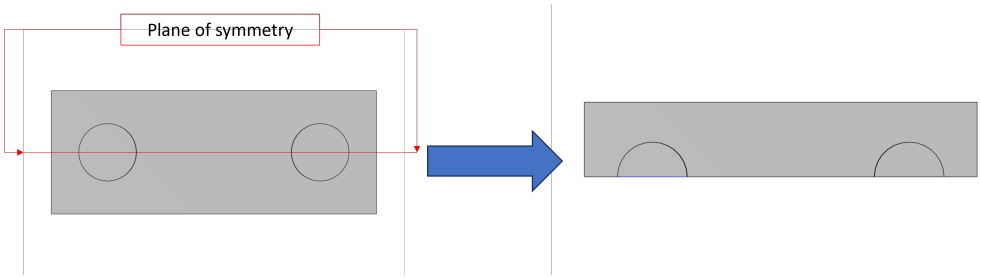

Fig. 3.5.3: Cell level plane of symmetry reduction

where the heat generation from the drive cycles is applied.

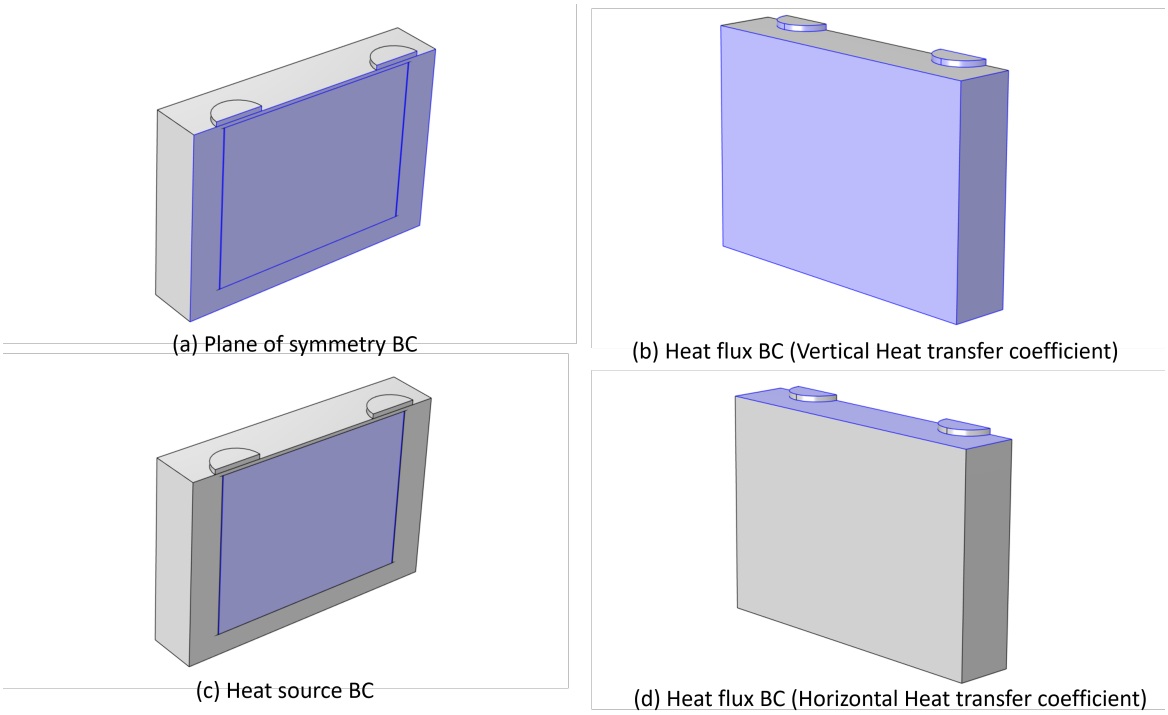

Fig. 3.5.4: Cell boundary conditions

3.5.2 Module Model

Here, the 3D model of the module will be discussed. The geometry build-up will be shown, and the thermal boundary conditions will be stated concretely to illustrate the modeling nuances and details, along with their implicit assumptions. The heat maps previously generated from the 1D SPM for the module level were used for the heat generation in the jelly roll domains. In this way, the unique and specific temperature and heat generation behaviors could be individually encapsulated for the entire 3D module's thermal behavior. The conductivity equation 3.74 along with the natural convective heat flux boundary equation 3.75 from section 3.5.1 remain the same and are not repeated here for brevity.

3.5.2.1 Module Geometry

The module-level comprises several cells in series, parallel, or a combination of both, as described in section 2.6.1. The module geometry is created by combining several cells. The simulations were similarly done in ambient air without forced convection; similar boundary combinations to the ones used at the cellular level were applied at the module level.

Here, the entire geometry is seen in 3.5.5

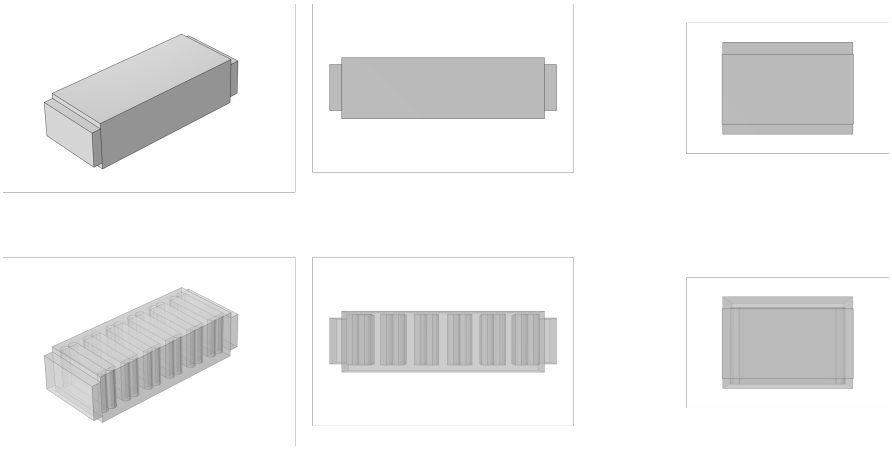

Fig. 3.5.5: Various views of module geometry

The thermal data for the module was provided as an averaged value, including all of the components; as such, geometry was simplified, being one continual material based on this averaged value. As such, the only domains of particular interest are the heat generation domains, which can be seen in the bottom row of the views shown in Fig.3.5.5.

As the simulation is similar to the cell, further simplifications were made to reduce the computational time. These simplifications take root in the form of the boundary conditions.

3.5.2.2 Module Thermal Boundary Conditions

The boundary conditions were highly similar to that of the cell model where, firstly, by identifying the planes of symmetry in the model, one can achieve a simplification which is shown in Fig.3.5.6.

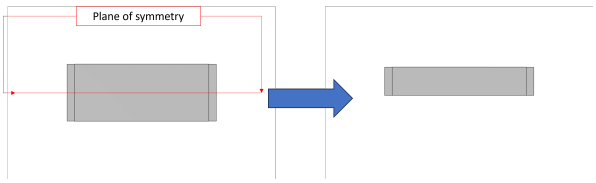

Fig. 3.5.6: First plane of symmetry module BC

A second plane of symmetry was also applied to the module, as shown in Fig. 3.5.7.

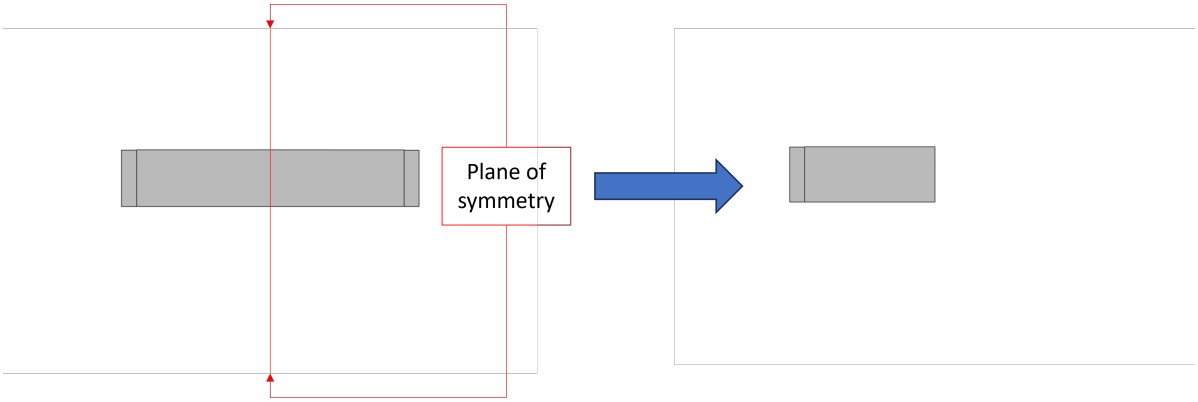

Fig. 3.5.7: Second plane of symmetry module BC

The jelly roll domains each had the heat map generated applied to its volumetric domain, where the heat map was evaluated at each of the average different jelly roll temperatures. This boundary condition can be seen in Fig. 3.5.8 below.

The same heat flux boundary conditions with the estimations of natural heat transfer coefficients were applied at the vertical and horizontal faces of the module 3.5.10. The ambient temperature was 25 degrees C.

The last boundary condition is the insulation condition at the bottom of the module.

3.5.3 Cell Model Grid Independence study

A grid independence study was carried out to verify that the results obtained from the numerical analysis are no longer dependent on the mesh size characteristics. The overall steps to complete the grid independence study are to

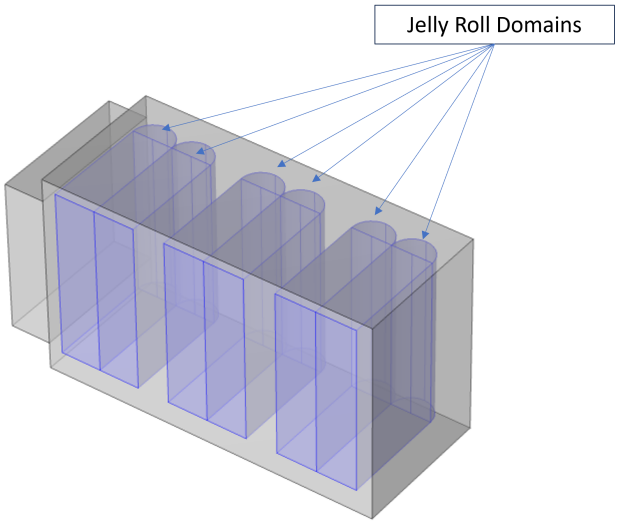

Fig. 3.5.8: Heat source boundary condition

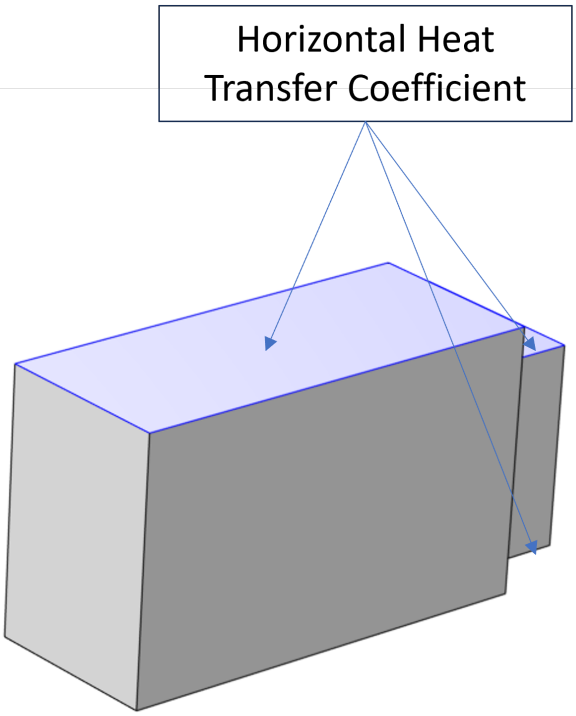

Fig. 3.5.9: Horizontal heat transfer coefficient BCs

Fig. 3.5.10: Heat flux boundary conditions based on horizontal and vertical heat transfer coefficients

Config No	Avg Surface T (°K)	Avg JR T (°K)	Max Cell T (°K)	Max JR T (°K)
1	303.66	303.81	303.82	303.94
2	303.66	303.8	303.82	303.94
3	303.66	303.81	303.82	303.94
4	303.66	303.81	303.82	303.94
5	303.66	303.81	303.82	303.94
6	303.66	303.81	303.82	303.94
7	303.66	303.81	303.82	303.94
8	303.66	303.81	303.82	303.94
9	303.66	303.81	303.82	303.94

Table 3.5.1: Cellular independence study

1. Identify a location of interest
2. Identify a result of interest
3. Vary the mesh to evaluate if the result changes based on the fidelity of the mesh

This process is shown in this section for the cellular function. The mesh size has been altered at varying lengths to verify the mesh behavior. The location and results of interest are expressed below.

1. Average cell temperature of external Faces
2. Average jelly roll temperature
3. Max cell temperature of external faces
4. Max jelly roll temperature

The mesh refinement process was completed over ten different mesh values to ensure a proper mesh density was reached, as seen in table 3.5.1.

As can be seen, the temperature behavior of the model was excellent. As such, the configuration in the center of this stable domain was chosen to ensure that a mix of certainty that the model is behaving correctly and the computational expense was reached.

3.5.4 Experimental Uncertainty Analysis

The uncertainty of an experiment comes from multiple sources, and an experiment can only be genuinely complete with some estimation of uncertainty from the resulting experiment.

Uncertainty within an experiment measurement propagates into the final results and, for completeness, must be included to provide an understanding of the overall sensitivity of the data. The methodology that will be followed is that described from [246, 247, 248].

That is the effect of the uncertainty of the indirect measurement, a "combined standard uncertainty" as seen in equation 3.83 with the final result can be calculated [248]. Where x_i is the i^{th} indirect measurement.

$$u^2 = (\sum_{i=1}^{n}(\frac{\partial f}{\partial x_i})^2 u^2(x_i) + 2\sum_{i=1}^{n-1}\sum_{j=i+1}^{n} u(x_i, x_j)) \tag{3.83}$$

If the different indirect measurements are uncorrelated, the second part of the equation approaches zero, and the equation simplifies to

$$u^2 = (\sum_{i=1}^{n}(\frac{\partial f}{\partial x})^2 u^2(x_i)) \tag{3.84}$$

CHAPTER 4

Results and Discussions

The results for the GA parameter estimations, cell-level voltage estimations, cell-level thermal simulations, and module-level thermal estimations are discussed at length here.

4.1 GA Results

The GA was completed four times using the methodology described in section 3.3, and its parameter estimations varied. Four separate runs provided different estimations for each of the different parameters. The estimated parameters are shown below in table 4.1.1. Although the runs provided different values for some parameters, other values had quantities to which the parameters did seem to converge, as seen from the table. This deviation among the parameter estimations is expected behavior; as previously stated, the GA can converge to local optimums. Due to this difference in parameter estimation, the values from the best run, Test # 4 are used throughout the simulations.

4.2 Cell Model Voltage Results

Here, the multiple drive cycle voltage results are broken down and discussed. The results showed good agreement with the experimental data using the estimated parameters from the GA.

Table 4.1.1: 1D SPM GA variables

Parameter	Test 1	Test 2	Test 3	Test 4
$R_{p,anode}(m)$	0.000987	0.0000185	0.0000315	0.00000175
$\epsilon_{anode}(ul)$	0.49	0.3777	0.377	0.3
$R_{p,cathode}(m)$	0.000816	0.001	9.71e-05	0.000001375
$\epsilon_{cathode}(m)$	0.45	0.449	0.447	0.3
$L_{separator}(m)$	0.00058	0.000501	0.00079	0.00027894
$\epsilon_{separator}(ul)$	0.48	0.48	0.41	0.4
$Q_{Batt}(ul)$	1.02	1.024	1.013	1.05

4.2.1 HPPC

A brief section from the HPPC discharge results at 25 °C is shown in Fig. 4.2.1. The parameter estimation functions appropriately. The RMSE for this simulation is $1.9 \times 10^{-3} V$, and its maximum difference is $0.22V$. Looking at the overall cycle trends seen in figure 4.2.1, the simulation follows the experimental voltage curve nicely. The curve in the central areas of the profile follows the voltage for smoother sections of current applications and the sporadic pulsing of the battery as well.

Some details to focus on in this result are the areas of improvement that could be applied. The boundaries of the charging and discharging section are where the simulation performed the least adequately. These are only small sections of the curve and, as such, did not consequently significantly affect the RMSE value. It is noted, however, that these areas could be improved. The simulation performed most well within the boundaries of around 5 % and 95 % SOC. This pattern also applied across many of the subsequent cycles.

4.2.2 WLTC Drive Cycle

Moving on to the WLTC drive cycle, one can see that the experimental and simulated data also follow each other closely in Fig.4.2.2. Although it is noted from the difference

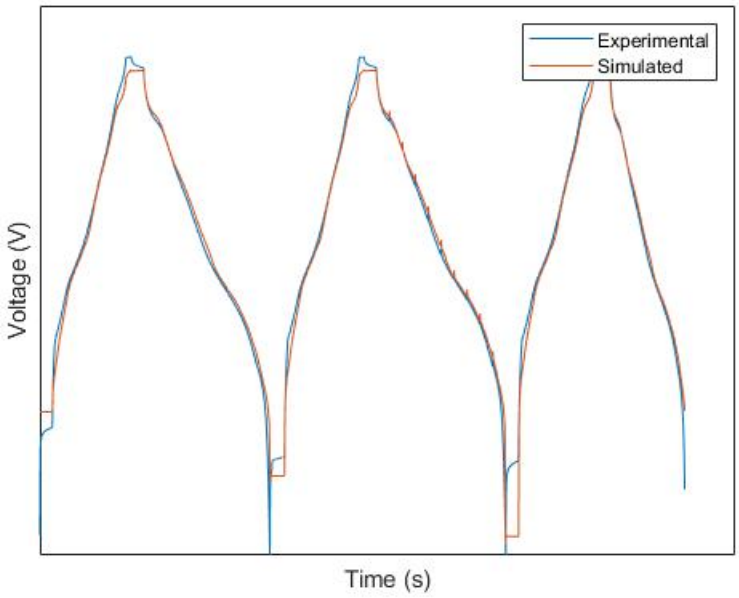

Fig. 4.2.1: HPPC voltage curves

between simulation and experimental, there is a slight offset between the two outputs. This offset can be seen in Fig.4.2.2b, where the maximum percent difference falls below 0.8 %, which is not very large in magnitude. Its RMSE value over the entire drive cycle is also meager, $9.65 \times 10^{-5}V$. These low values show that even though the RMSE value from the HPPC simulation is much larger, when the SOC range is between 95 % and above 5%, the model can accurately capture the battery's voltage behavior.

4.2.3 CLTC Drive Cycle

The CLTC drive cycle results in Fig. 4.2.3 show that the previous trend continues. Here, for added perspective, the percent difference has been swapped with the absolute difference. As before, the model captures the behavior of the cycle well with an RMSE value of 4.9×10^{-3} and a maximum voltage difference of $0.012V$.

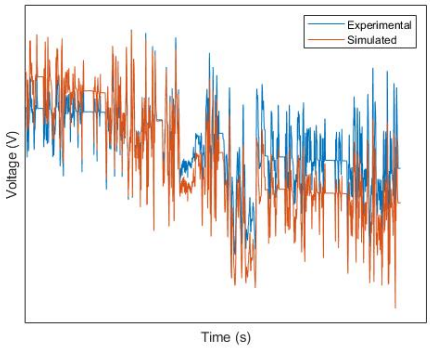

(a) Voltage comparison between simulated and experimental voltage profiles for WLTC curve

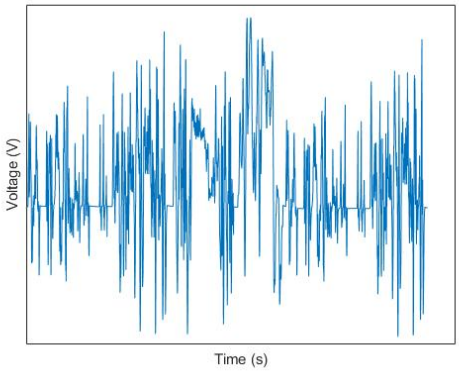

(b) Voltage percent difference comparison between simulated and experimental voltage profiles for WLTC curve

Fig. 4.2.2: Voltage results and comparison for WLTC

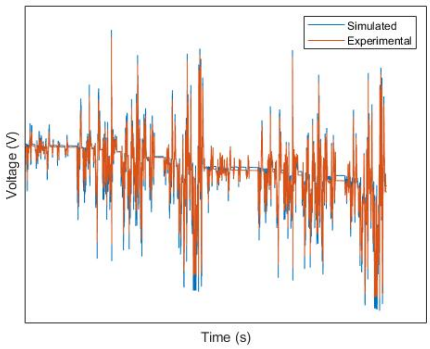

(a) CLTC simulated vs. experimental voltage comparison for cell level

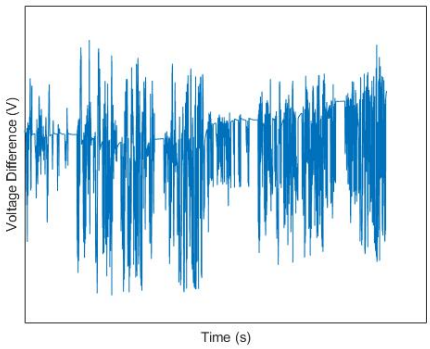

(b) CLTC cell level voltage difference between simulated and experimental

Fig. 4.2.3: CLTC cell level voltage results

4.2.4 EPA

The EPA drive cycle results were poorer than the previous cycle but were still acceptable as the RMSE value was calculated at 2.19×10^{-2} and had a maximum voltage difference of 0.09V.

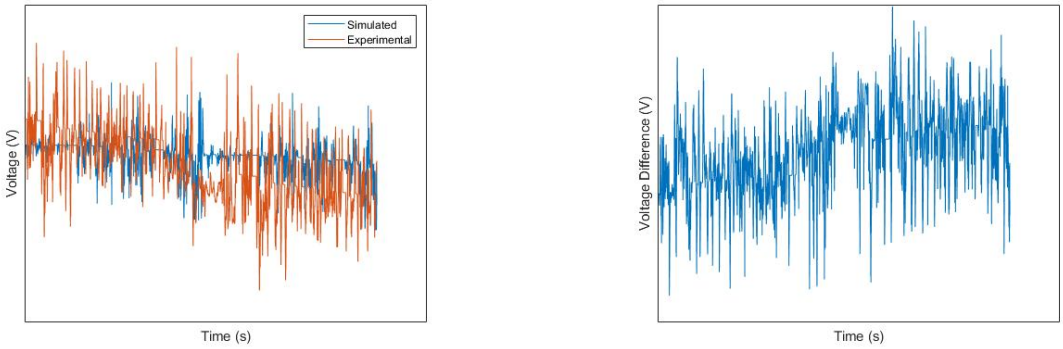

(a) EPA simulated vs. experimental voltage comparison for cell level

(b) EPA cell level voltage difference between simulated and experimental

Fig. 4.2.4: EPA cell level voltage results

4.2.5 NR Drive Cycle

Last but not least, the NR drive cycle was completed. This cycle has the greatest loading by far, and as such, the high C-rates are believed to be skewing the simulation's ability to describe the voltage conditions. The simulation does describe the voltage behavior well, as is evident from 4.2.5 but there is still room for improvement. The RMSE value is $4.62 \times 10^{-2} V$, and the maximum difference is $0.08 V$.

4.3 Cell Model Thermal Results

Here, the cell model thermal results are discussed for the WLTC, CLTC, EPA, and NR drive cycles, with their maximum and average temperatures discussed.

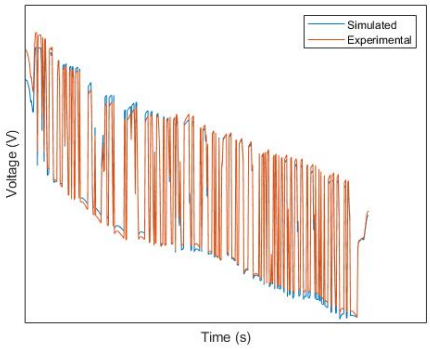

(a) NR simulated vs. experimental voltage comparison for cell level

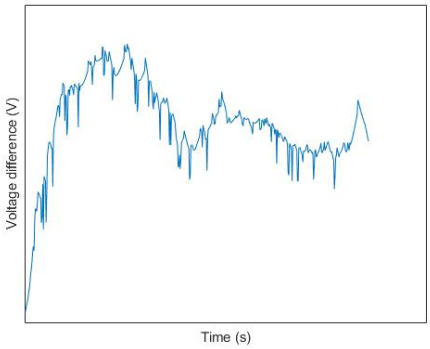

(b) NR cell level voltage difference between simulated and experimental

Fig. 4.2.5: NR voltage results

4.3.1 WLTC Thermal Results

The maximum and average temperature values of the cycle were recorded and are displayed over the entirety of the drive cycle in Fig. 4.3.1. Over the entire drive cycle, one can see that heat generation within the cell has a limited effect on the battery temperatures, with an average temperature increase of only 0.165 °C. The maximum temperature increase is of similar magnitude at 0.185 °C.

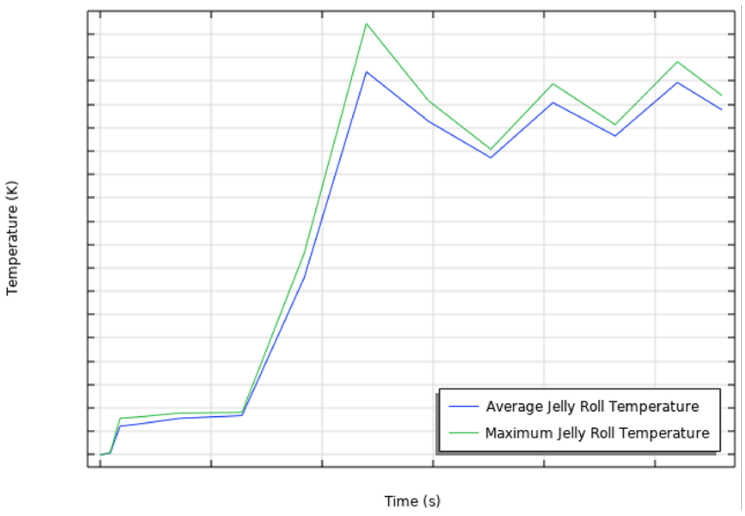

Fig. 4.3.1: WLTC cell temperature results

4.3.2 CLTC Thermal Results

The CLTC drive cycle thermal results are shown in Fig. 4.3.2. The profile starts with a decrease in temperature and ends with a final temperature increase of about 0.3 °C from the initial starting point. Although this is unintuitive, this endothermic behavior in the context of the reversible heat generation makes sense as the entropic terms of the heat generation have negative values at specific points of the charge status. These entropic terms create a negative heat generation if the current values are not high enough. This behavior again only shows a minor increase in temperature over the drive cycle. Also importantly, the difference between the maximum and average temperature of the battery is slight.

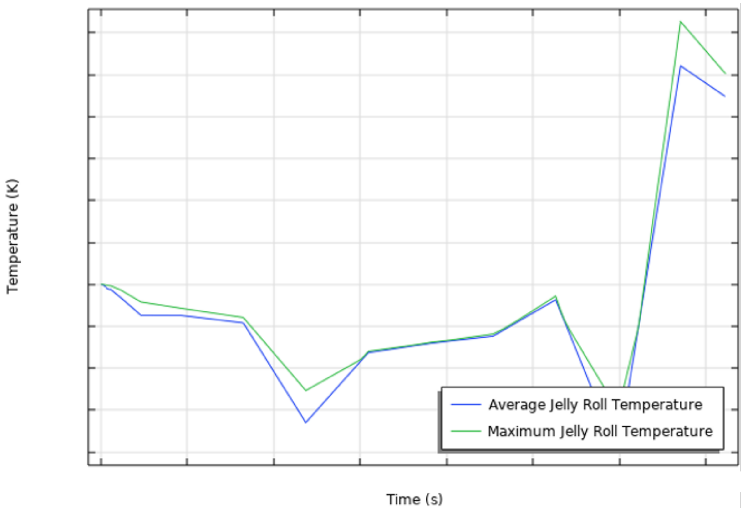

Fig. 4.3.2: CLTC cell temperature results

4.3.3 EPA Thermal Results

The thermal results from the EPA are apparent in Fig. 4.3.3. There is a spike at around 1100 seconds, where the currents are most prominent. Still, even with this significant increase, one can see that the magnitude of the temperature increase is 0.42 °C from the initial starting conditions. One is also able to see that once again, for the drive cycles that are not simulating racing conditions, such as the NR cycle, the maximum temperature differential is minimal, with the most significant difference

being at the peak of the heat generation seen at around 1100 seconds, where the maximum jelly roll temperature is 298.365 (K). This is only a 0.5 °C increase. As the currents within the drive cycle decrease over the latter half, the convective heat transfer is enough to return the battery temperature to a temperature closer to the ambient temperature.

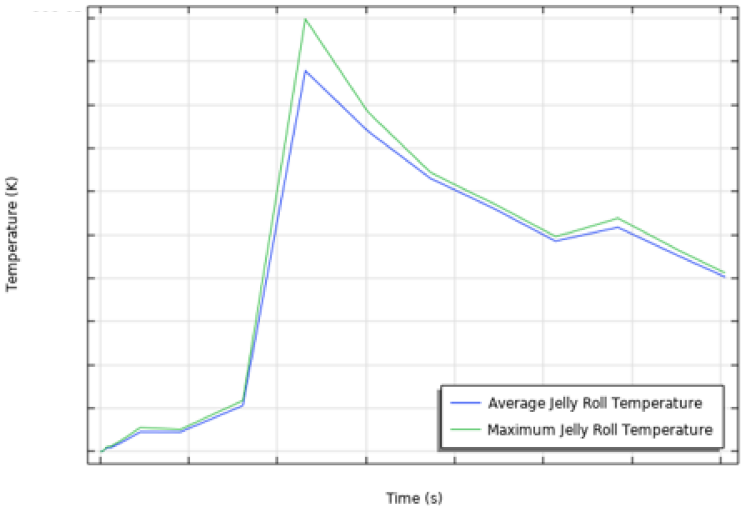

Fig. 4.3.3: EPA cell temperature results

4.3.4 NR Thermal Results

The NR results show a much larger temperature increase than the other drive cycles. This temperature difference is due to the magnitude difference in current rates between the CLTC, WLTC, EPA, and NR cycles. These cycles, respectively, have maximum C-rates of 0.6,0.6,0.8 C. These aforementioned cycles' C-rates contrasted with the NR cycle, which has a maximum C-rate of 8.8, are very low. The NR C-rates are correspondingly a whole magnitude difference larger than the other drive cycles, and their effects can be seen in the temperature plot observed in Fig. 4.3.4. The temperature magnitude differs hugely from the other drive cycles, with a temperature increase of 34 °C.

The average and maximum temperature difference also falls within an unacceptable range, with a temperature differential of around 5 °C. This temperature differential is not within the acceptable ranges for EVs and suggests that a thermal manage-

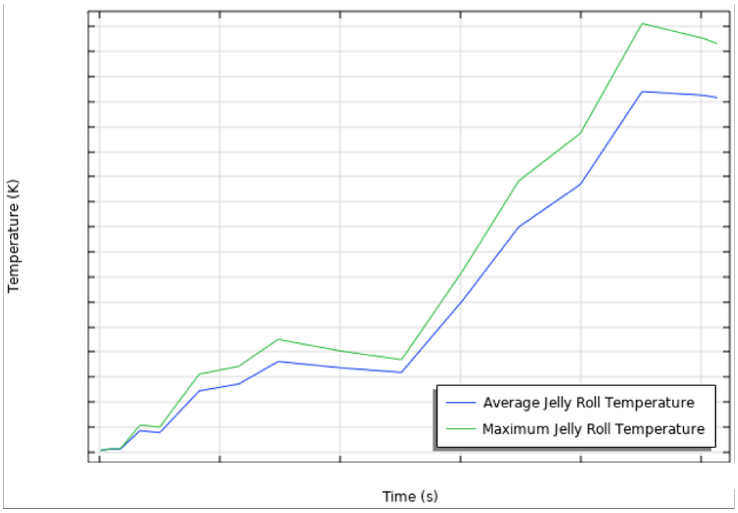

Fig. 4.3.4: NR cell temperature results

ment system's loading would undoubtedly need to be increased for these racing-like scenarios.

4.4 Modular Thermal Results

Looking now at the modular topology configuration, the drive cycle simulation for the thermal behavior started to approach a more realistic scenario of the topology of uses these batteries will face during driving. Before continuing with the discussion, there was a need for a numbering scheme because there are multiple cells at the module level. The subsequent figures label the different jelly roll temperatures as C(No). The cell number starts farthest from the plane of symmetry, and then the cell number increases as it moves towards the plane of symmetry. The same numbering system is used for the jelly rolls, where each jelly roll's number for a specific battery is increased as its location is closer to the plane of symmetry. In the case of the jelly roll, its classification is listed as J(no). For geometric clarification, the naming system is included in Fig. 4.4.1 shown below.

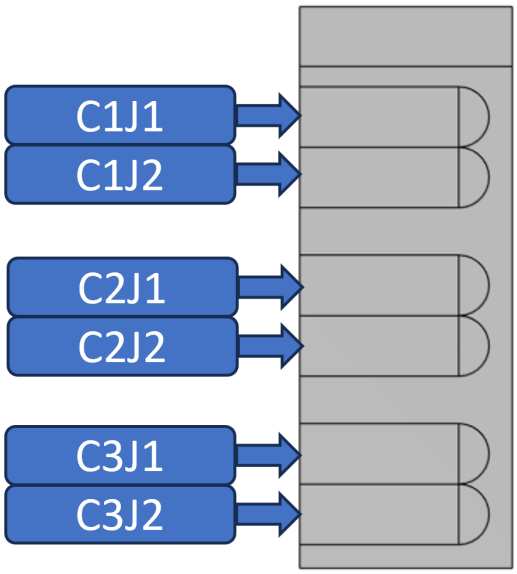

Fig. 4.4.1: Naming convention for the modular thermal results

4.4.1 WLTC Drive Cycle

Starting again with the WLTC cycle, the temperatures of the drive cycle are shown in Fig. 4.4.3. These results show that the temperature increase is more significant than the cell temperature alone, as the maximum temperature increases to 300.6 K, a 2.45-degree C increase from the initial condition. One can also see that the cells' temperatures diverge as the cycle progresses; however, this temperature difference is within 1 °C.

It can also be seen that the cell closest to the module's center $C3J2$ from Fig. 4.4.3 has the highest temperature increase at the end of the simulation. Interestingly, the cells in the module's center for the duration of the initial portion of the cycle have the most considerable temperature magnitude, as seen from $C2J2$ in Fig. 4.4.3.

4.4.2 CLTC Drive Cycle

Similarly to the WLTC cycle, the magnitude of the cell temperature increase intensified with the addition of more cells. Its overall increase is reduced in comparison with that of the WLTC cycle. Still, it had a very similar temperature increase, with

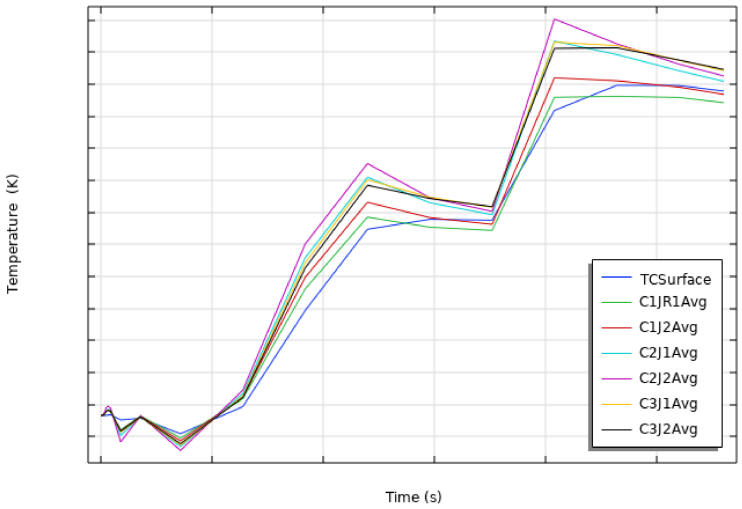

Fig. 4.4.2: WLTC drive cycle results

an average increase of around 2 °C, and the temperature spread of the cells across the module is tightly knit. This temperature spread was smaller than that of the WLTC cycle. This temperature increase displays that a BTMS should accompany the module behavior for regular use. It is proposed that the average temperatures would increase further with an increase in the cycle number. It is noted, however, that the time scale of the WLTC cycle is around 3500 s. This time scale is relatively close in time magnitude to around an hour of light driving. If the WLTC encapsulates the drivers' behavior, then the load on the BTMS system would be relatively small.

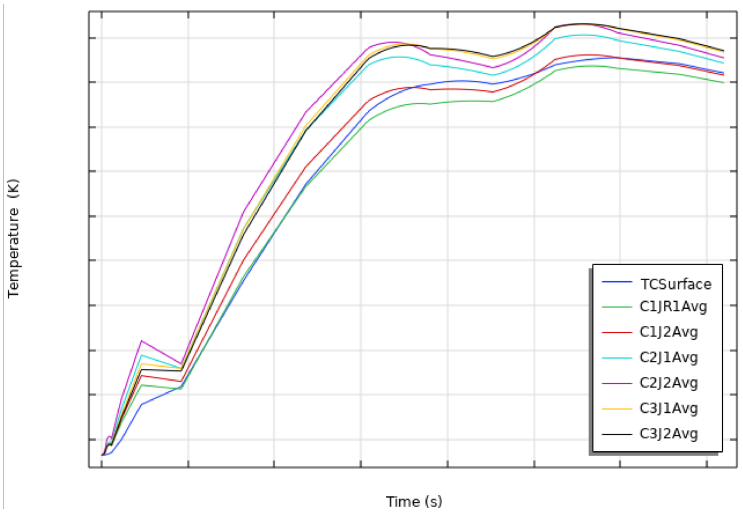

Fig. 4.4.3: CLTC drive cycle results

Once again, the cell behavior during the cycle has similar properties to the WLTC cycle. The cells in the center of the module for the initial half of the cycle are the highest, and then towards the end of the cycle, they start to converge with the cell in the center, finishing with the highest temperature.

4.4.3 EPA

Regarding the average temperatures for the EPA cycle, the average temperatures as shown in Fig. 4.4.4 increase more significantly than that of the individual cell. These more significant temperature differences are expected due to the cells' multiplicity. Its increase is again very similar, with a rise of 4.3 °C. The spread of the temperatures also follows the same trend as the others, diverging over the entire drive cycle and having the most significant differences near the end of the cycle. This differential from lowest to maximum is around 0.5 degrees C, which is acceptable in battery use.

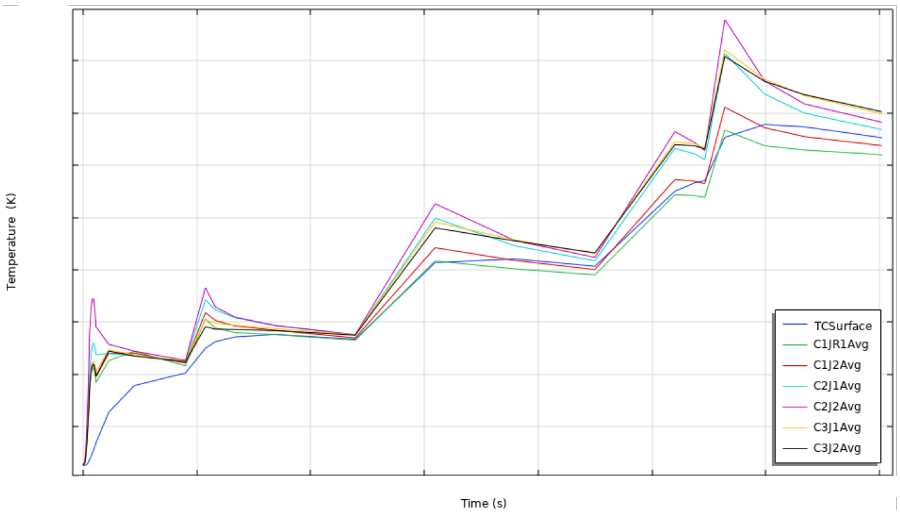

Fig. 4.4.4: EPA drive cycle results

The pattern of the WLTC, and CLTC drive cycle continues with the continues here with the EPA drive cycle. The cells in the center had the most significant initial temperature gradient, and their increase on average to be the hottest continued until the very end of the drive cycle, where the innermost jelly roll then became the maximum temperature.

4.4.4 NR

The NR cycle is the most demanding of all the cycles, with incredibly large C-rates and E-rates; due to this, it was expected that the temperature increase would be more extensive in magnitude than the previous drive cycles. However, the drive cycle is much shorter than that of the WLTC, CLTC, and EPA sections at a meager value of around 600 s, so it was possible that the temperature increase would not be as drastic as it was. The temperature distribution of the module can be seen from the image in 4.4.5.

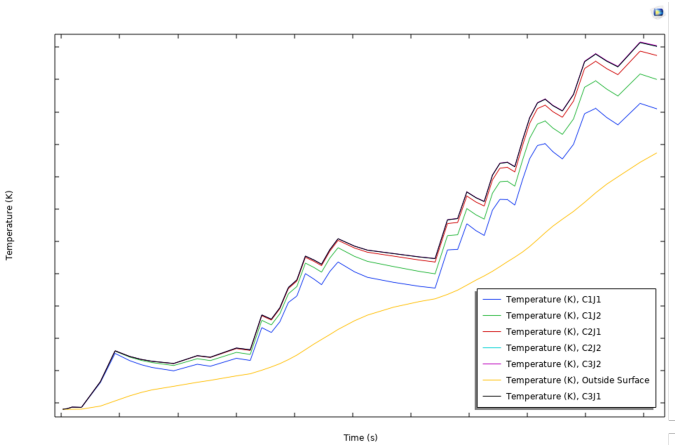

Fig. 4.4.5: NR drive cycle JR temperatures

The overall increase throughout the drive cycle was expected to be quite large due to the immense heat generation and the significant heat effects from one jelly roll. The hotspots of the module range closer to the center of the battery, with the highest temperature sections being directly adjacent to the batteries. This simulation calculated a final temperature increase of over 110 °C. This temperature seems unlikely and is likely due to the employed heat generation map technique. As the battery approaches temperatures exceeding the temperature domains of the heat generation maps, extrapolation must occur, leading to unrealistic heat generation. Due to this extrapolation, the temperature difference grew quite large, from their original starting temperatures and from each other. This behavior suggests that without the BTMS, this cycle could be detrimental to the lifecycle and safety of the battery, and as such, these racing-link driving conditions would need a BTMS.

CHAPTER 5

Conclusions and Recommendations

5.1 Conclusions

In conclusion, a 1D SPM model to estimate voltages was completed and tested using the HPPC curve 25°C ambient air conditions as its basis. Parameters for the 1D SPM simulation were estimated using a GA and used to generate voltage profiles that displayed accurate results to the behavior of a real-life cell. Although there were differences between the estimated HPPC and simulated HPPC voltage curves, these parameters effectively simulated the various driving cycles in the regions 95% SOC and 5% SOC, as was seen for the WLTC, CLTC, EPA, and NR cycles. The errors between the estimated voltages and experimental voltages were $9.65 \times 10^{-5}V$, $4.9 \times 10^{-3}V$, $2.19 \times 10^{-2}V$, and $4.62 \times 10^{-2}V$ respectively. These results show how well the GA can estimate the voltage behavior of the battery.

With these estimations, 2D heat generation maps were created to include the varying effects temperature had on the heat generation terms. With these heat maps, the behavior of the battery at cell and module temperatures was completed, and the behavior was analyzed. The thermal behavior of the WLTC, CLTC, EPA, and NR drive cycles was modeled and evaluated, with average temperature increases of 0.19°C, 0.3°C, and 0.4°C for the first three curves. The NR drive cycle had the most significant heat generation profile and the largest temperature increase. The results show that these parameter estimations show the cell level's expected thermal

behaviors. This expected thermal behavior was shown at the cellular level for the WLTC, EPA, CLTC, and EPA drive cycles. Areas of interest at the cellular level were identified.

The areas of thermal interest were also identified at the modular level for the CLTC, WLTC, EPA, and NR cycles. The temperature increase across the drive cycles is more significant in magnitude than that of their cellular results. The temperature spread of module cells was also small, which is beneficial for the batteries' use case. The maximum temperatures were also identified in each case, where the cell in the module's center unsurprisingly had the highest end temperature after the simulation. The heat map technique was also identified to be functional with cycles of lower C-rate and unsuitable for cycles that could push the temperatures of the batteries outside the expected temperature range for the heat map.

5.2 Recommendations

Areas of improvement for future research have multiple avenues. They will be divided into three categories.

- Simulation-based improvements
- GA Improvements
- 3D thermal model improvements

5.2.1 Simulation-based Improvements

The first area of improvement that is possible is to couple the thermal 3D simulations with the 1D simulations, such that, at every time step, the 1D electrochemical model is recalculated, and the heat generation terms can be more accurately simulated instead of the interpolation process that was carried out in this research. Another area of improvement is the heat generation terms within the 1D model; by including the concentration gradients to calculate the heat generation more closely, a more accurate representation of the battery can be achieved.

5.2.2 GA improvements

The generations could be run further for the GA improvement to achieve a more convergent RMSE value. Due to the nature of the GA approaching a local optimum, there remained a spread in the estimations of the parameters. In the author's belief, this spread could be reduced with the increase of the generation number and the number of GA attempts, but at the cost of the time. As written, the GA did not consider parallelization capabilities; with a rewrite of the methodology, more convergent results could be achieved simultaneously but with increased computational resources.

Within the 1D model, there are implicit assumptions on some of the values of the parameters that are well accepted; two of particular note are the Bruggeman coefficient and the charge transfer coefficient α used in the Butler-Volmer equation. These values were assumed to be 1.5 and 0.5, respectively. However, this may not be the case, and perhaps including these values within the GA estimation process could further improve the model's estimation properties.

One fundamental assumption in this context could also provide improvement: the assumption provided by equation 3.69. This assumption is not necessarily valid and may be incorrect to the best of the author's knowledge. The assumption changed to equation 5.1 is more comprehensive.

$$C_{batt} = min(C_{anode}, C_{cathode}) \tag{5.1}$$

This more comprehensive assumption allows either of the electrodes to be oversized, which is likely from a design perspective. Furthermore, a sensitivity analysis could have been completed before the start of the GA to ensure that the variables chosen have a non-negligible contribution to the simulation results.

5.2.3 3D Thermal Model Improvements

With some changes in assumptions at the 3D scale, further improvements could also be made. An overall thermal conductivity was provided; however, the thermal distribution could be enhanced with further fidelity of the material properties. The thermal

conductivities are not the only values that could be improved; an enhancement to the 3D model at every level (cell and module) could include radiation dissipation. The values for the emissivity and absorptivity of the surrounding BMS system were unknown and, as such, not included in the scope of this work. Finally, one further improvement could be made at the 3D level; with further cell fidelity, the tab information and the bus bar parts could be included in the simulation to evaluate potential hot spots of the battery due to the connection with the CAN bus. One particular area of interest could also be including stress and aging effects within the 1D model, including the temperature effects.

REFERENCES

[1] L. Yu and Y. Li, "A flexible-possibilistic stochastic programming method for planning municipal-scale energy system through introducing renewable energies and electric vehicles," *Journal of Cleaner Production*, vol. 207, pp. 772–787, 2019.

[2] N. Cunningham, "Canada announces plans to phase out ice vehicles by 2035," Jul 2021.

[3] D. Xu, Y. Zhang, B. Chen, J. Bai, G. Liu, and B. Zhang, "Identifying the critical paths and sectors for carbon transfers driven by global consumption in 2015," *Applied Energy*, vol. 306, p. 118137, 2022.

[4] S. Amjad, S. Neelakrishnan, and R. Rudramoorthy, "Review of design considerations and technological challenges for successful development and deployment of plug-in hybrid electric vehicles," *Renewable and Sustainable Energy Reviews*, vol. 14, no. 3, pp. 1104–1110, 2010.

[5] A. Jacob, B. Ashok, R. Vignesh, S. Balusamy, and A. Alagumalai, "Nox and pm trade-off in ic engines," in *NOx Emission Control Technologies in Stationary and Automotive Internal Combustion Engines*, pp. 69–93, Elsevier, 2022.

[6] Z. Rao and S. Wang, "A review of power battery thermal energy management," *Renewable and Sustainable Energy Reviews*, vol. 15, no. 9, pp. 4554–4571, 2011.

[7] Y. Lyu, A. Siddique, S. H. Majid, M. Biglarbegian, S. Gadsden, and S. Mah-

mud, "Electric vehicle battery thermal management system with thermoelectric cooling," *Energy Reports*, vol. 5, pp. 822–827, 2019.

[8] L. Xie, C. Tang, Z. Bi, M. Song, Y. Fan, C. Yan, X. Li, F. Su, Q. Zhang, and C. Chen, "Hard carbon anodes for next-generation li-ion batteries: review and perspective," *Advanced Energy Materials*, vol. 11, no. 38, p. 2101650, 2021.

[9] Y. Kang, C. Deng, Y. Chen, X. Liu, Z. Liang, T. Li, Q. Hu, and Y. Zhao, "Binder-free electrodes and their application for li-ion batteries," *Nanoscale Research Letters*, vol. 15, pp. 1–19, 2020.

[10] B. Xu, Y. Liu, J. Tian, X. Ma, Q. Ping, B. Wang, and Y. Xia, "Ni3 (bo3) 2 as anode material with high capacity and excellent rate performance for sodium-ion batteries," *Chemical Engineering Journal*, vol. 363, pp. 285–291, 2019.

[11] Y. Wang, C. Liu, R. Pan, and Z. Chen, "Modeling and state-of-charge prediction of lithium-ion battery and ultracapacitor hybrids with a co-estimator," *Energy*, vol. 121, pp. 739–750, 2017.

[12] F. Baronti, G. Fantechi, R. Roncella, R. Saletti, and P. Terreni, "Hardware building blocks of a hierarchical battery management system for a fuel cell hev," in *IECON 2012-38th Annual Conference on IEEE Industrial Electronics Society*, pp. 4041–4047, IEEE, 2012.

[13] J. Jaguemont, L. Boulon, and Y. Dubé, "Characterization and modeling of a hybrid-electric-vehicle lithium-ion battery pack at low temperatures," *IEEE Transactions on Vehicular Technology*, vol. 65, no. 1, pp. 1–14, 2015.

[14] D. Burow, K. Sergeeva, S. Calles, K. Schorb, A. Boerger, C. Roth, and P. Heitjans, "Inhomogeneous degradation of graphite anodes in automotive lithium ion batteries under low-temperature pulse cycling conditions," *Journal of Power Sources*, vol. 307, pp. 806–814, 2016.

[15] Y. Zhang, C.-Y. Wang, and X. Tang, "Cycling degradation of an automotive

lifepo4 lithium-ion battery," *Journal of power sources*, vol. 196, no. 3, pp. 1513–1520, 2011.

[16] J. Kim, J. Oh, and H. Lee, "Review on battery thermal management system for electric vehicles," *Applied thermal engineering*, vol. 149, pp. 192–212, 2019.

[17] P. R. Tete, M. M. Gupta, and S. S. Joshi, "Developments in battery thermal management systems for electric vehicles: A technical review," *Journal of Energy Storage*, vol. 35, p. 102255, 2021.

[18] H. Kim and K. G. Shin, "Desa: Dependable, efficient, scalable architecture for management of large-scale batteries," *IEEE Transactions on Industrial Informatics*, vol. 8, no. 2, pp. 406–417, 2011.

[19] A. H. Akinlabi and D. Solyali, "Configuration, design, and optimization of air-cooled battery thermal management system for electric vehicles: A review," *Renewable and Sustainable Energy Reviews*, vol. 125, p. 109815, 2020.

[20] K. See, G. Wang, Y. Zhang, Y. Wang, L. Meng, X. Gu, N. Zhang, K. Lim, L. Zhao, and B. Xie, "Critical review and functional safety of a battery management system for large-scale lithium-ion battery pack technologies," *International Journal of Coal Science & Technology*, vol. 9, no. 1, p. 36, 2022.

[21] L. Situ, "Electric vehicle development: the past, present & future," in *2009 3rd International Conference on Power Electronics Systems and Applications (PESA)*, pp. 1–3, IEEE, 2009.

[22] M. Morimoto, "Which is the first electric vehicle?," *Electrical Engineering in Japan*, vol. 192, no. 2, pp. 31–38, 2015.

[23] E. H. Wakefield, *History of the electric automobile: Hybrid electric vehicles*, vol. 187. SAE International, 1998.

[24] W. Zhuang, S. Li, X. Zhang, D. Kum, Z. Song, G. Yin, and F. Ju, "A survey of powertrain configuration studies on hybrid electric vehicles," *Applied Energy*, vol. 262, p. 114553, 2020.

[25] K. Chau and C. C. Chan, "Emerging energy-efficient technologies for hybrid electric vehicles," *Proceedings of the IEEE*, vol. 95, no. 4, pp. 821–835, 2007.

[26] J. Albers, E. Meissner, and S. Shirazi, "Lead-acid batteries in micro-hybrid vehicles," *Journal of Power Sources*, vol. 196, no. 8, pp. 3993–4002, 2011.

[27] Y. Chen, *New Energy Vehicle Powertrain Technologies and Applications*. Springer Nature, 2023.

[28] Z. Li, A. Khajepour, and J. Song, "A comprehensive review of the key technologies for pure electric vehicles," *Energy*, vol. 182, pp. 824–839, 2019.

[29] K. Erhan and E. Özdemir, "Prototype production and comparative analysis of high-speed flywheel energy storage systems during regenerative braking in hybrid and electric vehicles," *Journal of Energy Storage*, vol. 43, p. 103237, 2021.

[30] A. Schäfer, J. B. Heywood, and M. A. Weiss, "Future fuel cell and internal combustion engine automobile technologies: A 25-year life cycle and fleet impact assessment," *Energy*, vol. 31, no. 12, pp. 2064–2087, 2006.

[31] S. Mekhilef, R. Saidur, and A. Safari, "Comparative study of different fuel cell technologies," *Renewable and Sustainable Energy Reviews*, vol. 16, no. 1, pp. 981–989, 2012.

[32] S. Sharma, A. K. Panwar, and M. Tripathi, "Storage technologies for electric vehicles," *Journal of Traffic and Transportation Engineering (English Edition)*, vol. 7, no. 3, pp. 340–361, 2020. Special Issue: Clean Alternative Fuels for Transport Vehicles.

[33] M. İnci, M. Büyük, M. H. Demir, and G. İlbey, "A review and research on fuel cell electric vehicles: Topologies, power electronic converters, energy management methods, technical challenges, marketing and future aspects," *Renewable and Sustainable Energy Reviews*, vol. 137, p. 110648, 2021.

[34] K. K. Kar, *Handbook of nanocomposite supercapacitor materials II*, vol. 302. Springer, 2020.

[35] M. Horn, J. MacLeod, M. Liu, J. Webb, and N. Motta, "Supercapacitors: A new source of power for electric cars?," *Economic Analysis and Policy*, vol. 61, pp. 93–103, 2019. Special issue on: Future of transport.

[36] S. Karthikeyan, B. Narenthiran, A. Sivanantham, L. D. Bhatlu, and T. Maridurai, "Supercapacitor: Evolution and review," *Materials Today: Proceedings*, vol. 46, pp. 3984–3988, 2021.

[37] A. Cultura and Z. M. Salameh, "Modeling, evaluation and simulation of a supercapacitor module for energy storage application," in *Proceedings of the International Conference on Computer Information Systems and Industrial Applications*, pp. 876–882, Atlantis Press, 2015.

[38] M. Hashemi, M. S. Rahmanifar, M. F. El-Kady, A. Noori, M. F. Mousavi, and R. B. Kaner, "The use of an electrocatalytic redox electrolyte for pushing the energy density boundary of a flexible polyaniline electrode to a new limit," *Nano energy*, vol. 44, pp. 489–498, 2018.

[39] W. Raza, F. Ali, N. Raza, Y. Luo, K.-H. Kim, J. Yang, S. Kumar, A. Mehmood, and E. E. Kwon, "Recent advancements in supercapacitor technology," *Nano Energy*, vol. 52, pp. 441–473, 2018.

[40] S. Verma, S. Mishra, A. Gaur, S. Chowdhury, S. Mohapatra, G. Dwivedi, and P. Verma, "A comprehensive review on energy storage in hybrid electric vehicle," *Journal of Traffic and Transportation Engineering (English Edition)*, vol. 8, no. 5, pp. 621–637, 2021.

[41] M. N. Gayathri, "Energy storage systems for electric vehicles," *Energy Storage for Modern Power System Operations*, pp. 79–104, 2021.

[42] A. G. Olabi, T. Wilberforce, M. A. Abdelkareem, and M. Ramadan, "Critical

review of flywheel energy storage system," *Energies*, vol. 14, no. 8, p. 2159, 2021.

[43] M. Krichen, Y. Basheer, S. M. Qaisar, and A. Waqar, "A survey on energy storage: Techniques and challenges," *Energies*, vol. 16, no. 5, p. 2271, 2023.

[44] D. S. Cardoso, P. O. Fael, and A. Espírito-Santo, "A review of micro and mild hybrid systems," *Energy reports*, vol. 6, pp. 385–390, 2020.

[45] W. Enang and C. Bannister, "Modelling and control of hybrid electric vehicles (a comprehensive review)," *Renewable and Sustainable Energy Reviews*, vol. 74, pp. 1210–1239, 2017.

[46] K. Ç. Bayindir, M. A. Gözüküçük, and A. Teke, "A comprehensive overview of hybrid electric vehicle: Powertrain configurations, powertrain control techniques and electronic control units," *Energy conversion and Management*, vol. 52, no. 2, pp. 1305–1313, 2011.

[47] A. Sciarretta, M. Back, and L. Guzzella, "Optimal control of parallel hybrid electric vehicles," *IEEE Transactions on control systems technology*, vol. 12, no. 3, pp. 352–363, 2004.

[48] N. N. Mustafi, "An overview of hybrid electric vehicle technology," *Engines and Fuels for Future Transport*, pp. 73–102, 2022.

[49] M. Ehsani, Y. Gao, and J. M. Miller, "Hybrid electric vehicles: Architecture and motor drives," *Proceedings of the IEEE*, vol. 95, no. 4, pp. 719–728, 2007.

[50] Q. Hou, N. Zhang, E. Du, M. Miao, F. Peng, and C. Kang, "Probabilistic duck curve in high pv penetration power system: Concept, modeling, and empirical analysis in china," *Applied Energy*, vol. 242, pp. 205–215, 2019.

[51] D. Dees, E. Gunen, D. Abraham, A. Jansen, and J. Prakash, "Electrochemical modeling of lithium-ion positive electrodes during hybrid pulse power characterization tests," *Journal of the Electrochemical Society*, vol. 155, no. 8, p. A603, 2008.

[52] P. J. Bugryniec, J. N. Davidson, D. J. Cumming, and S. F. Brown, "Pursuing safer batteries: thermal abuse of lifepo4 cells," *Journal of Power Sources*, vol. 414, pp. 557–568, 2019.

[53] Y. Feng, L. Zhou, H. Ma, Z. Wu, Q. Zhao, H. Li, K. Zhang, and J. Chen, "Challenges and advances in wide-temperature rechargeable lithium batteries," *Energy & Environmental Science*, vol. 15, no. 5, pp. 1711–1759, 2022.

[54] Y. Ji, Y. Zhang, and C.-Y. Wang, "Li-ion cell operation at low temperatures," *Journal of The Electrochemical Society*, vol. 160, no. 4, p. A636, 2013.

[55] J. Hou, M. Yang, D. Wang, and J. Zhang, "Fundamentals and challenges of lithium ion batteries at temperatures between- 40 and 60° c," *Advanced Energy Materials*, vol. 10, no. 18, p. 1904152, 2020.

[56] J. Tian, Y. Wang, and Z. Chen, "An improved single particle model for lithium-ion batteries based on main stress factor compensation," *Journal of Cleaner Production*, vol. 278, p. 123456, 2021.

[57] F. Brosa Planella, W. Ai, A. M. Boyce, A. Ghosh, I. Korotkin, S. Sahu, V. Sulzer, R. Timms, T. G. Tranter, M. Zyskin, S. J. Cooper, J. Edge, J. M. Foster, M. Marinescu, B. Wu, and G. Richardson, "A continuum of physics-based lithium-ion battery models reviewed," *Progress in Energy*, vol. 4, no. 4, p. 042003, 2022.

[58] A. M. Bizeray, J.-H. Kim, S. R. Duncan, and D. A. Howey, "Identifiability and parameter estimation of the single particle lithium-ion battery model," *IEEE Transactions on Control Systems Technology*, vol. 27, no. 5, pp. 1862–1877, 2018.

[59] J. Sun and J. Kainz, "Optimization of hybrid pulse power characterization profile for equivalent circuit model parameter identification of li-ion battery based on taguchi method," *Journal of Energy Storage*, vol. 70, p. 108034, 2023.

[60] M. Wakihara, "Recent developments in lithium ion batteries," *Materials Science and Engineering: R: Reports*, vol. 33, no. 4, pp. 109–134, 2001.

[61] S. Manzetti and F. Mariasiu, "Electric vehicle battery technologies: From present state to future systems," *Renewable and Sustainable Energy Reviews*, vol. 51, pp. 1004–1012, 2015.

[62] Q. Wang, B. Jiang, B. Li, and Y. Yan, "A critical review of thermal management models and solutions of lithium-ion batteries for the development of pure electric vehicles," *Renewable and Sustainable Energy Reviews*, vol. 64, pp. 106–128, 2016.

[63] C. Curry, "Lithium-ion battery costs and market," *Bloomberg New Energy Finance*, vol. 5, pp. 4–6, 2017.

[64] N.A, "Stellantis and lg energy solution to invest over 5 billion cad in joint venture for first large scale lithium-ion battery production plant in canada." `https://www.stellantis.com/en/news/press-releases/2022/march/stellantis-and-lg-energy-solution-to-invest-over-5-billion-cad-in-joint-venture-for-first-large-scale-lithium-Ion-battery-production-plant-in-canada`.

[65] P. A. Eisenstein, "Gm hikes spending $35 billion on evs, battery plants, self-driving and fuel cells," Oct 2022.

[66] NCR18650PF, "Ncr18650pf." `https://na.industrial.panasonic.com/products/batteries/rechargeable-batteries/lineup/lithium-ion/series/90729/model/90730`.

[67] E. J. Dufek, T. R. Tanim, B.-R. Chen, and S. Kim, "Battery calendar aging and machine learning," *Joule*, vol. 6, no. 7, pp. 1363–1367, 2022.

[68] W. Pantoja, J. A. Perez-Taborda, and A. Avila, "Tug-of-war in the selection of materials for battery technologies," *Batteries*, vol. 8, no. 9, p. 105, 2022.

[69] M. E. V. Team, "A guide to understanding battery specifications," *Academia. edu*, 2008.

[70] H. Rubenbauer and S. Henninger, "Definitions and reference values for battery systems in electrical power grids," *Journal of Energy Storage*, vol. 12, pp. 87–107, 2017.

[71] Q. Ouyang and J. Chen, *Advanced Model-Based Charging Control for Lithium-Ion Batteries*. Springer, 2023.

[72] F. Cheng, W. Zhang, D. Qin, S. Sun, Y. Xu, Q. Li, C. Fang, J. Han, and Y. Huang, "Reinterpreting the correlation between cycling stability of ni-rich layered oxide cathode and the charging cut-off voltage in li-ion batteries," *Nano Energy*, p. 108699, 2023.

[73] S. Yang, C. Zhang, J. Jiang, W. Zhang, L. Zhang, and Y. Wang, "Review on state-of-health of lithium-ion batteries: Characterizations, estimations and applications," *Journal of Cleaner Production*, vol. 314, p. 128015, 2021.

[74] P. Kollmeyer, "Panasonic 18650pf li-ion battery data," *Mendeley Data*, vol. 1, no. 2018, 2018.

[75] M. Winter and R. J. Brodd, "What are batteries, fuel cells, and supercapacitors?," *Chemical reviews*, vol. 104, no. 10, pp. 4245–4270, 2004.

[76] I. Hadjipaschalis, A. Poullikkas, and V. Efthimiou, "Overview of current and future energy storage technologies for electric power applications," *Renewable and sustainable energy reviews*, vol. 13, no. 6-7, pp. 1513–1522, 2009.

[77] A. A. Habib, S. Motakabber, and M. I. Ibrahimy, "A comparative study of electrochemical battery for electric vehicles applications," in *2019 IEEE International Conference on Power, Electrical, and Electronics and Industrial Applications (PEEIACON)*, pp. 43–47, IEEE, 2019.

[78] R. C. Massé, C. Liu, Y. Li, L. Mai, and G. Cao, "Energy storage through intercalation reactions: electrodes for rechargeable batteries," *National Science Review*, vol. 4, no. 1, pp. 26–53, 2017.

[79] Z. J. Zhang and P. Ramadass, "Lithium-ion battery systems and technology," in *Batteries for Sustainability: Selected Entries from the Encyclopedia of Sustainability Science and Technology*, pp. 319–357, Springer, 2012.

[80] B. Dunn, H. Kamath, and J.-M. Tarascon, "Electrical energy storage for the grid: a battery of choices," *Science*, vol. 334, no. 6058, pp. 928–935, 2011.

[81] A. Mauger and C. Julien, "Critical review on lithium-ion batteries: are they safe? sustainable?," *Ionics*, vol. 23, pp. 1933–1947, 2017.

[82] C. Costa, E. Lizundia, and S. Lanceros-Méndez, "Polymers for advanced lithium-ion batteries: State of the art and future needs on polymers for the different battery components," *Progress in Energy and Combustion Science*, vol. 79, p. 100846, 2020.

[83] H.-H. Chang, T.-H. Ho, and Y.-S. Su, "Graphene-enhanced battery components in rechargeable lithium-ion and lithium metal batteries," *C*, vol. 7, no. 3, p. 65, 2021.

[84] G. L. Plett, *Battery management systems, Volume I: Battery modeling*. Artech House, 2015.

[85] P. Zhu, D. Gastol, J. Marshall, R. Sommerville, V. Goodship, and E. Kendrick, "A review of current collectors for lithium-ion batteries," *Journal of Power Sources*, vol. 485, p. 229321, 2021.

[86] H. Zhang, Y. Yang, D. Ren, L. Wang, and X. He, "Graphite as anode materials: Fundamental mechanism, recent progress and advances," *Energy Storage Materials*, vol. 36, pp. 147–170, 2021.

[87] A. R. Armstrong, C. Lyness, P. M. Panchmatia, M. S. Islam, and P. G. Bruce, "The lithium intercalation process in the low-voltage lithium battery anode li1+ x v1- x o2," *Nature materials*, vol. 10, no. 3, pp. 223–229, 2011.

[88] N. A. Kaskhedikar and J. Maier, "Lithium storage in carbon nanostructures," *Advanced Materials*, vol. 21, no. 25-26, pp. 2664–2680, 2009.

[89] P. Luo, C. Zheng, J. He, X. Tu, W. Sun, H. Pan, Y. Zhou, X. Rui, B. Zhang, and K. Huang, "Structural engineering in graphite-based metal-ion batteries," *Advanced Functional Materials*, vol. 32, no. 9, p. 2107277, 2022.

[90] I. El Hajj, L. Speyer, S. Cahen, P. Lagrange, G. Medjahdi, and C. Hérold, "Crystal structure of first stage strontium-graphite intercalation compound," *Carbon*, vol. 168, pp. 732–736, 2020.

[91] J. H. Xu, D. E. Turney, A. L. Jadhav, and R. J. Messinger, "Effects of graphite structure and ion transport on the electrochemical properties of rechargeable aluminum–graphite batteries," *ACS Applied Energy Materials*, vol. 2, no. 11, pp. 7799–7810, 2019.

[92] S. Glazier, J. Li, A. Louli, J. Allen, and J. Dahn, "An analysis of artificial and natural graphite in lithium ion pouch cells using ultra-high precision coulometry, isothermal microcalorimetry, gas evolution, long term cycling and pressure measurements," *Journal of The Electrochemical Society*, vol. 164, no. 14, p. A3545, 2017.

[93] Z. Jin, Z. Cui, X. Long, M. Millan, G. Yuan, Z. Dong, Y. Cong, J. Zhang, Y. Li, and X. Li, "Understanding the correlation between microstructure and electrochemical performance of hybridized pitch cokes for lithium-ion battery through tailoring their evolutional structures from ordered soft carbon to disordered hard carbon," *Journal of Alloys and Compounds*, vol. 887, p. 161357, 2021.

[94] F. Xie, Z. Xu, A. C. Jensen, H. Au, Y. Lu, V. Araullo-Peters, A. J. Drew, Y.-S. Hu, and M.-M. Titirici, "Hard–soft carbon composite anodes with synergistic sodium storage performance," *Advanced functional materials*, vol. 29, no. 24, p. 1901072, 2019.

[95] Y. Li, Y.-S. Hu, H. Li, L. Chen, and X. Huang, "A superior low-cost amorphous carbon anode made from pitch and lignin for sodium-ion batteries," *Journal of Materials Chemistry A*, vol. 4, no. 1, pp. 96–104, 2016.

[96] A. Franco Gonzalez, N.-H. Yang, and R.-S. Liu, "Silicon anode design for lithium-ion batteries: progress and perspectives," *The Journal of Physical Chemistry C*, vol. 121, no. 50, pp. 27775–27787, 2017.

[97] Y. Jin, B. Zhu, Z. Lu, N. Liu, and J. Zhu, "Challenges and recent progress in the development of si anodes for lithium-ion battery," *Advanced Energy Materials*, vol. 7, no. 23, p. 1700715, 2017.

[98] L. Sun, Y. Liu, R. Shao, J. Wu, R. Jiang, and Z. Jin, "Recent progress and future perspective on practical silicon anode-based lithium ion batteries," *Energy Storage Materials*, vol. 46, pp. 482–502, 2022.

[99] C. Xu, B. Wang, H. Luo, P. Jing, X. Zhang, Q. Wang, Y. Zhang, and H. Wu, "Embedding silicon in pinecone-derived porous carbon as a high-performance anode for lithium-ion batteries," *ChemElectroChem*, vol. 7, no. 13, pp. 2889–2895, 2020.

[100] J. Wang, W. Huang, Y. S. Kim, Y. K. Jeong, S. C. Kim, J. Heo, H. K. Lee, B. Liu, J. Nah, and Y. Cui, "Scalable synthesis of nanoporous silicon microparticles for highly cyclable lithium-ion batteries," *Nano Research*, vol. 13, pp. 1558–1563, 2020.

[101] B. Li, X. Gao, J. Li, and C. Yuan, "Life cycle environmental impact of high-capacity lithium ion battery with silicon nanowires anode for electric vehicles," *Environmental science & technology*, vol. 48, no. 5, pp. 3047–3055, 2014.

[102] Z. Zhang, H. Wang, M. Cheng, Y. He, X. Han, L. Luo, P. Su, W. Huang, J. Wang, C. Li, Z. Zhu, Q. Zhang, and S. Chen, "Confining invasion directions of li+ to achieve efficient si anode material for lithium-ion batteries," *Energy Storage Materials*, vol. 42, pp. 231–239, 2021.

[103] E. Antolini, "Licoo2: formation, structure, lithium and oxygen nonstoichiometry, electrochemical behaviour and transport properties," *Solid state ionics*, vol. 170, no. 3-4, pp. 159–171, 2004.

[104] K. Mizushima, P. Jones, P. Wiseman, and J. B. Goodenough, "Lixcoo2 (0¡ x¡-1):

A new cathode material for batteries of high energy density," *Materials Research Bulletin*, vol. 15, no. 6, pp. 783–789, 1980.

[105] Y. Nishi, "Lithium ion secondary batteries; past 10 years and the future," *Journal of Power Sources*, vol. 100, no. 1-2, pp. 101–106, 2001.

[106] L. Hu, S. Zhang, and Z. Zhang, "Rechargeable batteries: materials, technologies and new trends," *Green Energy Technol*, 2012.

[107] K. Zaghib, C. Julien, and J. Prakash, "New trends in intercalation compounds for energy storage and conversion: Proceedings of the international symposium," The Electrochemical Society, 2003.

[108] S. Passerini and B. Scrosati, "Lithium and lithium-ion batteries: challenges and prospects," *The Electrochemical Society Interface*, vol. 25, no. 3, p. 85, 2016.

[109] Y. Takahashi, S. Tode, A. Kinoshita, H. Fujimoto, I. Nakane, and S. Fujitani, "Development of lithium-ion batteries with a licoo2 cathode toward high capacity by elevating charging potential," *Journal of the electrochemical society*, vol. 155, no. 7, p. A537, 2008.

[110] M. S. Whittingham, "Lithium batteries and cathode materials," *Chemical reviews*, vol. 104, no. 10, pp. 4271–4302, 2004.

[111] Y. Shao-Horn, L. Croguennec, C. Delmas, E. C. Nelson, and M. A. O'Keefe, "Atomic resolution of lithium ions in licoo2," *Nature materials*, vol. 2, no. 7, pp. 464–467, 2003.

[112] C. M. Julien, A. Mauger, K. Zaghib, and H. Groult, "Comparative issues of cathode materials for li-ion batteries," *Inorganics*, vol. 2, no. 1, pp. 132–154, 2014.

[113] A. R. Armstrong and P. G. Bruce, "Synthesis of layered limno2 as an electrode for rechargeable lithium batteries," *Nature*, vol. 381, no. 6582, pp. 499–500, 1996.

[114] R. Korthauer, *Lithium-ion batteries: basics and applications*. Springer, 2018.

[115] P. Guan, L. Zhou, Z. Yu, Y. Sun, Y. Liu, F. Wu, Y. Jiang, and D. Chu, "Recent progress of surface coating on cathode materials for high-performance lithium-ion batteries," *Journal of Energy Chemistry*, vol. 43, pp. 220–235, 2020.

[116] L. Yunjian, L. Xinhai, G. Huajun, W. Zhixing, H. Qiyang, P. Wenjie, and Y. Yong, "Electrochemical performance and capacity fading reason of limn2o4/graphite batteries stored at room temperature," *Journal of Power Sources*, vol. 189, no. 1, pp. 721–725, 2009.

[117] H. A. Tariq, J. J. Abraham, R. A. Shakoor, S. Al-Qaradawi, M. R. Abdul Karim, and U. Chaudhry, "Synthesis of lithium manganese oxide nanocomposites using microwave-assisted chemical precipitation technique and their performance evaluation in lithium-ion batteries," *Energy Storage*, vol. 2, no. 6, p. e202, 2020.

[118] B. E. Murdock, K. E. Toghill, and N. Tapia-Ruiz, "A perspective on the sustainability of cathode materials used in lithium-ion batteries," *Advanced Energy Materials*, vol. 11, no. 39, p. 2102028, 2021.

[119] G. Kucinskis, G. Bajars, and J. Kleperis, "Graphene in lithium ion battery cathode materials: A review," *Journal of Power Sources*, vol. 240, pp. 66–79, 2013.

[120] A. Manthiram, "An outlook on lithium ion battery technology," *ACS central science*, vol. 3, no. 10, pp. 1063–1069, 2017.

[121] P. P. Prosini, M. Lisi, D. Zane, and M. Pasquali, "Determination of the chemical diffusion coefficient of lithium in lifepo4," *Solid state ionics*, vol. 148, no. 1-2, pp. 45–51, 2002.

[122] K. Dokko, M. Mohamedi, Y. Fujita, T. Itoh, M. Nishizawa, M. Umeda, and I. Uchida, "Kinetic characterization of single particles of licoo2 by ac impedance and potential step methods," *Journal of the Electrochemical Society*, vol. 148, no. 5, p. A422, 2001.

[123] F. Cao and J. Prakash, "A comparative electrochemical study of limn2o4 spinel thin-film and porous laminate," *Electrochimica Acta*, vol. 47, no. 10, pp. 1607–1613, 2002.

[124] F. Astuti, V. L. Maghfirohtuzzoimah, S. H. Intifadhah, P. Az-Zahra, R. Arifin, W. Klysubun, M. Zainuri, and Darminto, "Local structure and electronic structure of lifepo4 as a cathode for lithium-ion batteries," in *Journal of Physics: Conference Series*, vol. 1951, p. 012007, IOP Publishing, 2021.

[125] L. Wang, B. Chen, J. Ma, G. Cui, and L. Chen, "Reviving lithium cobalt oxide-based lithium secondary batteries-toward a higher energy density," *Chemical Society Reviews*, vol. 47, no. 17, pp. 6505–6602, 2018.

[126] K. Xu, "Nonaqueous liquid electrolytes for lithium-based rechargeable batteries," *Chemical reviews*, vol. 104, no. 10, pp. 4303–4418, 2004.

[127] J. Hassoun and B. Scrosati, "Advances in anode and electrolyte materials for the progress of lithium-ion and beyond lithium-ion batteries," *Journal of The Electrochemical Society*, vol. 162, no. 14, p. A2582, 2015.

[128] D. Abraham, M. Furczon, S.-H. Kang, D. Dees, and A. Jansen, "Effect of electrolyte composition on initial cycling and impedance characteristics of lithium-ion cells," *Journal of Power Sources*, vol. 180, no. 1, pp. 612–620, 2008.

[129] D. Andre, S.-J. Kim, P. Lamp, S. F. Lux, F. Maglia, O. Paschos, and B. Stiaszny, "Future generations of cathode materials: an automotive industry perspective," *Journal of Materials Chemistry A*, vol. 3, no. 13, pp. 6709–6732, 2015.

[130] X. Huang, "Separator technologies for lithium-ion batteries," *Journal of Solid State Electrochemistry*, vol. 15, no. 4, pp. 649–662, 2011.

[131] S.-T. Myung, Y. Hitoshi, and Y.-K. Sun, "Electrochemical behavior and passivation of current collectors in lithium-ion batteries," *Journal of Materials Chemistry*, vol. 21, no. 27, pp. 9891–9911, 2011.

[132] S. S. Zhang, "A review on the separators of liquid electrolyte li-ion batteries," *Journal of power sources*, vol. 164, no. 1, pp. 351–364, 2007.

[133] Y. Xiang, J. Li, J. Lei, D. Liu, Z. Xie, D. Qu, K. Li, T. Deng, and H. Tang, "Advanced separators for lithium-ion and lithium–sulfur batteries: a review of recent progress," *ChemSusChem*, vol. 9, no. 21, pp. 3023–3039, 2016.

[134] C. F. Francis, I. L. Kyratzis, and A. S. Best, "Lithium-ion battery separators for ionic-liquid electrolytes: a review," *Advanced Materials*, vol. 32, no. 18, p. 1904205, 2020.

[135] L. Zhang, X. Li, M. Yang, and W. Chen, "High-safety separators for lithium-ion batteries and sodium-ion batteries: advances and perspective," *Energy Storage Materials*, vol. 41, pp. 522–545, 2021.

[136] P. Arora and Z. Zhang, "Battery separators," *Chemical reviews*, vol. 104, no. 10, pp. 4419–4462, 2004.

[137] L. Guo, D. B. Thornton, M. A. Koronfel, I. E. Stephens, and M. P. Ryan, "Degradation in lithium ion battery current collectors," *Journal of Physics: Energy*, vol. 3, no. 3, p. 032015, 2021.

[138] M. Yamada, T. Watanabe, T. Gunji, J. Wu, and F. Matsumoto, "Review of the design of current collectors for improving the battery performance in lithium-ion and post-lithium-ion batteries," *Electrochem*, vol. 1, no. 2, pp. 124–159, 2020.

[139] A. H. Whitehead and M. Schreiber, "Current collectors for positive electrodes of lithium-based batteries," *Journal of The Electrochemical Society*, vol. 152, no. 11, p. A2105, 2005.

[140] S. Jin, Y. Jiang, H. Ji, and Y. Yu, "Advanced 3d current collectors for lithium-based batteries," *Advanced Materials*, vol. 30, no. 48, p. 1802014, 2018.

[141] Y. Yue and H. Liang, "3d current collectors for lithium-ion batteries: a topical review," *Small Methods*, vol. 2, no. 8, p. 1800056, 2018.

[142] T. Ma, G.-L. Xu, Y. Li, L. Wang, X. He, J. Zheng, J. Liu, M. H. Engelhard, P. Zapol, L. A. Curtiss, J. Jorne, K. Amine, and Z. Chen, "Revisiting the corrosion of the alu-

minum current collector in lithium-ion batteries," *The journal of physical chemistry letters*, vol. 8, no. 5, pp. 1072–1077, 2017.

[143] S.-T. Myung, Y. Sasaki, S. Sakurada, Y.-K. Sun, and H. Yashiro, "Electrochemical behavior of current collectors for lithium batteries in non-aqueous alkyl carbonate solution and surface analysis by tof-sims," *Electrochimica Acta*, vol. 55, no. 1, pp. 288–297, 2009.

[144] J. Yang, C. Hu, H. Wang, K. Yang, J. B. Liu, and H. Yan, "Review on the research of failure modes and mechanism for lead-acid batteries," *International Journal of Energy Research*, vol. 41, no. 3, p. 336–352, 2016.

[145] H. L. Ferreira, R. Garde, G. Fulli, W. Kling, and J. P. Lopes, "Characterisation of electrical energy storage technologies," *Energy*, vol. 53, pp. 288–298, 2013.

[146] E. Karden, S. Ploumen, B. Fricke, T. Miller, and K. Snyder, "Energy storage devices for future hybrid electric vehicles," *Journal of Power Sources*, vol. 168, no. 1, pp. 2–11, 2007. 10th EUROPEAN LEAD BATTERY CONFERENCE.

[147] H. Gibbard, "Nickel metal hydride battery applications," in *Proceedings of 9th Annual Battery Conference on Applications and Advances*, pp. 127–, 1994.

[148] S. Arya and S. Verma, "Nickel-metal hydride (ni-mh) batteries," *Rechargeable Batteries*, p. 131–175, 2020.

[149] W. Liu, T. Placke, and K. Chau, "Overview of batteries and battery management for electric vehicles," *Energy Reports*, vol. 8, pp. 4058–4084, 2022.

[150] L. Cassayre, B. Guzhov, M. Zielinski, and B. Biscans, "Chemical processes for the recovery of valuable metals from spent nickel metal hydride batteries: A review," *Renewable and Sustainable Energy Reviews*, vol. 170, p. 112983, 2022.

[151] M. Gutsch and J. Leker, "Global warming potential of lithium-ion battery energy storage systems: A review," *Journal of Energy Storage*, vol. 52, p. 105030, 2022.

[152] M. A. Rahman, X. Wang, and C. Wen, "High energy density metal-air batteries: a review," *Journal of the Electrochemical Society*, vol. 160, no. 10, p. A1759, 2013.

[153] J. Deng, S. Fang, Y. Fang, Q. Hao, L. Wang, and Y. H. Hu, "Multiple roles of graphene in electrocatalysts for metal-air batteries," *Catalysis Today*, vol. 409, pp. 2–22, 2023.

[154] P. N. Halimah, S. Rahardian, and B. A. Budiman, "Battery cells for electric vehicles," *International Journal of Sustainable Transportation Technology*, vol. 2, no. 2, pp. 54–57, 2019.

[155] Y. Liu, R. Zhang, J. Wang, and Y. Wang, "Current and future lithium-ion battery manufacturing," *IScience*, vol. 24, no. 4, 2021.

[156] S. Baazouzi, N. Feistel, J. Wanner, I. Landwehr, A. Fill, and K. P. Birke, "Design, properties, and manufacturing of cylindrical li-ion battery cells—a generic overview," *Batteries*, vol. 9, no. 6, p. 309, 2023.

[157] S. S. Lee, T. H. Kim, S. J. Hu, W. W. Cai, and J. A. Abell, "Joining technologies for automotive lithium-ion battery manufacturing: A review," in *International Manufacturing Science and Engineering Conference*, vol. 49460, pp. 541–549, 2010.

[158] O. E. Bankole, C. Gong, and L. Lei, "Battery recycling technologies: Recycling waste lithium-ion batteries with the impact on the environment in-view," *Journal of Environment and Ecology*, vol. 4, no. 1, pp. 14–28, 2013.

[159] K. Yeow, H. Teng, M. Thelliez, and E. Tan, "3d thermal analysis of li-ion battery cells with various geometries and cooling conditions using abaqus," in *Proceedings of the SIMULIA community conference*, 2012.

[160] S. Landini, J. Leworthy, and T. O'Donovan, "A review of phase change materials for the thermal management and isothermalisation of lithium-ion cells," *Journal of Energy Storage*, vol. 25, p. 100887, 2019.

[161] R. Schröder, M. Aydemir, and G. Seliger, "Comparatively assessing different shapes of lithium-ion battery cells," *Procedia Manufacturing*, vol. 8, pp. 104–111, 2017.

[162] E. Maiser, "Battery packaging-technology review," in *AIP Conference Proceedings*, vol. 1597, pp. 204–218, American Institute of Physics, 2014.

[163] S.-H. Lee and I.-H. Ko, "Failure analysis of swelling in prismatic lithium-ion batteries during their cycle life after long-term storage," *Journal of Failure Analysis and Prevention*, vol. 18, no. 3, pp. 554–561, 2018.

[164] M. Yoshio, R. J. Brodd, and A. Kozawa, *Lithium-ion batteries*, vol. 1. Springer, 2009.

[165] H. Maleki, H. Wang, W. Porter, and J. Hallmark, "Li-ion polymer cells thermal property changes as a function of cycle-life," *Journal of Power Sources*, vol. 263, pp. 223–230, 2014.

[166] S. Chen, C. Niu, H. Lee, Q. Li, L. Yu, W. Xu, J.-G. Zhang, E. J. Dufek, M. S. Whittingham, S. Meng, J. Xiao, and J. Liu, "Critical parameters for evaluating coin cells and pouch cells of rechargeable li-metal batteries," *Joule*, vol. 3, no. 4, pp. 1094–1105, 2019.

[167] H. Saariluoma, A. Piiroinen, A. Unt, J. Hakanen, T. Rautava, and A. Salminen, "Overview of optical digital measuring challenges and technologies in laser welded components in ev battery module design and manufacturing," *Batteries*, vol. 6, no. 3, p. 47, 2020.

[168] Y. Li, J. Song, and J. Yang, "A review on structure model and energy system design of lithium-ion battery in renewable energy vehicle," *Renewable and Sustainable Energy Reviews*, vol. 37, pp. 627–633, 2014.

[169] G. L. Plett, *Battery management systems, Volume II: Equivalent-circuit methods*. Artech House, 2015.

[170] Y. Xing, E. W. Ma, K. L. Tsui, and M. Pecht, "Battery management systems in electric and hybrid vehicles," *Energies*, vol. 4, no. 11, pp. 1840–1857, 2011.

[171] M. A. Hannan, M. M. Hoque, A. Hussain, Y. Yusof, and P. J. Ker, "State-of-the-art and energy management system of lithium-ion batteries in electric vehicle applications: Issues and recommendations," *Ieee Access*, vol. 6, pp. 19362–19378, 2018.

[172] H. A. Gabbar, A. M. Othman, and M. R. Abdussami, "Review of battery management systems (bms) development and industrial standards," *Technologies*, vol. 9, no. 2, p. 28, 2021.

[173] D. Andrea, *Battery management systems for large lithium-ion battery packs*. Artech house, 2010.

[174] M. Lelie, T. Braun, M. Knips, H. Nordmann, F. Ringbeck, H. Zappen, and D. U. Sauer, "Battery management system hardware concepts: An overview," *Applied Sciences*, vol. 8, no. 4, p. 534, 2018.

[175] Y. Wang, J. Tian, Z. Sun, L. Wang, R. Xu, M. Li, and Z. Chen, "A comprehensive review of battery modeling and state estimation approaches for advanced battery management systems," *Renewable and Sustainable Energy Reviews*, vol. 131, p. 110015, 2020.

[176] G. Xia, L. Cao, and G. Bi, "A review on battery thermal management in electric vehicle application," *Journal of power sources*, vol. 367, pp. 90–105, 2017.

[177] H. Liu, Z. Wei, W. He, and J. Zhao, "Thermal issues about li-ion batteries and recent progress in battery thermal management systems: A review," *Energy conversion and management*, vol. 150, pp. 304–330, 2017.

[178] J. Jaguemont and J. Van Mierlo, "A comprehensive review of future thermal management systems for battery-electrified vehicles," *Journal of Energy Storage*, vol. 31, p. 101551, 2020.

[179] M. Lu, X. Zhang, J. Ji, X. Xu, and Y. Zhang, "Research progress on power battery cooling technology for electric vehicles," *Journal of Energy Storage*, vol. 27, p. 101155, 2020.

[180] M. Shahjalal, T. Shams, M. E. Islam, W. Alam, M. Modak, S. B. Hossain, V. Ramadesigan, M. R. Ahmed, H. Ahmed, and A. Iqbal, "A review of thermal management for li-ion batteries: Prospects, challenges, and issues," *Journal of energy storage*, vol. 39, p. 102518, 2021.

[181] W. Wu, S. Wang, W. Wu, K. Chen, S. Hong, and Y. Lai, "A critical review of battery thermal performance and liquid based battery thermal management," *Energy conversion and management*, vol. 182, pp. 262–281, 2019.

[182] K. J. Kelly, M. Mihalic, and M. Zolot, "Battery usage and thermal performance of the toyota prius and honda insight during chassis dynamometer testing," in *Seventeenth Annual Battery Conference on Applications and Advances. Proceedings of Conference (Cat. No. 02TH8576)*, pp. 247–252, IEEE, 2002.

[183] N. Yang, X. Zhang, G. Li, and D. Hua, "Assessment of the forced air-cooling performance for cylindrical lithium-ion battery packs: A comparative analysis between aligned and staggered cell arrangements," *Applied thermal engineering*, vol. 80, pp. 55–65, 2015.

[184] K. Chen, W. Wu, F. Yuan, L. Chen, and S. Wang, "Cooling efficiency improvement of air-cooled battery thermal management system through designing the flow pattern," *Energy*, vol. 167, pp. 781–790, 2019.

[185] S. Hong, X. Zhang, K. Chen, and S. Wang, "Design of flow configuration for parallel air-cooled battery thermal management system with secondary vent," *International Journal of Heat and Mass Transfer*, vol. 116, pp. 1204–1212, 2018.

[186] E. Jiaqiang, M. Yue, J. Chen, H. Zhu, Y. Deng, Y. Zhu, F. Zhang, M. Wen, B. Zhang, and S. Kang, "Effects of the different air cooling strategies on cooling performance of a lithium-ion battery module with baffle," *Applied Thermal Engineering*, vol. 144, pp. 231–241, 2018.

[187] R. Schmidt and F. C. Engineer, "Packaging of new servers, energy efficiency aspects," in *1st Berkeley Symposium on Energy Efficient Electronics*, pp. 9–12, 2009.

[188] D. Chen, J. Jiang, G.-H. Kim, C. Yang, and A. Pesaran, "Comparison of different cooling methods for lithium ion battery cells," *Applied Thermal Engineering*, vol. 94, pp. 846–854, 2016.

[189] Y. Chung and M. S. Kim, "Thermal analysis and pack level design of battery thermal management system with liquid cooling for electric vehicles," *Energy conversion and management*, vol. 196, pp. 105–116, 2019.

[190] G. Murali, G. Sravya, J. Jaya, and V. N. Vamsi, "A review on hybrid thermal management of battery packs and it's cooling performance by enhanced pcm," *Renewable and Sustainable Energy Reviews*, vol. 150, p. 111513, 2021.

[191] Z. Wang, Z. Zhang, L. Jia, and L. Yang, "Paraffin and paraffin/aluminum foam composite phase change material heat storage experimental study based on thermal management of li-ion battery," *Applied Thermal Engineering*, vol. 78, pp. 428–436, 2015.

[192] S. Shahid and M. Agelin-Chaab, "A review of thermal runaway prevention and mitigation strategies for lithium-ion batteries," *Energy Conversion and Management: X*, p. 100310, 2022.

[193] X. Feng, M. Ouyang, X. Liu, L. Lu, Y. Xia, and X. He, "Thermal runaway mechanism of lithium ion battery for electric vehicles: A review," *Energy Storage Materials*, vol. 10, pp. 246–267, 2018.

[194] Z. Liao, S. Zhang, K. Li, G. Zhang, and T. G. Habetler, "A survey of methods for monitoring and detecting thermal runaway of lithium-ion batteries," *Journal of Power Sources*, vol. 436, p. 226879, 2019.

[195] N. I. Shchurov, S. I. Dedov, B. V. Malozyomov, A. A. Shtang, N. V. Martyushev, R. V. Klyuev, and S. N. Andriashin, "Degradation of lithium-ion batteries in an electric transport complex," *Energies*, vol. 14, no. 23, p. 8072, 2021.

[196] V. A. Agubra and J. W. Fergus, "The formation and stability of the solid electrolyte interface on the graphite anode," *Journal of Power Sources*, vol. 268, pp. 153–162, 2014.

[197] C. Yan, R. Xu, Y. Xiao, J.-F. Ding, L. Xu, B.-Q. Li, and J.-Q. Huang, "Toward critical electrode/electrolyte interfaces in rechargeable batteries," *Advanced Functional Materials*, vol. 30, no. 23, p. 1909887, 2020.

[198] J. Vetter, P. Novák, M. R. Wagner, C. Veit, K.-C. Möller, J. Besenhard, M. Winter, M. Wohlfahrt-Mehrens, C. Vogler, and A. Hammouche, "Ageing mechanisms in lithium-ion batteries," *Journal of power sources*, vol. 147, no. 1-2, pp. 269–281, 2005.

[199] M. L. Divya, Y.-S. Lee, and V. Aravindan, "Solvent co-intercalation: an emerging mechanism in li-, na-, and k-ion capacitors," *ACS Energy Letters*, vol. 6, no. 12, pp. 4228–4244, 2021.

[200] X. Lai, Y. Zheng, L. Zhou, and W. Gao, "Electrical behavior of overdischarge-induced internal short circuit in lithium-ion cells," *Electrochimica Acta*, vol. 278, pp. 245–254, 2018.

[201] M. Petzl and M. A. Danzer, "Nondestructive detection, characterization, and quantification of lithium plating in commercial lithium-ion batteries," *Journal of Power Sources*, vol. 254, pp. 80–87, 2014.

[202] J. Fan and S. Tan, "Studies on charging lithium-ion cells at low temperatures," *Journal of The Electrochemical Society*, vol. 153, p. A1081, apr 2006.

[203] A. Samanta and S. Chowdhuri, "Active cell balancing of lithium-ion battery pack using dual dc-dc converter and auxiliary lead-acid battery," *Journal of Energy Storage*, vol. 33, p. 102109, 2021.

[204] Y. Shang, Q. Zhang, N. Cui, and C. Zhang, "A cell-to-cell equalizer based on three-resonant-state switched-capacitor converters for series-connected battery strings," *Energies*, vol. 10, no. 2, p. 206, 2017.

[205] Z. B. Omariba, L. Zhang, and D. Sun, "Review on health management system for lithium-ion batteries of electric vehicles," *Electronics*, vol. 7, no. 5, p. 72, 2018.

[206] Z. B. Omariba, L. Zhang, and D. Sun, "Review of battery cell balancing methodologies for optimizing battery pack performance in electric vehicles," *IEEE Access*, vol. 7, pp. 129335–129352, 2019.

[207] Y. Hua, S. Zhou, H. Cui, X. Liu, C. Zhang, X. Xu, H. Ling, and S. Yang, "A comprehensive review on inconsistency and equalization technology of lithium-ion battery for electric vehicles," *International Journal of Energy Research*, vol. 44, no. 14, pp. 11059–11087, 2020.

[208] T. Duraisamy and D. Kaliyaperumal, "Adaptive passive balancing in battery management system for e-mobility," *International Journal of Energy Research*, vol. 45, no. 7, pp. 10752–10764, 2021.

[209] M. Jongerden and B. Haverkort, "Battery modeling," *Enschede, January*, p. 38, 2008.

[210] G. P. Fenner, L. F. Ramos, and L. N. Canha, "Battery analysis using kinetic battery model with voltage response," in *2020 55th International Universities Power Engineering Conference (UPEC)*, pp. 1–5, IEEE, 2020.

[211] S. Shanmuganathan, *Artificial neural network modelling: An introduction*. Springer, 2016.

[212] S. Sharma, S. Sharma, and A. Athaiya, "Activation functions in neural networks," *Towards Data Sci*, vol. 6, no. 12, pp. 310–316, 2017.

[213] A. D. Rasamoelina, F. Adjailia, and P. Sinčák, "A review of activation function for artificial neural network," in *2020 IEEE 18th World Symposium on Applied Machine Intelligence and Informatics (SAMI)*, pp. 281–286, IEEE, 2020.

[214] R. M. Neal, "Connectionist learning of belief networks," *Artificial intelligence*, vol. 56, no. 1, pp. 71–113, 1992.

[215] B. Karlik and A. V. Olgac, "Performance analysis of various activation functions in generalized mlp architectures of neural networks," *International Journal of Artificial Intelligence and Expert Systems*, vol. 1, no. 4, pp. 111–122, 2011.

[216] A. Krizhevsky, I. Sutskever, and G. E. Hinton, "Imagenet classification with deep convolutional neural networks," *Advances in neural information processing systems*, vol. 25, 2012.

[217] A. L. Maas, A. Y. Hannun, and A. Y. Ng, "Rectifier nonlinearities improve neural network acoustic models," in *Proc. icml*, vol. 30, p. 3, Atlanta, GA, 2013.

[218] F. Dettù, G. Pozzato, D. M. Rizzo, and S. Onori, "Exergy-based modeling framework for hybrid and electric ground vehicles," *Applied Energy*, vol. 300, p. 117320, 2021.

[219] J. Newman and W. Tiedemann, "Porous-electrode theory with battery applications," *AIChE Journal*, vol. 21, no. 1, pp. 25–41, 1975.

[220] N. A. Chaturvedi, R. Klein, J. Christensen, J. Ahmed, and A. Kojic, "Algorithms for advanced battery-management systems," *IEEE Control systems magazine*, vol. 30, no. 3, pp. 49–68, 2010.

[221] X. Han, M. Ouyang, L. Lu, and J. Li, "Simplification of physics-based electrochemical model for lithium ion battery on electric vehicle. part i: Diffusion simplification and single particle model," *Journal of Power Sources*, vol. 278, pp. 802–813, 2015.

[222] A. Jokar, B. Rajabloo, M. Désilets, and M. Lacroix, "Review of simplified pseudo-two-dimensional models of lithium-ion batteries," *Journal of Power Sources*, vol. 327, pp. 44–55, 2016.

[223] S. Santhanagopalan, Q. Guo, P. Ramadass, and R. E. White, "Review of models for predicting the cycling performance of lithium ion batteries," *Journal of power sources*, vol. 156, no. 2, pp. 620–628, 2006.

[224] V. Ramadesigan, P. W. Northrop, S. De, S. Santhanagopalan, R. D. Braatz, and V. R. Subramanian, "Modeling and simulation of lithium-ion batteries from a systems engineering perspective," *Journal of the electrochemical society*, vol. 159, no. 3, p. R31, 2012.

[225] H. Perez, S. Dey, X. Hu, and S. Moura, "Optimal charging of li-ion batteries via a single particle model with electrolyte and thermal dynamics," *Journal of The Electrochemical Society*, vol. 164, no. 7, p. A1679, 2017.

[226] J. Li, N. Lotfi, R. G. Landers, and J. Park, "A single particle model for lithium-ion batteries with electrolyte and stress-enhanced diffusion physics," *Journal of The Electrochemical Society*, vol. 164, no. 4, p. A874, 2017.

[227] N. Baba, H. Yoshida, M. Nagaoka, C. Okuda, and S. Kawauchi, "Numerical simulation of thermal behavior of lithium-ion secondary batteries using the enhanced single particle model," *Journal of Power Sources*, vol. 252, pp. 214–228, 2014.

[228] T. R. Tanim, C. D. Rahn, and C.-Y. Wang, "State of charge estimation of a lithium ion cell based on a temperature dependent and electrolyte enhanced single particle model," *Energy*, vol. 80, pp. 731–739, 2015.

[229] I. Gridin, "Learning genetic algorithms with python: empower the performance of machine learning and ai models with the capabilities of a powerful searth algorithm," *(No Title)*, 2021.

[230] K. A. Smith, C. D. Rahn, and C.-Y. Wang, "Control oriented 1d electrochemical model of lithium ion battery," *Energy Conversion and management*, vol. 48, no. 9, pp. 2565–2578, 2007.

[231] K. W. Gao, C. Fang, D. M. Halat, A. Mistry, J. Newman, and N. P. Balsara, "The transference number," *Energy & Environmental Materials*, vol. 5, no. 2, pp. 366–369, 2022.

[232] A. Vadakkepatt, B. Trembacki, S. R. Mathur, and J. Y. Murthy, "Bruggeman's exponents for effective thermal conductivity of lithium-ion battery electrodes," *Journal of the Electrochemical Society*, vol. 163, no. 2, p. A119, 2015.

[233] T. G. Zavalis, M. Behm, and G. Lindbergh, "Investigation of short-circuit scenarios in a lithium-ion battery cell," *Journal of the electrochemical Society*, vol. 159, no. 6, p. A848, 2012.

[234] A. Nyman, M. Behm, and G. Lindbergh, "Electrochemical characterisation and modelling of the mass transport phenomena in lipf6–ec–emc electrolyte," *Electrochimica Acta*, vol. 53, no. 22, pp. 6356–6365, 2008.

[235] K. Kumaresan, G. Sikha, and R. E. White, "Thermal model for a li-ion cell," *Journal of the Electrochemical Society*, vol. 155, no. 2, p. A164, 2007.

[236] D. K. Karthikeyan, G. Sikha, and R. E. White, "Thermodynamic model development for lithium intercalation electrodes," *Journal of Power Sources*, vol. 185, no. 2, pp. 1398–1407, 2008.

[237] J. Sturm, A. Rheinfeld, I. Zilberman, F. B. Spingler, S. Kosch, F. Frie, and A. Jossen, "Modeling and simulation of inhomogeneities in a 18650 nickel-rich, silicon-graphite lithium-ion cell during fast charging," *Journal of Power Sources*, vol. 412, pp. 204–223, 2019.

[238] R. Braga, A. Mevawalla, S. Gudiyella, S. Panchal, M. Giuliano, G. Nicol, and Y. Zheng, "Transient electrochemical modeling and performance investigation under different driving conditions for 144ah li-ion cell with two jelly rolls," tech. rep., SAE Technical Paper, 2023.

[239] K. Liu, K. Li, Q. Peng, and C. Zhang, "A brief review on key technologies in the battery management system of electric vehicles," *Frontiers of mechanical engineering*, vol. 14, pp. 47–64, 2019.

[240] S. Du, Y. Lai, L. Ai, L. Ai, Y. Cheng, Y. Tang, and M. Jia, "An investigation of irreversible heat generation in lithium ion batteries based on a thermo-electrochemical coupling method," *Applied Thermal Engineering*, vol. 121, pp. 501–510, 2017.

[241] G. Liu, M. Ouyang, L. Lu, J. Li, and X. Han, "Analysis of the heat generation of lithium-ion battery during charging and discharging considering different influencing factors," *Journal of Thermal Analysis and Calorimetry*, vol. 116, pp. 1001–1010, 2014.

[242] J. Li, *Modeling and Simulation of Lithium-ion Power Battery Thermal Management*. Springer, 2022.

[243] S. W. Churchill and H. H. Chu, "Correlating equations for laminar and turbulent free convection from a vertical plate," *International journal of heat and mass transfer*, vol. 18, no. 11, pp. 1323–1329, 1975.

[244] O. Kalkan, A. Celen, and K. Bakirci, "Experimental and numerical investigation of the lifepo4 battery cooling by natural convection," *Journal of Energy Storage*, vol. 40, p. 102796, 2021.

[245] Y. A. Çengel and A. J. Ghajar, *Heat and Mass Transfer: Fundamentals [and] Applications*. McGraw-Hill Education, 2020.

[246] R. J. Moffat, "Describing the uncertainties in experimental results," *Experimental thermal and fluid science*, vol. 1, no. 1, pp. 3–17, 1988.

[247] S. J. Kline, "Describing uncertainties in single-sample experiments," *Mech. Eng.*, vol. 75, pp. 3–8, 1963.

[248] S. Salicone, *Measurement uncertainty: an approach via the mathematical theory of evidence*. Springer science & business media, 2007.

[249] M. Malik, I. Dincer, M. A. Rosen, M. Mathew, and M. Fowler, "Thermal and electrical performance evaluations of series connected li-ion batteries in a pack with liquid cooling," *Applied Thermal Engineering*, vol. 129, pp. 472–481, 2018.

[250] M. Jongerden and B. Haverkort, "Battery aging and the kinetic battery model," *Enschede: Centre for Telematics and Information Technology (CTIT)*, 2016.

[251] F. Reverter, "A tutorial on thermal sensors in the 200th anniversary of the seebeck effect," *IEEE Sensors Journal*, vol. 21, no. 20, pp. 22122–22132, 2021.

[252] M. Berecibar, I. Gandiaga, I. Villarreal, N. Omar, J. Van Mierlo, and P. Van den Bossche, "Critical review of state of health estimation methods of li-ion batteries for real applications," *Renewable and Sustainable Energy Reviews*, vol. 56, pp. 572–587, 2016.

[253] O. M. Govardhan, "Fundamentals and classification of hybrid electric vehicles," *International Journal of Engineering and Techniques*, vol. 3, no. 5, pp. 194–198, 2017.

[254] M. Shen and Q. Gao, "A review on battery management system from the modeling efforts to its multiapplication and integration," *International Journal of Energy Research*, vol. 43, no. 10, pp. 5042–5075, 2019.

[255] A. Shukla, A. Banerjee, M. Ravikumar, and A. Jalajakshi, "Electrochemical capacitors: Technical challenges and prognosis for future markets," *Electrochimica acta*, vol. 84, pp. 165–173, 2012.

[256] X. Zhang, S. Chen, J. Zhu, and Y. Gao, "A critical review of thermal runaway prediction and early-warning methods for lithium-ion batteries," *Energy Material Advances*, vol. 4, p. 0008, 2023.

VITA AUCTORIS

NAME:	Kieran Johnson-Bujold
PLACE OF BIRTH:	Windsor Ontario Canada
YEAR OF BIRTH:	1996
EDUCATION:	
	Assumption College Catholic High School, Windsor, Ontario, 2011-2015
	University of Windsor, B.Sc in Mechanical Engineering, Windsor, Ontario, 2015-2020
	University of Windsor, M.Sc in Automotive Engineering, Windsor, Ontario, 2020-2023